



**Mónica Filipa dos Santos Mendes**

Master of Science in Biomedical Engineering

## **Probing Radiosensitisers in Electron Transfer Experiments**

Thesis submitted in partial fulfilment of the  
requirements for the degree of

Doctor of Philosophy in  
**Radiation Biology and Biophysics**  
**Applied Atomic and Molecular Physics**

Supervisor: Prof. Paulo Limão-Vieira, Full Professor  
Universidade Nova de Lisboa

Co-supervisor: Prof. Gustavo García Gómez-Tejedor, Full Professor  
Consejo Superior de Investigaciones Científicas

Examination Committee

Chairperson: Prof. João Carlos da Palma Goes  
Rapporteurs: Prof. Luís Paulo da Mota Capitão Lemos Alves  
Prof. Alexander Dorn  
Members: Prof. Pedro António de Brito Tavares  
Prof. Gustavo García Gómez-Tejedor

 **FACULDADE DE  
CIÊNCIAS E TECNOLOGIA  
UNIVERSIDADE NOVA DE LISBOA**

**March, 2019**



## **Probing Radiosensitisers in Electron Transfer Experiments**

Copyright © Mónica Filipa dos Santos Mendes, Faculdade de Ciências e Tecnologia, Universidade NOVA de Lisboa.

A Faculdade de Ciências e Tecnologia e a Universidade NOVA de Lisboa têm o direito, perpétuo e sem limites geográficos, de arquivar e publicar esta dissertação através de exemplares impressos reproduzidos em papel ou de forma digital, ou por qualquer outro meio conhecido ou que venha a ser inventado, e de a divulgar através de repositórios científicos e de admitir a sua cópia e distribuição com objetivos educacionais ou de investigação, não comerciais, desde que seja dado crédito ao autor e editor.



*“Nothing in life is to be feared, it is only to be understood. Now is the time to understand more, so that we may fear less”*

Marie Curie



# ACKNOWLEDGEMENTS

I feel very grateful for the opportunity I had to start my PhD 4 years ago. During this time I have learned such important and interesting things that made me grow both professionally but, especially as a person. Do a PhD is like a roller coaster with funny moments, frustrating days and motivating days but it is worthy in the end. All of these moments could not be lived and achieved without the best people by my side. So, I would like to thank...

To the financial support from the Portuguese National Funding Agency FCT-MCTES through PD/BD/106038/2015 scholarship. This work was also supported by Radiation Biology and Biophysics Doctoral Training Programme (RaBBiT, PD/00193/2012); UID/Multi/04378/2013 (UCIBIO).

To Prof. Dr. Paulo Limão-Vieira for all the support, supervision and motivation throughout the course of this work, as well as for the opportunity to visit other international groups and attend scientific meetings. Thank you for believing in my work!

To Prof. Dr. Gustavo García for support, supervision and for giving me the opportunity to be part of his research group and performed part of my work in his lab, as well as for the opportunity to visit other international groups and attend scientific meetings. These two years in Madrid were truly important and unforgettable.

To Prof. Dr. Filipe Ferreira da Silva for his friendship, support and scientific conversations that help me so much.

All of the remaining members of Molecular Physics and Applications research group, particularly Ana Cruz and Afonso Moutinho for their willingness to help at any moment.

To the Department of Physics of NOVA University of Lisbon and CEFITEC through UID/FIS/00068/2019 and PTDC/FIS-AQM/31281/2017.

To the Instituto de Física Fundamental of Consejo Superior de Investigaciones Científicas (CSIC) in Madrid for giving me all the support, supervision and working conditions to perform the work of this thesis.

To all my colleagues of CEFITEC, Emanuele Lange, André Rebelo, João Ameixa, Alexandra Loupas, Tiago Cunha, Guilherme Meneses, Telma Santos, Sarvesh Kumar, João Silva, José Romero, Rodrigo Rodrigues, Gonçalo Barreto and Diego Farago Pastega. Thank you for all the good moments and conversations that made everything easier.

To Filipa Pires for her friendship and tremendous support during these years. I have no doubt that without you it would be much more difficult.

To Alessandra de Souza Barbosa for her friendship and good times we spent together. I am glad that you decided to visit our lab one day.

To all my colleagues of CSIC, Lilian Ellis-Gibbings, Ali Traoré, Alexey Verkhovtsev, Carlos Guerra, Filipe Costa and Lidia Álvarez. In particular, to Ana Lozano for her kindness, motivation and friendship that encouraged me to pursue my work. I am really grateful for having meet you!

To my dear friends Mariana Baptista and Filipa Costa for all the support and long conversations about science. Thank you for your motivation and to believe in me! You were my first friends in science, and you will be with me forever. I have no doubt about that.

To my lifelong friends that have been with me in almost all the important and memorable moments of my life, even when we are separated by miles and miles. So, thank you to Carina, Luís, Hélder, Beto, Jorge, Lisandra, Sandrine, Bruno, Ana Rita, Lígia, Licas, Carla, Raquel, Daniela, Vanessa, Cláudia and Cíntia.

I would like to give a special thanks to my dear friend Susana. You are amazing and I am a such lucky person to have you in my life throughout the last 23 years.

To Ricardo for your love, patience, to believe in me and being by my side no matter what. Thank you! You are my best!

In finally, I would like to dedicate this thesis to my dearest family, my brother Miguel, my sister Lili, my grandmother “Avó” São, my grandmother “Avó” Laurinda (who is watching me wherever she is) and my love parents. Everything was because of them. Thank you for your unconditional love and support. You always believed in me and gave me confidence to go through all the obstacles in my life. I own you everything! Thank you so much! Love you!



# ABSTRACT

The impact of ionising radiation in the living systems is being investigated for decades, because its capability to induce damage in tissues and cells, compromising the DNA molecule integrity, resulting in mutations and eventually cells death. Considering this, ionising radiation can be very useful in different fields, especially in radiation therapy. However, it is necessary to guarantee that the effects of radiation in normal tissues during a radiation treatment are minimised. Many efforts have been made to improve the radiotherapy protocols, namely by the application of radiosensitisers which enhance the effect of radiation. Recent research investigations have demonstrated the role of secondary low-energy electrons as the main damaging agents in DNA. These secondary electrons can interact directly or indirectly with molecules, producing highly reactive species (ions and radicals). Moreover, it is also known that electrons do not exist freely in the physiological medium, but rather in solvated and/or in pre-solvated states. Therefore, studies on electron transfer between atoms/ions and biomolecules seems crucial to better understand the molecular mechanism of radiation interaction.

The work presented in this thesis consists on the study of electron transfer collisions of atoms/ions in molecules of biological relevance. Initially, neutral potassium collisions in imidazole, nitroimidazoles (4-nitroimidazole and 2-nitroimidazole) and methylated compounds (1-methyl-4-nitroimidazole and 1-methyl-5-nitroimidazole) were investigated by time-of-flight (TOF) mass spectrometry in a crossed beam experiment comprising a neutral potassium beam and a molecular effusive beam. In these experiments the anionic fragmentation patterns and yields were obtained. These results present some differences from the dissociative electron attachment (free electrons) results, highlighting the importance of charge transfer studies in understanding the molecular reactions upon radiation. The second part of the work was performed in a novel crossed beam setup where collisions between oxygen anions and molecules as nitrogen, water and pyridine were investigated by measuring positive and negative fragmentation patterns through TOF mass spectrometry. From these studies we obtained for the first time experimental electron detachment cross-section of  $O_2^-$  in water and pyridine.

**Keywords:** Electron transfer, radiosensitisers, time-of-flight mass spectrometry, atom/ion molecules collisions, negative/positive ion formation.



# RESUMO

A interação da radiação ionizante com os sistemas biológicos tem despertado o interesse da comunidade científica nas últimas décadas, principalmente devido à capacidade de induzir dano ao nível dos tecidos e células, comprometendo as biomoléculas, nomeadamente a integridade da molécula de ADN. Considerando estes efeitos, a radiação ionizante pode ser muito útil em diferentes áreas, nomeadamente em medicina através do seu uso em terapia oncológica. No entanto, é necessário garantir que, durante os tratamentos, os tecidos normais adjacentes ao tecido tumoral sejam preservados evitando posteriores danos a longo prazo. Neste sentido, têm sido feitos esforços no sentido de otimizar os protocolos de radioterapia, nomeadamente através de compostos moleculares radiosensibilizadores. Descobertas recentes demonstraram que os eletrões secundários de baixa energia que se formam após irradiação do meio biológico desempenham um papel fulcral nos danos ao nível do ADN. Estes eletrões secundários podem interagir direta ou indiretamente com as moléculas produzindo espécies altamente reativas, tais como iões e radicais livres. Sabe-se ainda que os eletrões não estão presentes de forma livre no meio fisiológico, mas solvatados ou pré-solvatados em molécula de água. Desta forma, estudos de transferência de eletrão entre átomos/iões e biomoléculas são cruciais para um melhor conhecimento ao nível dos mecanismos moleculares envolvidos na interação com a radiação.

O trabalho apresentado nesta tese consiste no estudo de transferência de eletrão em colisões de átomos/iões com moléculas de relevância biológica. Inicialmente, foram investigadas colisões de potássio com a molécula imidazol, nitroimidazóis (4-nitroimidazol e 2-nitroimidazol) e compostos metilados (1-metil-4-nitroimidazol e 1-metil-5-nitroimidazol) através de estudos de espectrometria de massa do tipo tempo-de-voou. Para tal usou-se um equipamento de feixes cruzados onde um feixe de átomos neutros de potássio colide com um feixe molecular em fase gasosa. Durante as medidas experimentais foram obtidos os padrões de fragmentação para as moléculas em estudo, que foram comparados com estudos de captura eletrónica dissociativa. Verificou-se que existem alguma diferenças entre estes dois métodos, o que realça a importância de estudo de transferência de carga para melhor compreender as reações moleculares após irradiação. A segunda parte deste trabalho foi desenvolvida num equipamento inovador de feixes cruzados com o qual se podem realizar estudos de colisões entre iões negativos de oxigénio e moléculas, tais como azoto molecular, água e piridina. Através de espectrometria do tipo tempo de voo foram analisados os padrões de fragmentação para iões positivos e negativos, e obtidos experimentalmente pela primeira vez secções eficazes de dissociação eletrónica em colisões envolvendo  $O_2^-$  e moléculas como água e piridina.

**Palavras-chave:** Transferência de eletrão, radiosensibilizadores, espectrometria de massa, colisões átomo/ião-molécula, padrão de fragmentação.



# CONTENTS

<b>ACKNOWLEDGEMENTS</b> .....	<b>VII</b>
<b>ABSTRACT</b> .....	<b>IX</b>
<b>RESUMO</b> .....	<b>XI</b>
<b>CONTENTS</b> .....	<b>XIII</b>
<b>LIST OF FIGURES</b> .....	<b>XVII</b>
<b>LIST OF TABLES</b> .....	<b>XXI</b>
<b>ACRONYMS AND SYMBOLS</b> .....	<b>XXIII</b>
<b>CHAPTER 1</b> .....	<b>1</b>
<b>INTRODUCTION</b> .....	<b>1</b>
<b>1.1 Motivation</b> .....	<b>1</b>
1.1.1 Cancer .....	1
1.1.2 Effects of ionising radiation in biological systems .....	2
1.1.3 Impact of low-energy electrons in biomolecules .....	4
1.1.3.1 Direct effects: dissociative electron attachment.....	5
1.1.3.2 Indirect effects: production of highly reactive species .....	7
1.1.4 Electron transfer processes in biomolecules damage .....	9
1.1.5 Radiosensitisers.....	11
<b>1.2 Outline of the Thesis</b> .....	<b>13</b>
<b>CHAPTER 2</b> .....	<b>15</b>
<b>COLLISION THEORY IN ELECTRON TRANSFER PROCESSES</b> .....	<b>15</b>
<b>2.1 Two-Particles Collision</b> .....	<b>15</b>
<b>2.2 Atom–Molecule Collisions</b> .....	<b>20</b>
<b>2.3 Ion–Molecule Collisions</b> .....	<b>22</b>
<b>CHAPTER 3</b> .....	<b>25</b>
<b>EXPERIMENTAL SETUPS</b> .....	<b>25</b>
<b>3.1 Potassium–Molecule Collision Crossed Beam Experimental Setup</b> .....	<b>25</b>
3.1.1 Overview .....	25
3.1.2 Neutral Potassium Beam .....	26

3.1.3	Langmuir-Taylor detector .....	28
3.1.4	Molecular Target Oven .....	28
3.1.5	Time-of-Flight Mass Spectrometer .....	29
3.1.5.1.	TOF spectrometry introduction.....	29
3.1.5.2.	Dual-Stage linear TOF.....	30
3.1.5.3.	Dual-stage Reflectron TOF.....	32
3.1.6	Hemispherical Energy Analyser (HEA).....	33
3.1.7	Vacuum system .....	33
<b>3.2</b>	<b>O<sub>2</sub><sup>-</sup> – Molecule Collision Crossed Beam Experimental Setup .....</b>	<b>35</b>
3.2.1	Overview .....	35
3.2.2	Anionic projectile beam .....	36
3.2.3	TOF mass spectrometers .....	37
3.2.3.1.	Post-collisional negative and positive ions detection .....	37
3.2.3.2.	Post-collisional primary beam detection.....	38
3.2.4	Data acquisition methodology.....	39
3.2.4.1.	Total electron detachment cross-sections .....	39
3.2.4.2.	Positive and negative ions detection .....	41
3.2.5	Optimisation procedures .....	42
3.2.6	Vacuum system .....	44
<b>CHAPTER 4</b>	<b>.....</b>	<b>47</b>
<b>ELECTRON TRANSFER EXPERIMENTS IN K–MOLECULES COLLISIONS.....</b>	<b>47</b>	
<b>4.1</b>	<b>Selective Bond Excision of Nitroimidazoles in Electron Transfer Experiments.....</b>	<b>47</b>
4.1.1	Experimental Section .....	54
4.1.2	Theoretical Section.....	54
<b>4.2</b>	<b>Dynamics of Negative Ions in Potassium Collisions with Imidazole, Nitroimidazoles and Methylated Compounds .....</b>	<b>56</b>
4.2.1	Introduction.....	57
4.2.2	Experimental Methods .....	59
4.2.3	Theoretical Method .....	59
4.2.4	Results and Discussion.....	59
4.2.5	Conclusions.....	71
<b>4.3</b>	<b>Ion-Pair Formation in Neutral Potassium-Neutral Pyrimidine Collisions: Electron Transfer Experiments .....</b>	<b>72</b>
4.3.1	Introduction.....	73
4.3.2	Experimental Methods .....	74
4.3.3	Theoretical Method .....	75
4.3.4	Results and Discussion.....	76
4.3.5	Conclusions.....	81
<b>CHAPTER 5</b>	<b>.....</b>	<b>83</b>
<b>ELECTRON TRANSFER EXPERIMENTS IN O<sub>2</sub><sup>-</sup> – MOLECULES COLLISIONS.....</b>	<b>83</b>	

---

<b>5.1</b>	<b>Experimental Electron Detachment Cross-sections for Collisions of <math>O_2^-</math> with <math>N_2</math> Molecules in the Energy Range 50-7000 eV</b> .....	<b>83</b>
5.1.1	Introduction.....	84
5.1.2	Results and Discussion.....	85
5.1.3	Conclusions.....	88
<b>5.2</b>	<b>Experimental Electron Detachment Cross-sections for Collisions of <math>O_2^-</math> from Water and Pyridine Molecules in the Energy Range 10–4000 eV</b> .....	<b>90</b>
5.2.1	Introduction.....	91
5.2.2	Results and Discussion.....	93
5.2.3	Conclusions.....	99
<b>CHAPTER 6</b>	.....	<b>101</b>
<b>CONCLUSIONS</b>	.....	<b>101</b>
<b>6.1</b>	<b>Concluding Remarks</b> .....	<b>101</b>
6.1.1	Electron Transfer in K – Molecule Collisions .....	101
6.1.2	Electron Transfer in $O_2^-$ – Molecule Collisions.....	103
<b>6.2</b>	<b>Future Work</b> .....	<b>103</b>
<b>REFERENCES</b>	.....	<b>105</b>





# LIST OF FIGURES

Figure 1.1. Chronological diagram of radiation-induced damage.....	3
Figure 1.2. Single electron tracks simulation in liquid water. (a) Electrons with 10 keV incident energies are slowed down by successive interactions with matter (e.g. elastic scattering ●, rotational excitation ●, vibrational excitation ●, electronic excitation ●, neutral dissociation ●, ionisation ●, and electron attachment ●). Image taken from ref. [32].....	4
Figure 1.3. Formation of a temporary negative ion in the DNA molecule after the capture of low-energy electrons that which leads to DNA strand breaks. Taken from ref. [36].....	6
Figure 1.4. Measured quantum yields, per incident electron (3 to 20 eV), for the induction of DSBs (A), SSBs (B), and loss of the supercoiled DNA form (C), in DNA films. Taken from ref. [37]. ....	7
Figure 1.5. DNA damage caused by indirect effects (water radiolysis). Taken from ref. [60]. ....	9
Figure 2.1. Schematics of adiabatic and diabatic potential energy curves for an atom-atom collision. $E_1$ and $E_2$ represent the adiabatic states (full curves). The dashed lines represent the diabatic states: $H_{11}$ (covalent) and $H_{22}$ (ionic). $R_c$ is the crossing radius. Adapted from ref. [62].....	19
Figure 2.2. Schematics of atom-atom scattering representing the four possible pathways considering the impact parameter $b$ and two different crossing radii. Adapted from ref. [62].....	20
Figure 3.1. Schematics of the linear TOF experimental apparatus: a) potassium oven; b) charge-exchange chamber; c) cationic potassium source; d) deflecting plates; e) Langmuir-Taylor detector; f) molecular target oven; g) collision/extraction region; h) TOF mass spectrometer; and i) channeltron detector. Adapted from ref. [62].....	26
Figure 3.2. Schematics of the new reflectron TOF apparatus and the hemispherical analyser: a) stack of laser cut electrodes (reflectron); b) deflecting plates; c) lens elements; d) hemispherical analyser; e) Einzel lens at the entrance of analyser; f) channeltron detector; and g) microchannel plate (MCP) detector. Taken from ref. [120]. ....	27
Figure 3.3. Schematics of the charge exchange hyperthermal neutral potassium beam formation..	27
Figure 3.4. Langmuir-Taylor detector. Taken from ref. [120]. ....	29
Figure 3.5. Schematics of the implemented linear TOF mass spectrometer. ....	31
Figure 3.6. Electrical connections of the TOF extraction system. ....	31
Figure 3.7. Schematic representation of the basic principle of a Reflectron TOF mass spectrometer showing two ions with the same $m/z$ produced in the extraction region with different velocity distributions.....	32
Figure 3.8. Vacuum system schematics: 1) Rotary pump; 2) Electro-magnetic valve; 3) Membrane valve; 4) Diffusion pump; 5) Baffle; 6) Gate valve; 7) Potassium chamber; 8) Collision chamber; 9) Turbomolecular pump; 10) Flexible tube; 11) Vacuum gauge control unit with dial indicator; 12) Penning gauge; 13) Vacuum gauge control unit with digital indicator; 14) TOF mass spectrometer; 15) Pirani gauge. Taken from ref. [120].....	34

Figure 3.9. Reflectron TOF instrument overview recently installed from Kore Technology, UK. Image courtesy of © Kore Technology, Ltd. ....	34
Figure 3.10. Schematics of the experimental setup with: V, pulsed supersonic valve; C, hollow cathode discharge; A <sub>1</sub> and A <sub>2</sub> , anodes; L <sub>1</sub> , L <sub>2</sub> and L <sub>3</sub> , Einzel lenses; D <sub>1</sub> , D <sub>2</sub> , D <sub>3</sub> and D <sub>4</sub> , deflecting plates; M <sub>1</sub> and M <sub>2</sub> , magnets; E <sub>1</sub> , E <sub>2</sub> , E <sub>3</sub> and E <sub>4</sub> , extraction plates; G <sub>2</sub> , focusing/attenuation grids; EG, electron gun; GC, gas cell; MCP 1 and MCP 2, multichannel plate detectors; QMS, quadrupole mass spectrometer; SEM, secondary electron multiplier detector; P <sub>1</sub> , P <sub>2</sub> , P <sub>3</sub> and P <sub>4</sub> , turbomolecular pumps. ....	35
Figure 3.11. Electrical schematics of the anion beam source. V, pulsed supersonic valve; A <sub>1</sub> and A <sub>2</sub> , anodes; C, hollow cathode discharge; L <sub>1</sub> , Einzel lens; VD, discharge voltage; VF, focusing voltage. ....	37
Figure 3.12. Schematics of the implemented TOF spectrometer with: a) the first commercial extraction system implemented into the chamber; b) the modified extraction system with a homemade cylindrical scattering chamber. E <sub>1</sub> and E <sub>2</sub> are the extraction plates and F <sub>3</sub> is an acceleration grid. ....	38
Figure 3.13. Schematics of the second extraction system implemented to detect and analyse the anionic primary beam. ....	39
Figure 3.14. Typical Time-of-flight mass spectrum of the projectile beam (O <sub>2</sub> <sup>-</sup> /O <sup>-</sup> ) at 200 eV in laboratory frame. ....	41
Figure 3.15. Example of a time-of-flight mass spectrum of N <sub>2</sub> at 560 eV where: the black line is the extraction pulse at E <sub>1</sub> , the pink line is the anionic incident beam and the green line is the collision resultant positive ions. ....	42
Figure 3.16. a) time-of-flight spectra of different discharge precursor gases: hydrogen (blue line), oxygen (red line), argon (green line) and carbon dioxide (yellow line); b) calibration curve time x mass. ....	43
Figure 3.17. Time-of-flight mass spectrum of positive ions detection in O <sub>2</sub> <sup>-</sup> + CH <sub>3</sub> NO <sub>2</sub> at 1300 eV (lab frame). ....	44
Figure 3.18. O <sub>2</sub> precursor discharge gas analysis in four different situations. ....	44
Figure 4.1. Molecular structures of 4-nitroimidazole (4NI), 2-nitroimidazole (2NI), 1-methyl-4-nitroimidazole (Me4NI) and 1-methyl-4-nitroimidazole (Me5NI). ....	49
Figure 4.2. Time-of-flight mass spectra of negative ions from electron transfer experiments at 100 eV lab frame energy for 4(5)NI, 2NI, Me4NI and Me5NI. ....	50
Figure 4.3. Time-of-flight mass spectra showing anions produced in electron transfer experiments at 10 eV lab frame energy for 4(5)NI, 2NI, Me4NI and Me5NI. The metastable parent anion M <sup>-</sup> is visible for all cases while the loss of a OH <sup>•</sup> radical is only operative in 4(5)NI and 2NI, the former also showing CN <sup>-</sup> formation. ....	51
Figure 4.4. Left column: M06-2X/aug-cc-pvtz level of theory optimized structures of radical anions and their SOMOs; Right column: lowest σ* orbitals from HF/D95VH level of theory, for 4(5)NI, Me4NI and Me5NI. C, N, and O atoms are represented in white, grey, blue and red colours, respectively. Positive and negative values of the wave function have a red and green colours, respectively. ....	53

Figure 4.5. Molecular structure of 4-nitroimidazole, 2-nitroimidazole, 1-methyl-4-nitroimidazole, 1-methyl-5-nitroimidazole and imidazole. ....	59
Figure 4.6. Time-of-flight negative ion mass spectra in potassium collisions with 4-nitroimidazole (4NI), 2-nitroimidazole (2NI), 1-methyl-4-nitroimidazole (Me4NI), 1-methyl-5-nitroimidazole (Me5NI) at 30eV lab frame energy (15.7 and 16.3 eV available energy in the centre-of-mass, respectively). See text for details. ....	66
Figure 4.7. 4-nitroimidazole (4NI) branching ratios (fragment anion yield/total anion yield) of the main negative ions formed as a function of the collision energy in the centre-of-mass frame. See text for details.....	66
Figure 4.8. Time-of-flight negative ion mass spectra in potassium collisions with 4-nitroimidazole (4NI), 2-nitroimidazole (2NI), 1-methyl-4-nitroimidazole (Me4NI), 1-methyl-5-nitroimidazole (Me5NI) at 100 eV lab frame energy (62.6 and 64.5 eV available energy in the centre-of-mass, respectively). See text for details. ....	67
Figure 4.9. 1-methyl-4-nitroimidazole (Me4NI) branching ratios (fragment anion yield/total anion yield) of the main negative ions formed as a function of the collision energy in the centre-of-mass frame. See text for details.....	67
Figure 4.10. Time-of-flight negative ion mass spectra in potassium collisions with 4-nitroimidazole (4NI), 2-nitroimidazole (2NI), 1-methyl-4-nitroimidazole (Me4NI), 1-methyl-5-nitroimidazole (Me5NI) at 500 eV lab frame (330 and 340 eV available energy in the centre-of-mass, respectively). See text for details. ....	68
Figure 4.11. 1-methyl-5-nitroimidazole (Me5NI) branching ratios (fragment anion yield/total anion yield) of the main negative ions formed as a function of the collision energy in the centre-of-mass frame. See text for details.....	68
Figure 4.12. Time-of-flight negative ion mass spectra in potassium-imidazole (IMI) collisions at 30, 100 and 500 eV lab frame energy (12.8, 52.9 and 282 eV available energy in the centre-of-mass, respectively). See text for details. ....	70
Figure 4.13. Imidazole (IMI) branching ratios (fragment anion yield/total anion yield) of the main negative ions formed as a function of the collision energy in the centre-of-mass frame. See text for details. ....	70
Figure 4.14. Molecular structure of pyrimidine (Pyr). ....	74
Figure 4.15. Time-of-flight negative ion mass spectra in potassium-pyrimidine (Pyr) collisions at 30, 100 and 700 eV lab frame energy (13.8, 56.2 and 419.3 eV available energy in the centre-of-mass, respectively). See text for details. ....	79
Figure 4.16. Energy loss spectrum of K <sup>+</sup> ions measured in the forward direction in collisions of potassium atoms with pyrimidine (Pyr) at 111 eV lab frame energy (67.2 eV in the centre-of-mass system). See text for details.....	80
Figure 4.17. Pyrimidine (Pyr) branching ratios (fragment anion yield/total anion yield) of the main negative ions formed as a function of the collision energy in the centre-of-mass frame. See text for details. ....	82
Figure 5.1. Electron detachment cross-sections in the 50-7000 eV energy range for O <sub>2</sub> <sup>-</sup> collisions with N <sub>2</sub> . ....	87

Figure 5.2. Total electron detachment cross-sections for $O_2^-$ on $N_2$ (black squares) compared with previously published experimental results from Jalbert et al. (blue triangles) and Bennett et al. (violet circles), and a theoretical model from Jalbert et al. (green dash line). The red circles represent the total ionization cross-sections for the formation of $N_2^+$ and $N^+$ . See also the legend on the plot for other symbols. ....	89
Figure 5.3. Molecular structure of water ( $H_2O$ ) and pyridine ( $C_5H_5N$ ).....	93
Figure 5.4. Electron detachment cross-sections in the 10–4000 eV energy range for $O_2^-$ collisions with water (cyan diamonds) and pyridine (purple squares). ....	94
Figure 5.5. Comparison between electron detachment cross-section values and the relative cross-section for positive and negative ions formation in $O_2^- + H_2O$ collisions. The values are normalized to the maximum value. ....	96
Figure 5.6. Comparison between electron detachment cross-section values and the relative cross-section for positive and negative ions formation in $O_2^- + C_5H_5N$ collisions. The values are normalized to the maximum value. ....	96
Figure 5.7. Time-of-flight positive and negative ion mass spectra from $O_2^-$ -pyridine collisions at 500 eV lab frame energy. ....	98
Figure 5.8. Time-of-flight positive and negative ion mass spectra from $O_2^-$ -pyridine collisions at 1000 eV lab frame energy. ....	99

# LIST OF TABLES

Table 4.1. Assignment of the negative ions formed in potassium collisions with 4-nitroimidazole (4NI), 2-nitroimidazole (2NI), 1-methyl-4-nitroimidazole (Me4NI), 1-methyl-5-nitroimidazole (Me5NI), and imidazole (IMI). .....	64
Table 4.2. Calculated dipole moments obtained with HF/aug-cc-pvtz level of theory and vertical electron affinities (VEAs) obtained with HF/D95V level of theory, for 4-nitroimidazole, 1-methyl-4-nitroimidazole, 1-methyl-5-nitroimidazole and imidazole. ....	65
Table 4.3. Calculated highest occupied molecular orbitals (HOMOs) and lowest unoccupied molecular orbitals (LUMOs) for 4-nitroimidazole (4NI), 1-methyl-4-nitroimidazole (Me4NI), 1-methyl-5-nitroimidazole (Me5NI) and imidazole (IMI) anions obtained at the M06-2X/aug-cc-pvtz level of theory. ....	65
Table 4.4. Calculated lowest unoccupied molecular orbitals (LUMOs) for pyrimidine (Pyr) and pyrimidine (Pyr) in the presence of a potassium atom in the perpendicular geometry inside the pyrimidine ring. Energies in eV. ....	78
Table 4.5. Negative ions formed in potassium collisions with pyrimidine (Pyr). ....	82
Table 5.1. Present experimental results of total electron detachment cross-sections for N <sub>2</sub> in collisions with O <sub>2</sub> <sup>-</sup> . ....	88
Table 5.2. Experimental electron detachment cross-sections for O <sub>2</sub> <sup>-</sup> collisions with water and pyridine. ....	95
Table 5.3. Tentative assignment of negative and positive ions formed in O <sub>2</sub> <sup>-</sup> collisions with water (H <sub>2</sub> O). ....	97
Table 5.4. Tentative assignment of negative and positive ions formed in O <sub>2</sub> <sup>-</sup> collisions with pyridine (C <sub>5</sub> H <sub>5</sub> N). ....	98



# ACRONYMS AND SYMBOLS

<b>AD</b>	Auto-detachment
<b>amu</b>	Atomic mass unit
<b>b</b>	Impact parameter
<b>BEIR</b>	Biologic Effects of Ionising Radiation
<b>BRs</b>	Branching ratios
<b>CEC</b>	Charge exchange chamber
<b>CEFITEC</b>	Centre of Physics and Technological Research
<b>CSIC</b>	Consejo Superior de Investigaciones Científicas
<b>CT</b>	Constant transmission
<b>CTSR</b>	Charge-transfer to shape resonances
<b>d</b>	Distance
<b>DBS</b>	Dipole bound state
<b>DCSs</b>	Differential cross-sections
<b>DD</b>	Direct detachment
<b>DEA</b>	Dissociative electron attachment
<b>DFT</b>	Density functional theory
<b>DNA</b>	Deoxyribonucleic acid
<b>DSB</b>	Double strand breaks
<b>e<sup>-</sup></b>	Single electron
<b>E<sub>0</sub></b>	Pass energy
<b>EA</b>	Electron affinity
<b>EA<sub>ad</sub></b>	Adiabatic electron affinity
<b>E<sub>av</sub></b>	Available energy
<b>E<sub>CM</sub></b>	Energy of the centre-of-mass
<b>E<sub>k</sub></b>	Kinetic energy
<b>E<sub>lab</sub></b>	Kinetic energy in the laboratory frame
<b>FWHM</b>	Full-width at half-maximum
<b>GC</b>	Gas cell
<b><math>\hat{H}</math></b>	Hamiltonian operator
<b>H<sup>•</sup></b>	Hydrogen radical
<b>H<sub>0</sub></b>	Non-perturbated Hamiltonian
<b>H<sub>11</sub></b>	Diabatic potential curves
<b>H<sub>12</sub></b>	Coupling factor
<b>H<sub>22</sub></b>	Diabatic potential curves
<b>H<sub>2O</sub><sup>•+</sup></b>	Water cation
<b>HCE</b>	Hollow cathode effect
<b>HEA</b>	Hemispherical energy analyser

<b>HOMO</b>	Highest occupied molecular orbital
<i>I</i>	Transmitted anion signal
<i>I<sub>0</sub></i>	Initial anion beam intensity
<b>ICRP</b>	International Commission on Radiological Protection
<b>IE</b>	Ionisation energy
<b>IMI</b>	Imidazole
<i>k</i>	Boltzmann constant
<i>k</i>	Electronic state
$K^+$	Cationic potassium
$K^+_{\text{hyp}}$	Hyperthermal cationic potassium
$K^0$	Neutral potassium
$K^0_{\text{hyp}}$	Hyperthermal neutral potassium
<i>l</i>	Effective path length
<b>LCAM</b>	Atomic and Molecular Collisions Laboratory
<b>LEE</b>	Low-energy electrons
<b>LNT</b>	Linear no-threshold
<b>LUMO</b>	Lowest unoccupied molecular orbital
<b>LZ</b>	Landau-Zener method
<i>m</i>	Mass
$M^{\#}$	Anionic transient state
<b>MCP</b>	Microchannel plate detector
<b>MDSB</b>	Multiple double strand breaks
<b>Me4NI</b>	1-methyl-4-nitroimidazole
<b>Me5NI</b>	1-methyl-5-nitroimidazole
$m_K$	Mass of potassium
$m_m$	Mass of the molecular target
<b>MO</b>	Molecular orbital
$NO^{\bullet}$	Nitric oxide radical
$O_2^{\bullet-}$	Superoxide anion
$OH^{\bullet}$	Hydroxyl radical
<i>P</i>	Gas pressure
<i>p</i>	Landau-Zener non-adiabatic transition probability
<b>PEPIPICO</b>	Photoelectron-photoion-photoion coincidence spectroscopy
<b>PET</b>	Positron emission tomography
<b>Pyr</b>	Pyrimidine
<b>QMS</b>	Quadrupole mass spectrometer
<i>r</i>	Spatial coordinates of the electron
<b>R</b>	Spatial coordinates of the nuclei
$R_c$	Crossing radius
<b>RNA</b>	Ribonucleic acid



<b>ROS</b>	Reactive oxygen species
<b>SC</b>	Scattering chamber
<b>SCF</b>	Self-Consistent Field
<b>SFS</b>	Sector field sweep
<b>SMC</b>	Schwinger multichannel
<b>SSB</b>	Single strand breaks
<b><i>T</i></b>	Temperature
<b><i>t</i></b>	Total flight time
<b><math>T_c</math></b>	Scattering chamber temperature
<b><math>t_{col}</math></b>	Collision time
<b><math>T_e</math></b>	Kinetic energy operator of the electrons
<b>THF</b>	Tetrahydrofuran
<b><math>T_m</math></b>	Operation temperature of Baratron gauge
<b><math>T_n</math></b>	Kinetic energy operator of the nuclei
<b>TNI</b>	Transient negative ion
<b>TOF</b>	Time-of-flight
<b><math>t_{vib}</math></b>	Vibrational time
<b>U</b>	Potential energy
<b>UV</b>	Ultra-violet
<b><i>V</i></b>	sum of potential
<b><i>V</i></b>	Electric field
<b><i>v</i></b>	Relative velocity
<b>VAE</b>	Vertical attachment energy
<b>VEA</b>	Vertical electron affinity
<b>VFRs</b>	Vibrational Feshbach resonances
<b><math>V_p</math></b>	Voltage applied between analyser hemispheres
<b>VUV</b>	Vacuum ultra-violet
<b>XPS</b>	X-ray photoelectron spectroscopy
<b><i>z</i></b>	Charge of the particle
<b><math>\alpha</math></b>	Experimental correction factor
<b><math>v_r</math></b>	Radial velocity
<b><math>\pi^*</math></b>	Antibonding orbital
<b><math>\sigma^*</math></b>	Antibonding orbital
<b><math>\sigma_{exp}</math></b>	Electron detachment cross-sections
<b><math>\Phi(r; R)</math></b>	Adiabatic electronic wavefunctions
<b><math>\Psi(r, R)</math></b>	Total wavefunction
<b><math>\Omega_k(R)</math></b>	The nuclear wave function
<b><math>\Delta E</math></b>	endoergicity
<b>2NI</b>	2-nitroimidazole
<b>4NI</b>	4-nitroimidazole



# CHAPTER 1

## INTRODUCTION

### 1.1 Motivation

#### 1.1.1 Cancer

Cancer represents a leading cause of death in developed and developing countries [1,2]. According to the more recent statistics it was estimated that 18.1 million people were diagnosed with a cancer disease and 9.6 million died from cancer in 2018, meaning that about 1 in 6 deaths worldwide is due to cancer. The World Health Organization and the International Agency for Cancer Research predicts an increase up to 29.5 million of new cancer cases in 2040 [3], which makes it one of the most important obstacles to life expectancy around the world in the 21<sup>st</sup> century [2]. The numbers also reveal that around 70% of deaths from cancer occur in less economically developed countries. In Portugal, the incidence of new malignant tumour cases has increased around 3% per year [4]. The most recent data reported in 2010 show an incidence rate of 441.9/100 000, with 67% of cancers diagnosed at ages greater than 60 years old [4,5].

Briefly, this noncommunicable disease is characterized by an uncontrolled proliferation of abnormal cells (tumour cells), which have suffered several mutations resulting into a malignant tumour. These tumour cells can also migrate to different parts of the body through the blood flow or lymph in a process named as metastasizing. Metastases become more difficult to control and are considered a major cause of death from cancer. The reasons for cancer occurrence are many and varied, and some of which are still unknown. However, in the last decades, some efforts have been made in order to understand the major risks factors for cancer, especially through epidemiologic studies. The possibilities of developing a neoplasm disease are related to a combination of genetic and external factors. The external factors can be classified in three different groups: physical

carcinogens (such ionising radiation (e.g. UV)), chemical carcinogens (such as asbestos, tobacco smoke, food and water contaminants) and biological carcinogens (such as infections by virus and bacteria) [3,6]. It is now identified that around 90-95% of the most cancer cases are associated with lifestyle and environment [7]. About 30% of cancer deaths are due to behavioural and dietary risks, such as, high body mass index, low fruit and vegetable intake, lack of physical activity, tobacco and alcohol use [6,8]. Therefore, it becomes urgent to search and find strategies to fight against this epidemic disease, either through early diagnosis or new treatment methods.

In the next subchapters we will focus on the role of radiation in living organisms especially due its capacity to induce at the molecular and atomic levels alterations in biomolecules.

### **1.1.2 Effects of ionising radiation in biological systems**

The biological organisms are continually being exposed to electromagnetic radiation. This interaction with radiation can result from natural sources, such as food (potassium-40 is a radioactive isotope present in bananas), sun, cosmic radiation, minerals and materials found in the ground (e.g. uranium-238, radon-222, radium-226) and even living organisms (e.g. radioactive carbon-14 used to dating organic material). Besides this natural exposure, we can also be a target to man-made radiation which comprises essentially the radiation used for medical diagnosis and treatment, atmospheric nuclear testing, wars, nuclear power production, and finally accidental nuclear disasters as Chernobyl and Fukushima [9].

The radiation sources can be divided in two main groups according to the energy and the effects they produce when interacting with matter. If we look at the electromagnetic spectrum, for lower energies we find radiation sources like microwaves, infrared and visible radiation which are considered as non-ionising radiation. At higher energies (shorter wavelengths) we find UV radiation, X-ray and gamma radiation, termed ionising radiation. Other particles like alpha, electrons, neutrons and heavy ions can also be treated as ionising radiation given the spectral energy ranges they are commonly used. Ionising radiation is capable, when interacting with matter, to ionise it through direct and indirect processes producing several species along the ionisation track [10]. This occurs when the energy of incident radiation transferred to the target is higher than the ionisation energy of atoms and molecules. The ionisation energy is the minimum energy necessary to ionise an atom and ranges from few eV for alkali atoms to 24.6 eV for helium (noble gas) [11,12]. Ionising radiation is very important and useful in different fields, such as industry, agriculture and in medicine. In medical applications it can be used for diagnosis (diagnostic radiology and nuclear medicine) and treatment of diseases particularly cancer-related diseases (radiotherapy, brachytherapy, among others).

Besides the benefits and positive effects about the use of ionising radiation, especially in medical applications, it can also cause adverse health effects, even when we are dealing with low-dose ionising radiation [13,14]. According to the US National Academy of Sciences BEIR VII Committee

[15], approximately 50% of cancer patients are treated with ionising radiation. Yet, the most important effect in humans resulting from low doses of radiation is the possibility to induce cancer [16]. So, we are facing an antagonistic effect of using ionising radiation. Therefore, recommendations from the dedicated Committees is the determination of the effects of low-dose ionising radiation on DNA damage, especially the long-term effects. Epidemiological studies using the survivors of Hiroshima and Nagasaki atomic bombs in 1945 have shown that there is a relationship between cancer incidence and radiation doses in organs. Using this data is possible to extrapolate the effects of low-dose radiation from exposure to high-doses based on a linear no-threshold (LNT) model [16,17]. This model has been used to define numerous international rules and standards of radiation protection (ICRP) [18]. Other nuclear accidents, like Chernobyl (April 1986) and Fukushima (March 2011) were also used to associate the risk of developing cancer diseases (as leukaemia, lymphoma, thyroid cancers, skin cancers, sarcomas, lung and breast carcinomas) in long-term after exposure to high doses of radiation [19]. Many other studies regarding the secondary effects of ionising radiation after the use in some medical treatments and even, after some diagnostic scans, were carried out in order to determine the main causes produced by exposure to very low radiation doses. These are extremely important to assess because during these procedures not only the tumour tissues are affected but also healthy tissue [18,20–22].

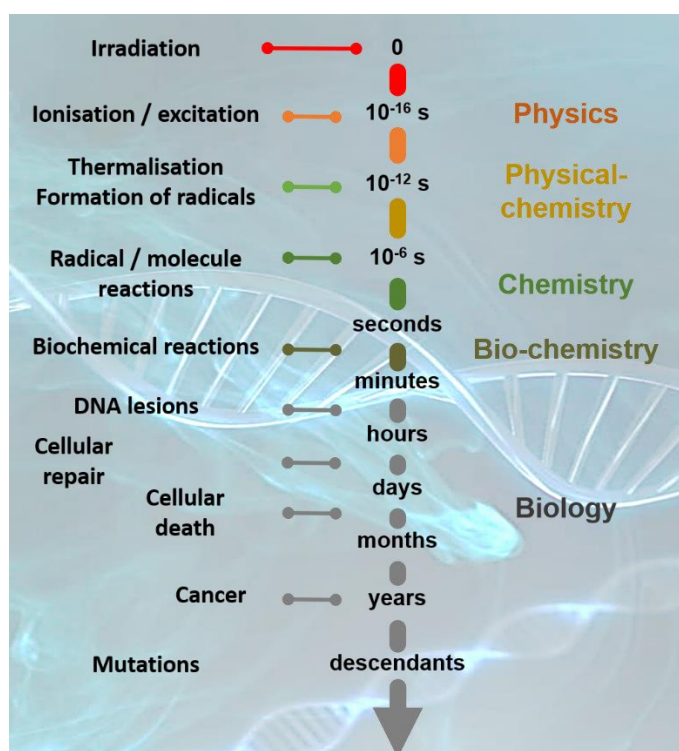


Figure 1.1. Chronological diagram of radiation-induced damage.

Briefly we can describe the ionising radiation interactions with living organisms on a time scale. At the time a primary high-energy ionising radiation interacts with biomolecules and tissues

generates multiple sequences of physical and chemical reactions, within the early stages of irradiation ( $\sim 10^{-16}$  s), resulting mainly in electronic excitation and ionisation of the molecular constituents, with subsequent bond breaks creating large amounts of secondary electrons and radicals. The damage in DNA molecule created by these secondary species are characterized by single strand breaks (SSB), double strand breaks (DSB), clustered damage, base damage and loss of the supercoiled helix integrity. The consequences of these injuries in long-term (biological stage) can lead to several mutations, chromosome aberrations, cell inactivation and other effects that compromise the genome integrity which may result in cancer [23–26] (figure 1.1). Given this complexity, a complete understanding of these processes represents a challenging task.

### 1.1.3 Impact of low-energy electrons in biomolecules

The impact of high-energy ionising radiation with biosystems generates a large amount of different secondary species along the radiation track. As referred before, the ionisation processes triggered by the primary beam create secondary electrons in abundance which interact with biological tissue causing damage in biomolecules, especially in DNA. In fact, it is well-established that low-energy electrons (LEE) and the radicals originated by them are the most responsible for the damage in DNA and other cell molecular components. Typically,  $5 \times 10^4$  secondary electrons (below 20 eV) are produced per MeV of primary radiation [27–29]. Along the track and due to successive inelastic interactions (see figure 1.2) with the medium, these secondary electrons transfer their kinetic energy until they reach a near-zero energy (thermalisation) undergoing solvation [30,31]. At this energy range, different electron induced processes can happen yielding different levels of molecular alterations, either producing ionisations (energies typically above 7 eV), bond rupture or resonant attachment, among several others.

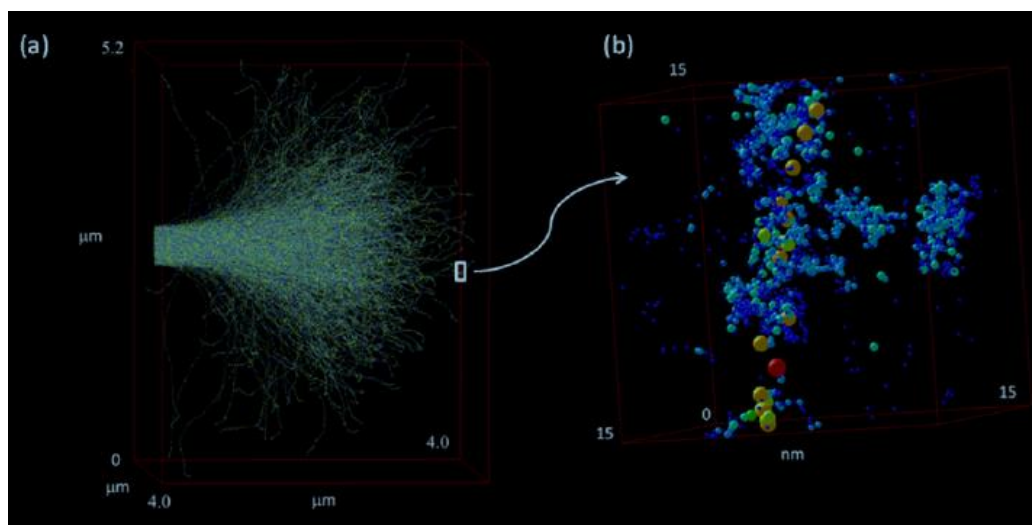


Figure 1.2. Single electron tracks simulation in liquid water. (a) Electrons with 10 keV incident energies are slowed down by successive interactions with matter (e.g. elastic scattering ●, rotational excitation ●, vibrational excitation ●, electronic excitation ●, neutral dissociation ●, ionisation ●, and electron attachment ●). Image taken from ref. [32].

### 1.1.3.1 Direct effects: dissociative electron attachment

Electron attachment can occur even at very low-energies as close to 0 eV. It is defined as a direct electron capture by a target molecule leading to formation of a transient negative ion (TNI) state with a lifetime of  $\sim 10^{-16}$  s [33]. The process is considered as a resonant scattering, which means that the energy of the incident electron must be exactly the energy necessary to reach a quasibound state of the molecular target (resonance) [34]. If there is no energy lost during the interaction, which means that the energy of the incident electron is roughly speaking the same of the scattered electron (excluding rotational excitation), the process is termed elastic. However, the scattering mechanism is considered inelastic where the energy of the incident electron is higher than the energy of the scattered electron. In the latter case, the formation of a TNI represents a transition from the electronic ground state of the neutral molecule ( $ABC + e^-$ ) to the potential energy surface of the molecular anion ( $ABC^-$ ) and can be described following the Franck-Condon transitions. The TNI has a very short lifetime which depends on the size of the molecule as well as the width of the resonance according to the Heisenberg's uncertainty principle  $\Gamma \sim \frac{\hbar}{\tau}$ , where  $\Gamma$  is the energy width of the resonant anionic state,  $\hbar$  is the Plank's constant/ $2\pi$  and  $\tau$  is the lifetime of the anionic state. As the TNI is very unstable it can decay through three different channels: radiative stabilization (equation 1.1), auto-detachment (AD) (equation 1.2) and dissociative electron attachment (DEA) (equation 1.3).



$(ABC)^{-\#}$  means TNI with an excess of internal energy. The formation of a stable molecular anion via radiative stabilization is much less likely and happens for time scales much longer than the other two processes ( $10^{-12}$  s) which means it is not a competitive channel. Auto-detachment consists on the ejection of an extra electron from the TNI without dissociation. In the case of an inelastic mechanism the incoming electron may leave the target molecule in an electronic or vibrational excited state. This is a competitive process to DEA, which occurs when the TNI decay resulting in dissociation with production of anions and one (or more) neutral species (equation 1.3). DEA typically occurs in the timescale of  $10^{-14}$  s to  $10^{-12}$  s [34]. Briefly, the TNI dissociates through the instability created by the extra electron, which is initially captured into an unoccupied anti-bonding molecular orbital, has the capability to change the intramolecular potential and adds an excess of internal energy (figure 1.3). DEA depends on the energy of the incoming electron and can also be site and bond selective, i.e. this process can selectivity occur whether the electron attaches to specific sites in the atoms and bonds of a molecule [35].

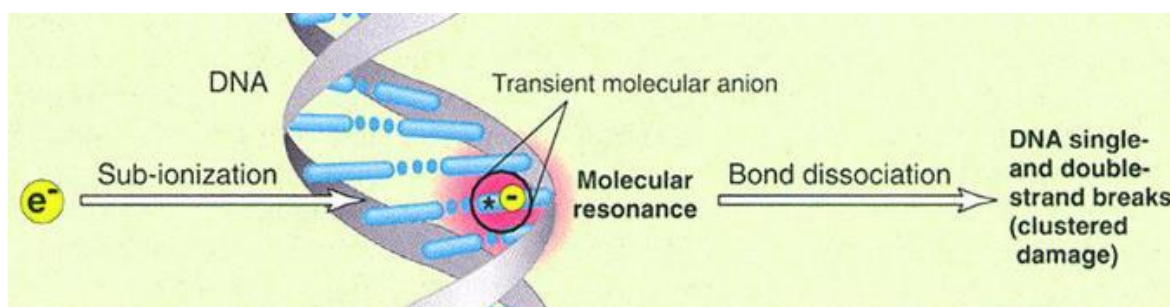


Figure 1.3. Formation of a temporary negative ion in the DNA molecule after the capture of low-energy electrons that which leads to DNA strand breaks. Taken from ref. [36].

During the last decades much effort has been given to the investigation of LEE impact with molecules, with considerable interest to biomolecules (e.g. DNA bases and amino acids). In 2000, a pioneering study performed by Boudaïffa and co-workers demonstrated that electrons with energies up to 20 eV are capable to induce SSB and DSB in plasmid DNA in ultra-high vacuum conditions (see figure 1.4). These authors have also observed that DNA damage is highly dependent on the initial kinetic energy of the incident electron, particularly below 15 eV, and even that SSB and DSB yields in the region of 7–10 eV incident electrons are one to two orders of magnitude larger than those for 10 to 25 eV photons. Therefore, the mechanisms of DNA damage depend not only on the quantum of energy absorbed but also on the nature of the particle that deposits the energy [37]. Further to these findings, Huels *et al.* reported that besides SSB and DSB also multiple double strand breaks (MDSB) occur from interactions with electrons below 100 eV, showing a strong monotonic increase above 30 eV, however less intense than in SSBs and in DSBs [38]. These authors concluded that MDSB are related with strand breaks clusters (nano-clusters) involving multiple successive interactions of one single electron in different sites of the supercoiled DNA. After these studies, several investigations were and are being performed in order to better understand the DEA processes operative in both gas and condensed-phases.

Studies using DNA sugars [39,40] and bases [35,41,42] showed that electrons with very low energies ( $< 3$  eV) attack the molecular target decomposing it, especially by the loss of H atoms, leading to formation of the dehydrogenated parent anion. It is being reported that a simple bond cleavage can be related to the triggering of other bond cleavages resulting in degradation of an entire cyclic structure. In most of the cases, it has been reported that this decomposition is remarkably bond and site selective [35,39,42,43]. In some studies, in order to investigate how certain dissociation channels may be quenched as a function of the electron energy, deuterated and/or methylated compounds specific sites in molecules have been used. Additionally, studies using slow electrons as a tool to control chemical reactions in condensed phase has also been reported. Balog and Illenberger performed studies in thin films of 1,2- $C_2F_4Cl_2$  molecules by setting the electron beam energy to values below 3 eV which resulted in a complete modification into molecular chlorine and other products. This effect is based on both selectivity and energy dependence and is triggered by a DEA



process [44]. Electron irradiation of thymine and halogen-substituted nonamers films [45] and pyrimidine [46] have shown that the TNI contributes significantly via DEA to molecular dissociation at low energies.

Besides the extremely importance to investigate DEA processes in DNA and cell components, other molecules have attracted the interest of the scientific community because their electron scavenging properties (e.g. halogenated compounds) make them very useful as radiosensitisers in medical treatments. This will be discussed in Section 1.1.5.

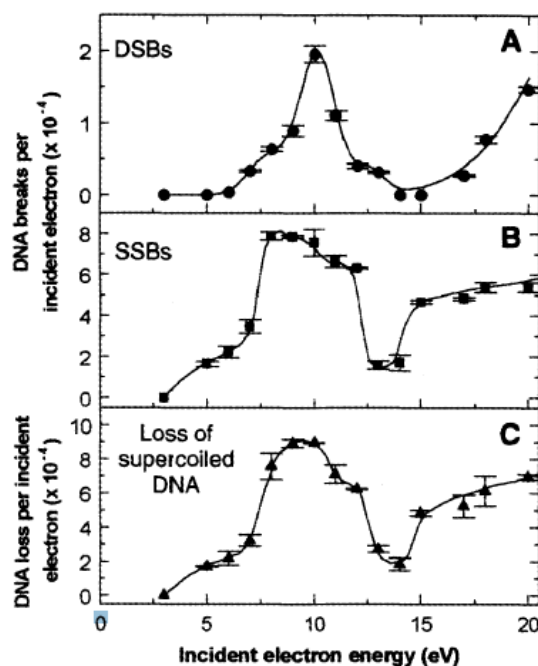


Figure 1.4. Measured quantum yields, per incident electron (3 to 20 eV), for the induction of DSBs (A), SSBs (B), and loss of the supercoiled DNA form (C), in DNA films. Taken from ref. [37].

### 1.1.3.2 Indirect effects: production of highly reactive species

As described in the previous paragraphs, secondary electrons are capable not only to induce directly alterations in the structure of biomolecules, with focus on DNA constituents, but are responsible to induce changes through indirect effects. The indirect effects of secondary electrons are related to the production of free radicals, atoms or molecules with unpaired electrons, after interaction with other cell components (DNA, water, oxygen and proteins). Most of these radicals are created from the interaction of the incoming radiation with the water molecule (water radiolysis), since around 80% of the cell is water [26]. These species are highly reactive and are responsible to permanent damage of the target molecule. It is assumed that one third of the damage in the genome is caused by direct effects whereas two thirds by indirect effects [36].

Thus, investigating the indirect mechanisms by LEE is essential to a comprehensive knowledge of the damage produced at the molecular level. Experiments were carried out using biomolecules

surrounded by water [31] and thin films of short single DNA strands embedded in a water medium [47,48]. Such studies have proved that the presence of water around DNA changes the decomposition channels and the SSB and DSB yield functions. Furthermore, theoretical studies have demonstrated that DNA solvation leads to an enhancement in electron capture with energies near zero eV or lower via the modification of adiabatic electron affinity of solvated DNA bases in water [49,50]. As result of water radiolysis, several reactive species are formed, such as hydroxyl radicals ( $\text{OH}^\bullet$ ), hydrogen radicals ( $\text{H}^\bullet$ ), as well as electrons (known as pre-hydrated electrons) [51], schematically represented in figure 1.5. It is assumed that these species are responsible for most of the damage induce in cells genome, leading to severe injuries, essentially because they have high electron affinities and can produce the excision of hydrogen atoms from the biomolecules [30,52]. When high-energy ionising radiation interacts with water molecules, ionisation processes are initiated producing water radical cations and electrons (equation 1.4). This reaction rapidly transfers electrons to DNA causing rupture and production of transient anions. As  $\text{H}_2\text{O}^{\bullet+}$  is a strong acid it immediately reacts with the medium components (equation 1.5) or can migrate over distances of a few molecular diameters by resonant electron transfer and produce hydroxyl radicals and solvated electrons (equation 1.6). Moreover, electronically excited states of water can also be produced and dissociate into H and OH radicals (equation 1.7) [53][54].



These are some examples of the interaction of radiation with water but there are also several other channels related to the indirect effects of LEEs. One of the most important reactions is the production of oxygen-derived free radicals (the so-called reactive oxygen species: ROS), which are short-lived and highly reactive. The hydroxyl radical ( $\text{OH}^\bullet$ ), the superoxide anion ( $\text{O}_2^{\bullet-}$ ) and the hydrogen peroxide ( $\text{H}_2\text{O}_2$ ) are some of the ROS [55]. At low levels, the ROS generation happens under normal physiologic conditions to guarantee the good cellular functioning by regulating the expression of specific genes and acting in the maintenance of redox balance of the organism. However, if a burst occurs in the normal functioning of cells, through high-energy irradiation or in cancer for instance, abnormal high levels of ROS are generated which can result in oxidative stress. Excess cellular levels of ROS can cause damage to proteins, nucleic acids, lipids, membranes and organelles such as mitochondria with severe consequences for organism [56,57]. Therefore, the high levels of ROS in cellular microenvironment can be harmful to healthy cells or can be used as intermediate species in tumour treatments using radiation [58,59].

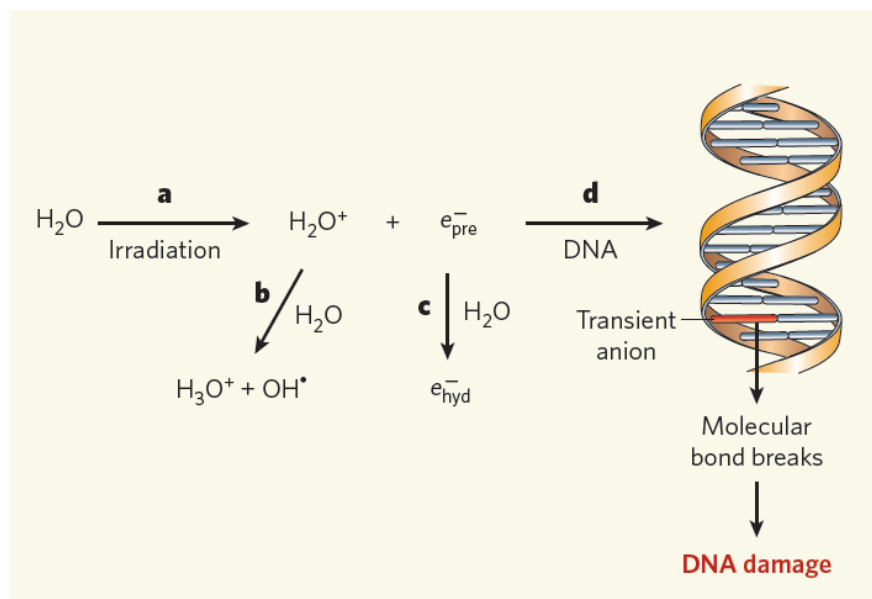
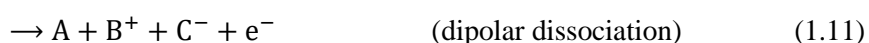
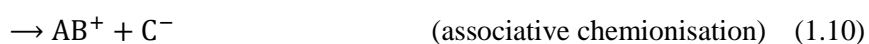
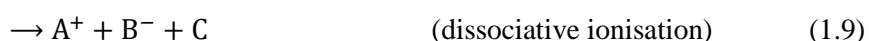


Figure 1.5. DNA damage caused by indirect effects (water radiolysis). Taken from ref. [60].

#### 1.1.4 Electron transfer processes in biomolecules damage

In the previous sections it was briefly discussed the role of direct electron attachment and the consequent dissociation processes of molecules. However, many elementary collisional processes are not direct electron impact but rather depend upon electron transfer, since free electrons have very limited lifetimes, losing their energies in successive inelastic collisions and reacting with or being solvated by surrounding molecules. In this context, the studies on molecular damage by free electron attachment processes must be complemented with studies on electronic capture of “bound” electrons (as in atom-molecule and ion-molecule collisions).

In atom-molecule collisions the electron is not free but weakly bounded to a neutral atom, which acts as an electron donor (A). This represents a better approximation to what may happen in the physiological environment. In this type of collision, the presence of an electron donor makes the collision system a three-body system, where the projectile significantly changes the fragmentation pathways of the target molecules (BC). Briefly, it is a collision system composed by a projectile which transfers a valence electron to the molecular target when reaching a given distance from the target producing a cationic donor and a transient molecular anion [61–63]. Thereupon, several channels can be opened as described in the following equations:



These processes can be characterised by two physical properties: the ionisation energy (IE) of the electron donor atom (A) and the electron affinity (EA) of the target molecule (BC). EA is defined as the energy difference between the neutral (BC) and the anion ( $BC^-$ ), termed vertical electron affinity (VEA) [34] and if it is related to their respective ground states, then is termed  $EA_{ad}$ , adiabatic electron affinity. In this case it is termed adiabatic electron affinity. It is also important to mention the endoergicity ( $\Delta E$ ) of a reaction, which is (at large atom-molecule collisions) the difference between the IE of the donor and the EA of the target, as shown in equation 1.12. If the ionisation energy is higher than the electron affinity, the endoergicity is positive, meaning that the process is endothermic.

$$\Delta E = IE(A) - EA(BC) \quad (1.12)$$

For large atom-molecule distances the ionic potential energy surface lies above the covalent. Due to the Coulomb potential there is a crossing point at small distances at which both potential energy surfaces have the same value. The crossing distance  $R_c$  is inversely proportional to the endoergicity of the reaction. Consequently, in a reaction where it is formed a cation and an anion (ion-pair formation) only the lowest ionic state will be involved. On the other hand, it should be noted that in these processes the electron transfer is only possible between configurations of the same symmetry and multiplicity [63–65]. Indeed, the presence of a third body (cationic donor projectile post-collision) in the collisional mechanism may yield a different fragmentation pattern after the TNI decays in contrast to DEA experiments. In fact, this was verified by Antunes *et al.* [66] in a study using nitromethane as a molecular target, the formation of a parent anion ( $CH_3NO_2^-$ ) which is not detected in DEA experiments. Other studies developed in the Lisbon group have demonstrated the ability to change the probability of certain reaction channels and to induce the formation of new dissociation pathways by electron transfer in potassium-molecule collisions. Ferreira da Silva *et al.* performed studies on different amino acids describing the side chain in the fragmentation pattern comparing the ionic yields. In some of them the dehydrogenated parent anion is one of the most intense fragments and possibly leading to the formation of metastable fragments (at higher collision energies) [67,68]. Dissociative ion-pair formation in collisions of fast potassium atoms with benzene and fluorobenzene was also studied by Limão-Vieira *et al.* [69]. Many studies performed by Almeida *et al.* have shown the importance of a third body in the “stabilisation” of the TNI in the collisional system. By tuning the collision energy of the hyperthermal neutral potassium beam in collisions with methylated and deuterated pyrimidine molecules Almeida *et al.* have showed that  $H^-$  loss is site and bond-selective [70,71]. Furthermore, they also studied D-Ribose [72], THF [73] and uridine [74] sugar where major enhancements in the formation of  $OH^-$  and  $O^-$  were observed compared with DEA experiments. Investigation on thymine and uracil molecules by Almeida *et al.* [75] also provide information about the dissociation channels and the fragmentation pattern by electron transfer as well as  $CNO^-$  formation as the major ring breaking anionic product for both molecules.

Following these studies, the focus of this thesis is the study of electron transfer processes making use of a crossed molecular beam setup where the electron donor is a neutral alkali atom (potassium atom) due to its low ionisation energy ( $IE(K) = 4.34 \text{ eV}$ ). Although neutral potassium does not exist in the physiological environment, it is a good candidate to mimic the charge transfer mechanism in DNA damage caused by LEEs. A set of measurements were performed for molecular targets of the nitroimidazoles family, including methylated compounds and imidazole. A comprehensive comparison was also established between DEA results and the results are thoroughly presented in this thesis. These studies were fully performed in the Atomic and Molecular Collisions Laboratory (LCAM) in Lisbon.

Furthermore, and considering the importance of what has been described in Section 1.1.3.2, ion-molecule collisions were also performed at Laboratorio de Interacción Radiación-Materia at CSIC in Madrid. In order to study such processes, we have developed and improved a novel crossed beam experimental setup to investigate negative and positive ion formation as well as cross-sections from charge transfer processes between the superoxide anion ( $O_2^-$ ) as electron donor and isolated molecules,  $N_2$ , water and pyrimidine as targets.

### 1.1.5 Radiosensitisers

Many cancer diseases are treated using ionising radiation through radiotherapy. The microenvironment of some solid tumours is characterised by regions of low oxygen (hypoxia), which plays a fundamental role in tumour progression. Tumour hypoxia arises from the high rate of tumour growth that cannot be sustained by a limited oxygen supply (the so-called “oxygen effect”). Hypoxia is directly related with aggressiveness of the tumour, and resistance to all available sorts of cancer treatment, including chemotherapy, radiotherapy and indirectly surgery [76,77]. The radiosensitisers used in radiotherapy to enhance tumour control of radioresistant hypoxic tumours are called electron-affinic molecules. However, the detailed molecular mechanism of actual radiosensitisation is still unknown. A working hypothesis is that these molecules undergo redox reactions inside the cells that are deficient in oxygen, and that the nitroimidazole ring facilitates reduction via the formation of radical anions [78]. In particular, the 5-nitroimidazole, nimorazole was shown to be effective in several clinical trials and it has been used in routine treatments of head and neck cancer in Denmark [79,80].

Feketeová and co-workers have reported on the formation of radical ions from radiosensitisers using different spectroscopy techniques [43,81–84]. They have concluded that low-energy electrons (0–8 eV) effectively decompose 4-nitroimidazole and two methylated isomers via DEA. The observation that neutral and radical anions are formed via DEA with high efficiency already at threshold (0 eV), shows the significant importance of the study of the molecular mechanisms involved in these reactions and emphasises the implications of that for the development of

nitroimidazole-based radiosensitisers in tumour radiation therapy. Yu and Bernstein demonstrated that the decomposition of three nitroimidazole model molecules following electronic excitation generates NO as an initial decomposition product at the nanosecond laser excitation wavelengths, with vibrational warm and rotational cold distributions of the NO product, which are independent of excitation wavelengths [85]. Some other studies using halogen-modified nucleic acids (such as 5-bromouridine, 5-fluoroacil, 5-chlorouracil, etc.) have been suggested as the most promising radiosensitisers for targeted therapies [86–89].

## 1.2 Outline of the Thesis

The present doctoral thesis describes the studies on interaction of low-energy electrons via charge transfer processes with different molecular targets. To pursue this objective, two different cross beam setups were used:

- (1) To investigate atom-molecule collisions an hyperthermal neutral potassium (K) beam was used as electron donor. The molecular targets studied were 4-nitroimidazole and methylated-derived, imidazole and pyrimidine.
- (2) To study ion-molecule collisions, the projectile used was a superoxide ( $\text{O}_2^-$ ) anion. The molecular targets studied were nitrogen molecule, water and pyridine.

This thesis is organized in six chapters as follows:

- **Chapter 1:** It is an introduction to the thesis presenting the main motivation and a state-of-the art for the presented scientific research.
- **Chapter 2:** It discussed some fundamental aspects of atom and ion-molecule collision theory used to support the analysis of the results.
- **Chapter 3:** It is presented and comprehensively described the experimental apparatus used to perform electron transfer experiments in both laboratories, Lisbon and Madrid.
- **Chapter 4:** It contains the experimental results obtained in electron transfer experiments between neutral potassium and 4-nitroimidazole and methylated compounds, imidazole and pyrimidine, as well as a comprehensive literature review, analysis and discussion results.
- **Chapter 5:** It contains the experimental results obtained in electron transfer experiments between the negative oxygen ion and the nitrogen molecule, water and pyridine as well as a comprehensive literature review, analysis and discussion of results.
- **Chapter 6:** It is a conclusion summarizing the results and some ideas and suggestions for future work that can complement the present research.





# CHAPTER 2

## COLLISION THEORY IN ELECTRON TRANSFER PROCESSES

In this chapter it will be introduced the principal theoretical aspects about electron transfer processes. Firstly, it will be discussed the generic fundamentals about the simplest case in collisions between two particles referring the Born-Oppenheimer approximation. Ion-pair formation will be also explained based on the Landau-Zener formalism. Thereafter, atom-molecule collisions will be explained focusing on diatomic molecules. Finally, some important notions will be expounded regarding collisions between ions and molecules, which constitutes the second part of this thesis dedicated to the experimental results. It is important to point out that the molecules studied in this thesis are more complex than the cases presented in this chapter. However, theoretical descriptions given in the next sections represent useful guiding concepts to analyse and explained most of the experimental results obtained in the thesis.

### 2.1 Two-Particles Collision

In collisions between two particles in their ground states two main processes can take place: the elastic and inelastic scattering. Let us consider as simplification the atom-atom collision case. The elastic scattering occurs when kinetic energy is transferred from an atom to the other yielding the same two atoms in their original electronic states. The inelastic scattering refers to the collision resulting in differences in final electronic states of the atoms. Here it will be discussed the case of electron transfer interactions, which comprises an electron transfer from a donor atom to an acceptor

atom with possible electronic excitation of the target. Equation 2.1 represents schematically this process.



Where A is the donor atom, B is the acceptor atom and \* means electronic excited. Equation 2.1 represents an ion-pair formation process, where after the interaction a cation and an anion are produced. The interaction between two atoms in a collision can be described through the time-dependent Schrödinger equation [61,62], as in equation 2.2:

$$\hat{H}\Psi(r, R) = i\hbar \left( \frac{d\Psi(r, R)}{dt} \right) \quad (2.2)$$

In this equation,  $\hat{H}$  is the Hamiltonian operator,  $\Psi(r, R)$  is the total wavefunction of the atom-atom system,  $r$  is the spatial coordinates of the electron and  $R$  of the nuclei. The Hamiltonian can be described through three components, the  $T_n$  (kinetic energy operator of the nuclei),  $T_e$  (kinetic energy operator of the electrons) and  $V$  is the sum of potential between the particles involved in the system that depends parametrically on the nuclear coordinates, as described in equation 2.3.

$$\hat{H} = T_n + T_e + V \quad (2.3)$$

Since the collisional systems can be much more complex than just two single particles interacting, it is necessary to find proper approximations to the solution of the Hamiltonian. In the next paragraphs it will be discussed the Born-Oppenheimer approximation. This approximation considers the nuclear motion and the electronic motion as two independent parameters. Therefore, the total wave function  $\Psi(r, R)$  can be expressed as a complete, orthogonal set of adiabatic electronic wavefunctions  $\Phi_k(r; R)$  that depend parametrically on the nuclear coordinates  $R$ . In other words, separating this wavefunction into a nuclear and electronic wavefunction [61,63,90,91]. The total wavefunction can now be defined according to equation 2.4.

$$\Psi(r, R) = \sum_k \Phi_k(r; R) \cdot \Omega_k(R) \quad (2.4)$$

in which  $\Omega_k(R)$  is the nuclear wave function associated with each electronic state  $k$ . Consequently, the Born-Oppenheimer approximation comprises two main assumptions: the nuclear motion can be considered as a classical trajectory  $R(t)$  which considers that the nuclei is moving as a function of the final state of the electrons, and it is possible to state that the nuclei are fixed relative to the electrons' motion because they are much more massive. Considering this, the Hamiltonian can be rewritten just as an electronic Hamiltonian ignoring the  $T_n$  parameter as follows:

$$H' = T_e + V \quad (2.5)$$

and, equation 2.2 can be modified as in equation 2.6, where  $E_{n,R}$  are the electronic levels associated with adiabatic electronic wavefunctions  $\Phi_k(r; R)$ .

$$(T_e + V(r; R)). \Phi_k(r; R) = E_{n,R} \Phi_k(r; R) \quad (2.6)$$

In this first approximation, it is considered that the motion of nuclei does not exist, this means they are kept at a constant mutual distance. Additionally, if the nuclei are considered to move slowly, the Born-Oppenheimer approximation continues to be valid. But this situation only happens when the electronic state will adiabatically follow the motion of the nuclei, which means that electrons will adjust themselves according to the motion of nuclei reaching an equilibrium. In this way equation 2.6 can be adjusted considering the parameter  $R(t)$  as a function of time (equation 2.7).

$$(T_e + V(r; R)). \Phi_k(r; R) = E_n(R) \Phi_k(r; R) \quad (2.7)$$

The function  $\Phi_k(r; R)$  is an eigenfunction of (2.3) however it is not an eigenfunction of (2.5). This can be solved by making use of perturbation theory, and so, a set of eigenfunctions  $\Theta_n(r; R)$  can be obtained through the use of  $\Phi_k(r; R)$  [61]. The total wavefunction  $\Psi(r,R)$  can also be expanded as in equation 2.8.

$$\Psi(r, R) = \sum_n a_n \Theta_n(r; R) = \sum_n a_n \Phi_k(r; R) \cdot e^{-\frac{i}{\hbar} \int_0^t E_n(R) dt} \quad (2.8)$$

From equation 2.2 and 2.8 the parameter  $a_n$  can be obtained through equation 2.9.

$$a_n = a_j v_r \left\langle \Phi_n \left| \frac{\partial}{\partial R} \right| \Phi_j \right\rangle e^{-\frac{i}{\hbar} \int_0^t (E_j - E_n) dt} \quad (2.9)$$

Where  $v_r$  is the nuclear radial velocity and can be defined as in equation 2.10.  $\Delta R$  is a characteristic length of the system and it is the responsible for the non-adiabatic coupling between the adiabatic states [61,63,66,90].

$$v \left\langle \Phi_n \left| \frac{\partial}{\partial R} \right| \Phi_j \right\rangle \approx \frac{v}{\Delta R} \quad (2.10)$$

Applying the Heisenberg uncertainty principle to this system we can obtain:

$$\Delta E \cdot \frac{\Delta R}{\hbar v} \gg 1 \quad (2.11)$$

When this condition holds, the adiabatic states are stationary or quasi-stationary and  $E_n(R)$  represents the adiabatic potential energy surfaces that regulate the motion of the nuclei. If this condition is not verified, there is a strong non-adiabatic coupling and the width between the energy levels is comparable to the energy uncertainty and making possible the non-adiabatic transitions between adiabatic states. This is a situation where it is possible to observe ion-pair formation in the case of electron transfer processes in atom-atom collisions [61,63,66,90].

In the previous paragraphs we briefly described the atom-atom collisions in an adiabatic framework. Next, we will discuss the diabatic approach. In the diabatic framework the two atoms involved in the collision are moving so fast that there is not enough time to interact with each other, and so, the electronic states maintain the same character independently of the nuclear distance  $R$ . Let us make use of an example of a collision between an alkali atom (A) and a halogen (B). The collisional system  $A + B$  can be described by two stationary states, the ionic,  $|\varphi_i\rangle (A^+ + B^-)$  and the covalent,  $|\varphi_c\rangle (A + B)$ , which are eigenfunctions of the non-perturbed Hamiltonian  $H_0$ , to which corresponds the eigenvalues,  $H_{11}$  and  $H_{22}$ , respectively. In this case, the Hamiltonian of the electronic diabatic wavefunctions is given by equation 2.12, where the diabatic potential curves,  $H_{11}$  and  $H_{22}$  are coupled by the adiabatic elements  $H_{12}$  and  $H_{21}$ .

$$H = \begin{bmatrix} H_{11} & H_{12} \\ H_{21} & H_{22} \end{bmatrix} \quad (2.12)$$

Considering that  $H_{12} = H_{21}$ , the coupling matrix  $H$  is diagnosable, and the adiabatic states can be defined as [63]:

$$E_{1,2} = \frac{1}{2}(H_{11} + H_{22}) \pm \frac{1}{2}\sqrt{(H_{11} - H_{22})^2 + 4H_{12}^2} \quad (2.13)$$

Where  $E_{1,2}$  are the adiabatic potential energies. From equation 2.13 we also conclude that if  $H_{22} - H_{11} \gg H_{12}$  a diabatic transition occurs, in a distance away from the crossing point  $R_c$ , as it can be seen in figure 2.1. However, when the two states are close to the crossing point ( $H_{11}(R_c) = H_{22}(R_c)$ ), the two states are quite different and only the crossing of diabatic states takes place. Furthermore, the possibility for the adiabatic states  $E_1$  and  $E_2$  to cross depends on the coupling  $H_{12}(R_c)$ , which must be equal to zero. This happens when the two wavefunctions that describe these adiabatic states show different symmetry and multiplicity [61,62].

A full analysis of the crossing between the curves represented in figure 2.1 allows to a better understanding of the electron transfer in atom-atom collisions and the consequent ion-pair formation process. One of the most used methods that leads with this type of processes is the formalism developed by Landau, Zener and Stuckelberg, known by Landau-Zener (LZ) method [63,92], which consists basically to find the inelastic transition probability at the crossing of two potential curves.

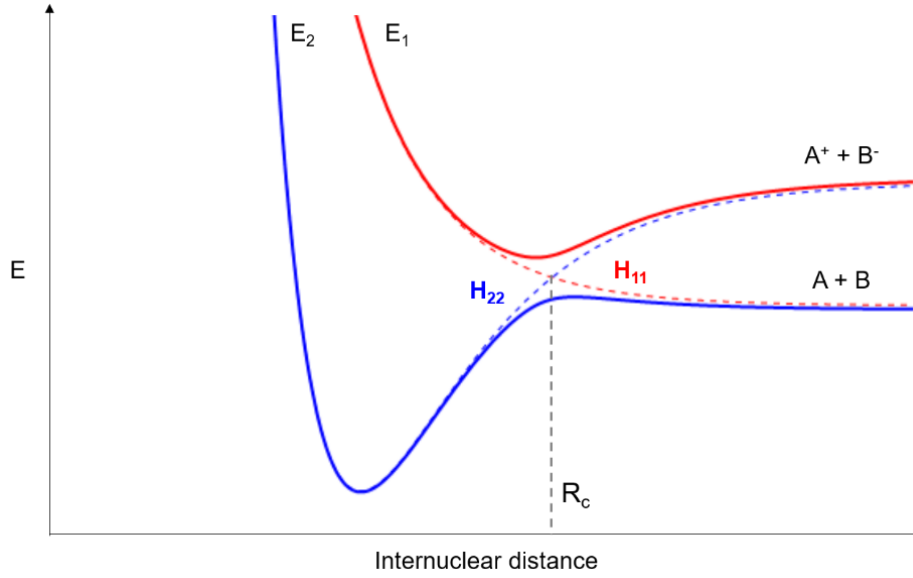


Figure 2.1. Schematics of adiabatic and diabatic potential energy curves for an atom-atom collision.  $E_1$  and  $E_2$  represent the adiabatic states (full curves). The dashed lines represent the diabatic states:  $H_{11}$  (covalent) and  $H_{22}$  (ionic).  $R_c$  is the crossing radius. Adapted from ref. [62].

The LZ method considers three main assumptions: the radial velocity ( $v_r$ ) is constant around  $R_c$ , the diabatic states are linearly dependent on  $R$  and  $H_{11}(R_c) = H_{22}(R_c)$ , as explained before. Thus, an expression to calculate the non-adiabatic transition probability can be obtained through equation 2.14. Briefly, it defines the probability of two-particle system staying in the diabatic potential energy curve ( $p$ ), which means the probability of passing  $R_c$  diabatically [63,65].

$$p = e^{-\left[ \frac{2H_{12}^2(R_c)}{\hbar v_r \left| \frac{d}{dR}(H_{11} - H_{22}) \right|_{R=R_c}} \right]} \quad (2.14)$$

For large distances from the crossing point, the energy difference between the ionic and the covalent configurations, i.e. the endoergicity of the system, corresponds to:

$$\Delta E = I - EA \quad (2.15)$$

Where  $I$  is the ionisation energy of the donor atom and  $EA$  the electron affinity of electron acceptor atom. From this we can obtain a value for the crossing radius ( $R_c$ ) in  $\text{\AA}$  from equation 2.16.

$$R_c = \frac{e^2}{\Delta E} = \frac{14.41}{\Delta E} \quad (2.16)$$

Let us now look at figure 2.2, where it is depicted an atom-atom scattering process taking into account the impact parameter  $b$  and two crossing points.

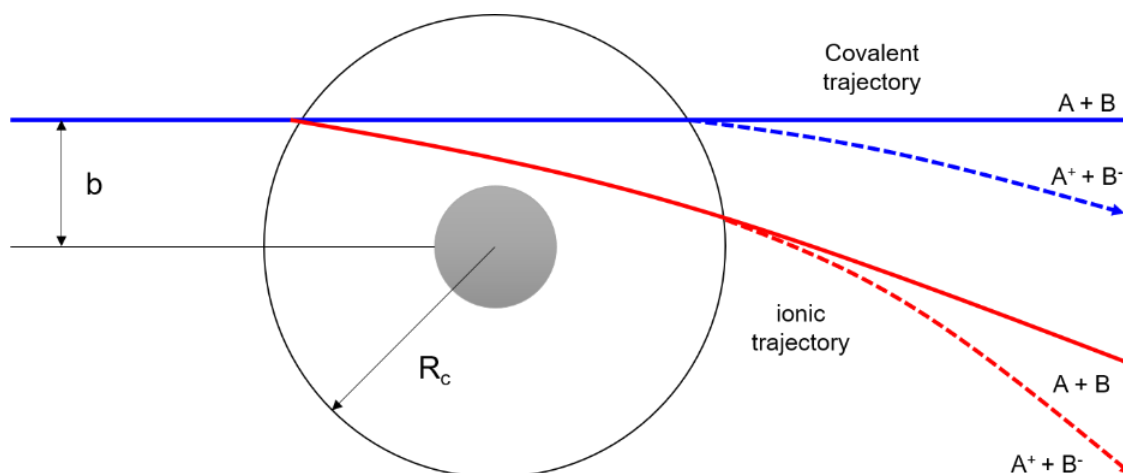


Figure 2.2. Schematics of atom-atom scattering representing the four possible pathways considering the impact parameter  $b$  and two different crossing radii. Adapted from ref. [62].

From figure 2.2 it is possible to discuss the electron transfer between two atoms through four different pathways for  $b < R_c$ . When the crossing occurs at the first crossing point ( $R = R_c$ ), the interaction between the two particles is mostly due to the coulombic interaction and it will cause a strong deviation in the trajectory of the cation formed after collision, meaning that an electron jump has occurred leading to ion-pair formation. This is designated as “ionic” trajectory. Re-neutralization can also occur, which means that the electron is transferred again to the cation. But, even in this case, a considerable strong path deviation is observed. After the first crossing and as the atoms come close together, they start to “repulse” each other and can reach the crossing point again (second crossing point). This case is designated as covalent trajectory, and the crossing can be passed diabatically (no electron transfer occurs) (maintaining as  $A + B$ ), or it can be passed adiabatically, resulting in ion-pair formation as well as in the ionic trajectory ( $A^+ + B^-$ ).

## 2.2 Atom–Molecule Collisions

In the previous section it was briefly discussed the simplest case about collisions between two atoms. However, in most of the current studies, particularly throughout the course of this thesis, the collisional system is much more complex, since we are dealing with polyatomic molecular systems. Therefore, in collisions between atoms (usually an alkali atom) and molecules many different new processes must be considered, namely electronic, vibrational and rotational excitations of the electron acceptor (molecule) and chemical reaction processes which lead to dissociation. This is due to the extra degrees of freedom of the molecular system. In this way, it is necessary to describe atom-molecule collisions based on multi-dimensional potential hypersurfaces to account for all the reaction

coordinates. Furthermore, in this type of collisions the rotational and vibrational periods of the molecule must be also considered, and so interesting aspects can be investigated depending on the collision energy used. The comprehensive description of these processes has been already done elsewhere [63,90,91] and here it will be presented just a brief discussion about the simplest one.

The analysis of the processes is facilitated by the fact that the electron transfer takes place at large separation from the atom to the molecule. In first approximation the rotational and vibrational periods are considered zero, which means the molecular target is “frozen” (the molecule is rigid during the collision). This assumption is valid if the atom-molecule potential is isotropic and the electronic properties of the molecule, especially its electron affinity, are independent of its internal degrees of freedom. This is true in the case that the vibrational time is much larger than the collision time (high velocity region:  $t_{\text{col}} \ll t_{\text{vib}}$ ) [63,65,90]. Here, bond stretching does not occur, and the electron transfer can be described following the Franck-Condon principle which can result in vibrational excitation of the TNI. Briefly, Franck-Condon principle means that, because of the short interaction time between the collision partners, the nuclear separation and the velocity of the relative nuclear motion will be the same after the interaction. The point on the potential energy curve of the molecule that represents the configuration before the transition lies directly below the point on the potential energy curve after the transition (vertical transition). This leads to a number of possible electronic transitions which depend on the relative shapes of the potential-energy curves available in a specific system [93]. For instance, ion-pair formation in alkali-atom-molecule collisions is a good way to determine molecular electron affinities. From the high velocity measurements, the vertical electron affinity can be obtained. On the other hand, it is important to note that in atom-molecule collisions usually the vibrational motion of the molecule is not frozen during the collision and additionally the molecular potentials are deformed with respect to those found in isolated conditions (low-velocity regions) [63]. For this type of collisions, the molecular anion is formed on the repulsive slope of the potential and has enough time to show an extension in its internuclear distance relative to a particular reaction coordinate. This is associated with a bond stretching during the collision, and it is a very important feature for ion-pair formation because the strong dependence of the coupling factor  $H_{12}$  and  $R_c$  with the electron affinity. Here  $H_{12}$  will be much smaller for the second crossing than for the first which favours the molecule to stay in the anionic state, leading to the formation of negative ions [62,65].

As been referred before, the electron transfer reactions are characterized by the “bound” electron being transferred from the electron donor to the molecular target which results in ion-pair formation. The available energy in atom molecule collision experiments is defined by the difference between the energy in the centre-of-mass frame and the ionisation energy of the electron donor, in equation 2.17 as follows:

$$E_{\text{av}} = E_{\text{CM}} - \text{IE} = \frac{m_{\text{m}}}{m_{\text{m}} + m_{\text{K}}} \cdot \alpha \cdot E_{\text{lab}} - \text{IE} \quad (2.17)$$

Where  $E_{av}$  is the available energy in eV,  $E_{CM}$  is the energy in the centre-of-mass frame,  $IE$  is the ionisation energy in eV, which in the case of present thesis is 4.34 eV (potassium atom),  $m_m$  is the mass of molecule,  $m_K$  is the mass of potassium atom and  $\alpha$  is an experimental correction factor (0.9) [94]. This later parameter was previously obtained using experimental studies and simulations, showing that the final kinetic energy of the hyperthermal potassium beam is smaller than the corresponding accelerating voltage. In this reaction, the velocity of the acceptor molecule is negligible (thermal) in respect to the velocity of the projectile. From 2.17, that anionic states with energies above  $E_{av}$  cannot be accessed. So, tuning the projectile energy (in this case potassium) it is possible to assess some and specific resonant states.

The presence of an electron donor in the collisional system represents an important and interesting feature of an electron transfer system. The cation that results from the electron donor ionisation acts as a “stabiliser” in the vicinity of the system (TNI) which leads to differences in the reactions pathways that are accessible when compared with free electron attachment processes. Indeed, this has been verified in some studies, namely using nitromethane as molecular target [66] in potassium-molecule collisions, where the formation of parent anion is observed even at higher collision energies. In DEA studies the channels that lead to formation of parent anion are not accessed [95].

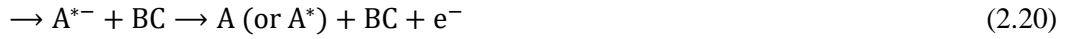
Moreover, in this thesis, some of these characteristics of electron transfer processes will be shown and discussed in collisions between potassium atoms and some molecules of interest (e.g. nitroimidazoles). The fragmentation pattern and the different reaction pathways resulting from this type of interaction will be highlighted in comparison with free electron capture studies whenever applicable. In fact, after electron transfer, the third-body system constitutes a chemical complex that interacts through a coulombic potential, which affects the transient molecular anion in different ways. Comparing with DEA where there is a strong competition with auto-detachment, in electron transfer processes the formation of anion is more favourable.

### 2.3 Ion–Molecule Collisions

Throughout the course of this thesis, electron transfer processes were also investigated through the study between ions and molecules. In particular, we used molecular oxygen anion ( $O_2^-$ ) as projectile and some simple molecular targets, such as  $N_2$ , water and pyridine. In previous sections it was already introduced the principal theoretical aspects which involve collisions between two particles. In this section it will be described briefly some specific aspects about ion-molecule collisions. The importance of positive and negative ions chemistry and physics is of interest in several fields, especially in astrophysics and in medical physics. The use of heavy ions in radiation therapy is a growing area of research. Moreover, the impact of radicals and ions produced after radiation interaction with matter (see Chapter 1) makes this type of processes an important research topic.



Similarly to the case of atom-molecule collisions, the description of ion-molecule collisions is also complex. Since in this thesis we will report experimental results from collisions between negative ions and molecules, let us focus on this type of reactions. When an anion interacts with a molecule several reactions can occur, as follows [96]:



Where  $A^-$  represents the anion projectile and  $AB$  the molecular target. These processes are: (2.18) direct detachment (DD), (2.19) to (2.21) detachment with excitation, (2.22) two-electron detachment, (2.23) charge transfer to temporary negative ion, (2.24) detachment with ionisation, and (2.25) dissociative ionisation. The later process involves the loss of an electron from the anion that is captured resonantly by the target, creating a short-lived TNI  $(BC)^{-\#}$ , which can be electronically and rovibrationally excited. In 2.23  $(BC^*)$  is the resultant neutral excited molecule. In some cases, the atom  $A$  can appear in excited state as well [97,98]. The negative ion electron detachment happens when the anionic incident beam passes through a low density neutral gas and collisions between the fast ions and the approximately stationary target atom or molecule remove one or more electrons from the negative ions [99]. Experimentally there are different methods to obtain the cross-section values for this type of collisions, namely the beam attenuation technique, which consists of measuring the loss of negative ions from the beam as it passes through the target.

Some studies regarding collisions between anions and molecules [97,98,100–104] have shown that for a low-energy range (up to 100 eV collision energy), direct detachment predominates (equation 2.18), while charge transfer to shape resonances (CTSR) are prevalent with energy. Moreover, DD also results in very low-energy loss ( $\leq 1\text{eV}$ ) by the projectile and CTSR is responsible for higher energy loss ( $\sim 3\text{--}4\text{ eV}$ ) [98]. Almeida *et al.* [98] investigated the fragmentation pattern in collisions using different negative ions as projectiles and have compared to alternative energy deposition mechanisms (electron impact ionisation, DEA and alkali-atom collisions), showing the appearance of different fragmentation channels. However, there is not much information available in the literature about experimental and theoretical research studies regarding anion-molecule

collisions in terms of dissociative reaction and subsequent fragmentation for low-energies. In collisions using  $\text{H}^-$  as projectile and  $\text{N}_2$  as target molecule, Risley [105] have also verified the influence of the shape resonance in the detachment processes. In this work a model is proposed to explain this influence based on formation and decay of a series of vibrational autodetaching states of  $\text{N}_2^-$ . Briefly, it was demonstrated that the shape resonance state  $^2\Pi_g$  of  $\text{N}_2^-$  is involved in the dynamics of detachment via charge transfer to the temporary negation ion. Identical results were also observed in  $\text{Cl}^- + \text{N}_2$  collisions [106,107]. Moreover, studies performed by Hasted *et al.* [108,109] and other authors [110–114] in collisions using different anionic beams, including  $\text{O}^-$  and  $\text{O}_2^-$ , have suggested that high cross-section values at lower energies could be due to the presence of stable excited states of long lifetimes of the negative ions, whose electron affinities are low. This is observed for example in  $\text{O}^- + \text{O}_2$ ,  $\text{O}_2^- + \text{O}_2$  and  $\text{O}^- + \text{Kr}$  interactions.

Other studies reported by Jalbert and co-workers [115–117] have explored the role of shape resonances in electron-detachment collisions between different negative ions and several atomic targets for intermediate and high-energies. They have demonstrated that for intermediate velocities this type of charge transfer processes are well reproduced by a model assuming an independent contribution from the outermost quasi-free electron and the neutral core atom of the negative ion.

Single ionisation and dissociative ionisation processes were also investigated in some studies performed at intermediate velocities, i.e. 1.0–2.14 a.u [118,119]. These results have shown that target ionisation is mostly due to projectile single electron loss and direct processes while target ionisation is a consequence of projectile double electron loss. Hence, two main features can be associated with this type of reaction: (1) single ionisation and single electron loss are associated with large impact parameters, (2) dissociative ionisation with consequent fragmentation and multiple electron loss are related with small impact parameters.

# CHAPTER 3

## EXPERIMENTAL SETUPS

The main focus of this chapter is the description and characterization of the two experimental apparatus used to perform the experiments throughout the course of this doctoral project. The first subchapter will be devoted to the setup where electron transfer collisions between neutral potassium atoms and different molecules of interest were performed and recorded through time-of-flight (TOF) mass spectrometry. This work was developed in the Atomic and Molecular Collisions Laboratory (LCAM), CEFITEC, Faculdade de Ciências e Tecnologia, Universidade NOVA de Lisboa under the supervision of Prof. Paulo Limão-Vieira. The second subchapter is related to the work performed in Laboratorio de Interaccion Radiación-Materia, CSIC, Madrid under supervision of Prof. Gustavo García. Here we will make a comprehensive description about all the main components of a novel crossed beam apparatus for collisions between negative oxygen ions and different neutral molecular targets. It is important to highlight that most of the system's elements were designed and assembled in the laboratory in order to suit the experimental purposes. Formation of positive and negative ions were detected through TOF mass spectrometry and cross-section values were obtained.

### 3.1 Potassium–Molecule Collision Crossed Beam Experimental Setup

#### 3.1.1 Overview

The crossed molecular beam apparatus is composed by two main chambers, the potassium chamber and the collision chamber differentially pumped and inter-connected by a gate valve. Both chambers are working under high vacuum conditions,  $1 \times 10^{-6}$  mbar ( $1 \times 10^{-4}$  Pa) and  $2 \times 10^{-7}$  mbar ( $2 \times 10^{-5}$  Pa), respectively. The general schematics is shown in figure 3.1.

Briefly, in the potassium chamber a neutral hyperthermal potassium beam is produced through a resonant charge exchange between the accelerated cationic potassium beam ( $K^+$ ) and the thermal potassium beam ( $K^0$ ). The neutral potassium beam is produced in an energy range between 8 and 1000 eV.

The second chamber comprises the Langmuir-Taylor detector, the molecular target oven, the collision region and the TOF mass spectrometer. In this chamber, negative ions resulting from the collision between the neutral potassium beam and gas-phase molecular target are detected through TOF mass spectrometry. Throughout the course of this work two different TOF mass spectrometers were used to perform the experiments, a dual-stage linear TOF (figure 3.1) and a reflectron TOF (figure 3.2). The experimental setup is also equipped with a hemispherical analyser to follow the resultant post-collisional potassium cation through energy loss measurements. The next sections will introduce and discuss all of these components in more detail.

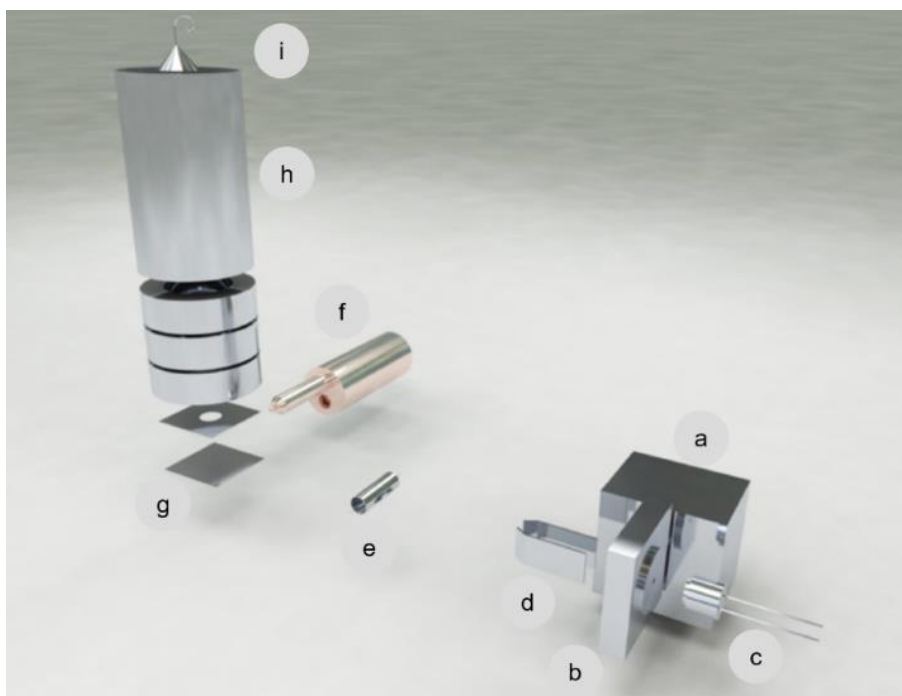


Figure 3.1. Schematics of the linear TOF experimental apparatus: a) potassium oven; b) charge-exchange chamber; c) cationic potassium source; d) deflecting plates; e) Langmuir-Taylor detector; f) molecular target oven; g) collision/extraction region; h) TOF mass spectrometer; and i) channeltron detector. Adapted from ref. [62].

### 3.1.2 Neutral Potassium Beam

The hyperthermal neutral potassium beam is produced as schematically shown in figure 3.3. Initially, a hyperthermal cationic potassium beam ( $K^+_{\text{hyp}}$ ) is formed produced by a commercial  $K^+$  ion source (Heatwave Labs, model 1011139) and accelerated with kinetic energies between 8 and 1000 eV towards the entrance of a charge exchange chamber (CEC) through a  $\sim 1.5$  mm circular aperture. At the same time, in the K oven a solid potassium chunk is heated to a temperature around 120° C

( $\sim 393$  K) and a vaporized thermal neutral potassium beam ( $K_{th}^0$ ) is produced and diffused to the CEC. The CEC is kept at a temperature of about  $140$  °C ( $\sim 413$  K) to avoid condensation in the connection between the oven and chamber. The temperature of both K oven and CEC is maintained by making use of two cartridge heaters and controlled by two PT100 resistors. For more detailed technical information see ref. [62].

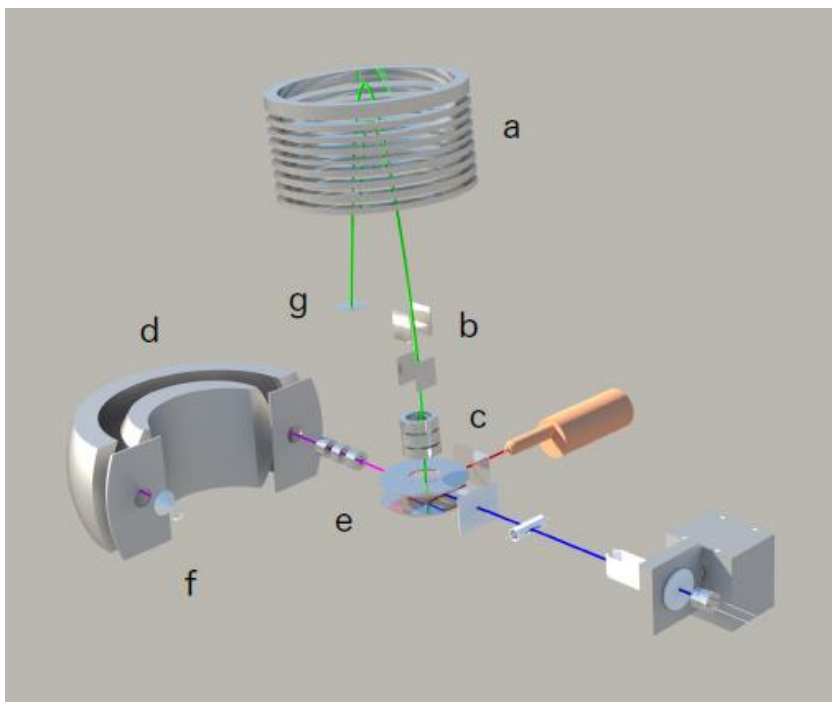


Figure 3.2. Schematics of the new reflectron TOF apparatus and the hemispherical analyser: a) stack of laser cut electrodes (reflectron); b) deflecting plates; c) lens elements; d) hemispherical analyser; e) Einzel lens at the entrance of analyser; f) channeltron detector; and g) microchannel plate (MCP) detector. Taken from ref. [120].

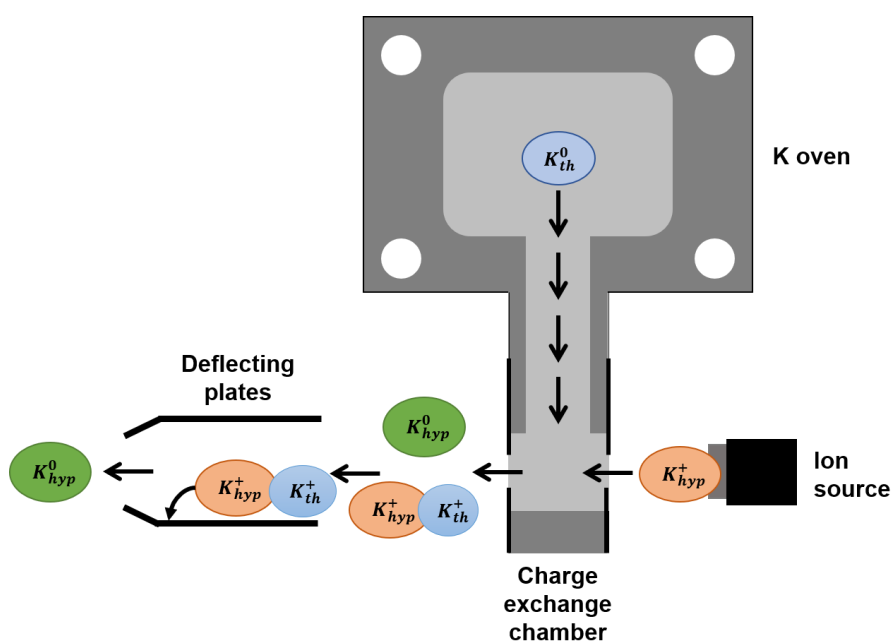


Figure 3.3. Schematics of the charge exchange hyperthermal neutral potassium beam formation.

Within the CEC, the potassium beam comprises  $K_{th}^0$  and  $K_{hyp}^+$  and a hyperthermal neutral potassium beam ( $K_{hyp}^0$ ) is created through a resonant charge exchange process between them, as represented in equation 3.1. This process is resonant since no kinetic energy of the hyperthermal projectile is lost.



Then, at the exit of the CEC after a  $\sim 1.5$  mm circular aperture, a set of deflecting plates are assembled to deflect the  $K_{hyp}^+$  that do not charge exchange, are extracted through an electric field applied between the two plates. One of the plates is at a positive voltage while the other is connected to an electrometer which measures a relative current of the  $K_{hyp}^+$ . This relative value of current is mainly to monitor the performance of the potassium ion source and the efficiency of the charge exchange process. Previous experimental tests were made in order to find the best potential to maximize the  $K_{hyp}^+$  deflection for each ion beam energy (see ref. [62]). The comprehensive work of Aten and Los [94] reports that some space charge effects in the system may be present. Because of that an experimental parameter  $\alpha$  is considered in equation 2.17, Chapter 2.

### 3.1.3 Langmuir-Taylor detector

Once the hyperthermal neutral potassium beam is produced in the CEC, it travels to the second chamber passing through a surface detector placed just after the gate valve (see figures 3.1 and 3.2). The Langmuir-Taylor detector is used to monitor the neutral potassium beam and it is essentially composed of a stainless steel cylindrical collector placed around a central high purity (>99 %) iridium filament (figure 3.4). The fast neutral potassium atoms pass through the two wide holes placed on opposing sides of the collector and a small fraction of the beam is ionised on the heated surface of the iridium filament, kept at a current of 0.63 A and a voltage drop of +60 V applied to repel the ionised potassium into the collector which is connected to an electrometer to measure the current of the resultant cations produced after ionisation. The current value measured in the electrometer is used later to normalise the ions yield produced after the collision between neutral potassium atoms and the molecular target.

### 3.1.4 Molecular Target Oven

The molecular target oven is constituted by three main components: a stainless steel outer body, a stainless steel container and a stainless steel capillary tip with 1.5 mm diameter. It is placed at right angles from the direction of the potassium beam. The solid molecular samples inserted inside the container and heated are sublimated using a halogen bulb (R7s/200Watts) and a cylindrical stainless steel reflector to increase the heating efficiency. The bulb's intensity is controlled by an adjustable Variac and the temperature is measured by a K-type thermocouple. The heating temperature is

changed accordingly to the sample under study. It is also possible to adjust the oven's position since it is placed on a movable holder that can move in the XY plane.

The liquid and gas molecular samples are introduced in containers placed outside the collision chamber and are introduced inside the chamber through a *Swagelock* entrance in the outer body of the oven, passing by a sapphire valve that allows to control the samples' pressure. The sample introduction system is independently pumped by a rotatory pump. In order to guarantee that the liquid samples introduced into the system are purified, heat and thaw-pump cycles are performed prior to their admission into the vacuum system.

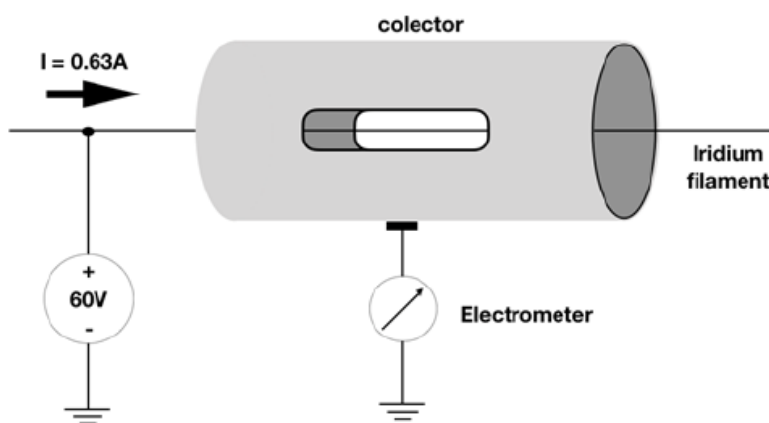


Figure 3.4. Langmuir-Taylor detector. Taken from ref. [120].

### 3.1.5 Time-of-Flight Mass Spectrometer

#### 3.1.5.1. TOF spectrometry introduction

The essential principle of time-of-flight (TOF) mass spectrometry is based on that ions with different mass-to-charge ratios ( $m/z$ ) and subject to the same electric field are accelerated with different velocities reaching a detector at different time, along a field-free region of known length, in which time is inversely proportional to the square root of  $m/z$  (see equation 3.3).

When the charged particles are formed in the extraction region, they are subject to an electric field created between two plates. The potential energy ( $U$ ) of these particles is given by the product of the charge of the particle ( $z$ ) and the electric field ( $V$ ),  $U = zV$ . The charged particles are then accelerated due to the potential  $V$  applied in one of the plates and the potential energy is converted into kinetic energy ( $E_k$ ),  $E_k = \frac{1}{2}mv^2$ , which means that:

$$U = E_k \Leftrightarrow zV = \frac{1}{2}mv^2 \quad (3.2)$$

Where  $m$  is the mass of the ion and  $v$  its velocity. Once flying the ions' velocity does not change during the path towards the detector. Since  $v = \frac{d}{t}$ , we can rearrange equation 3.2 as follows:

$$t = \frac{d}{\sqrt{2V}} \sqrt{\frac{m}{z}} \Leftrightarrow t = c \sqrt{\frac{m}{z}} \quad (3.3)$$

The simplest version of a TOF mass spectrometer is made by an extraction region, where the ions are repelled in direction to a detector passing through a drift field-free region. However, many optimisations and improvements were made, especially in terms of mass resolution, as for example by introducing a reflectron type TOF spectrometer. The TOF spectrometers have some advantages compared to other mass spectrometry apparatus, especially because they can measure an unlimited  $m/z$  range spectrum in a very short time (tens of microseconds) and its transmission and sensitivity are usually higher [62].

In mass spectrometry it is conventional to measure the resolving power by the ratio of  $\frac{m}{\Delta m}$  where  $\Delta m$  is difference in mass between two distinguishable mass peaks in a mass spectrum. In TOF it is convenient to work in the time domain. Thus the resolving power can be measured as in equation 3.4. The infinite time interval,  $\Delta t$ , is usually the full-width at half-maximum (height) of the peak (FWHM).

$$\frac{m}{\Delta m} = \frac{t}{2\Delta t} \quad (3.4)$$

The experimental results of this thesis regarding potassium-molecule collisions were obtained in a custom-made dual-stage linear TOF spectrometer based on Wiley-McLaren geometry [121] and a Reflectron TOF mass spectrometer (Kore Technology ©).

### 3.1.5.2. Dual-Stage linear TOF

The dual-stage linear TOF spectrometer implemented in LCAM laboratory is constituted by a collision/extraction region, an acceleration region, a set of Einzel lens, deflecting plates, a field-free region and a channeltron detector, as schematically represented in figure 3.5. In figure 3.6 we show a schematics of the electrical connections for the extraction system.



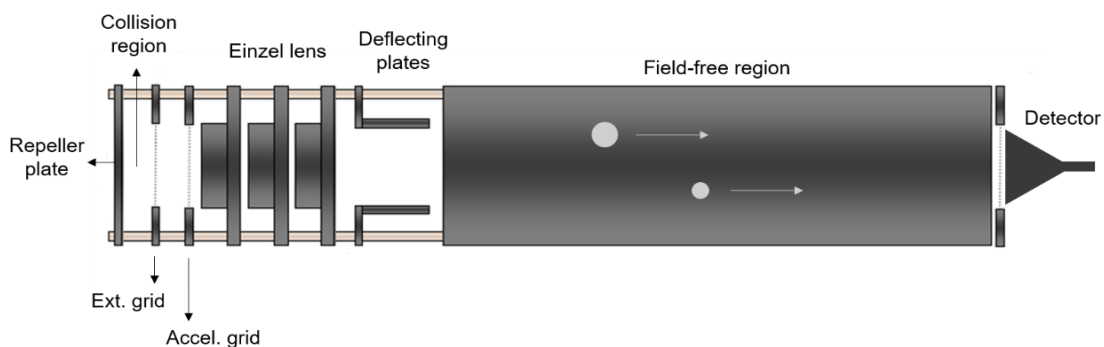


Figure 3.5. Schematics of the implemented linear TOF mass spectrometer.

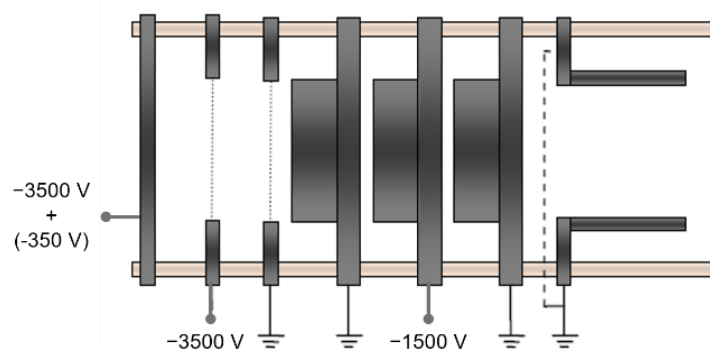


Figure 3.6. Electrical connections of the TOF extraction system.

The collision between the neutral potassium atoms and the molecules of interest occurs in the extraction region placed between two electrodes separated by 12 mm. The top one has a 10 mm diameter grid (extraction grid). In this region the negative ions produced during the collision are extracted towards the acceleration region by a fast rise time pulsed voltage signal of -350 V applied in the repeller plate. The pulse is applied through a Jordan D-1040 Pulser. The pulse duration is typically one microsecond but can vary according to the fragments' mass being analysed (typically 1-2  $\mu$ s). When no pulse is applied both repeller plate and extraction grid are at -3500 V constant voltage.

The acceleration region is also a region between two electrodes separated by 12 mm, the extraction grid and the acceleration grid (grounded). Here the anions are accelerated towards the next regions due to the -3500 V constantly applied to the extraction grid. When no pulse is applied no extraction occurs. Before reaching the detector, the anionic species pass through a set of Einzel lens and deflecting plates allowing focusing and improving the transmittance. The Einzel lens system is composed by three electrodes, two grounded and one (in the middle) at -1500 V. After leaving the lens system, ions enter the deflecting plates that are kept at a ground potential (0 V), since no significant improvement in the detection efficiency has been noticed [62]. After that, ions enter the drift tube also known as field-free region of about 1 m length and are detected in a channeltron type detector, operating in pulse counting mode. As a result, for each ion impinging on the detector, the

channeltron generates a negative voltage pulse with 20 ns duration and an amplitude of typically 20 mV. This signal is amplified through the ORTEC VT-120 pre-amplifier and enters the FastComtec P7888 multiscale. A full detailed description of the dual-stage TOF arrangement can be found elsewhere [62].

### 3.1.5.3. Dual-stage Reflectron TOF

As referred before, part of the experiments of this doctoral project were performed using a commercial Reflectron type TOF spectrometer (R-500-6) by Kore Technology ©. The main difference between this type of device and the former one is basically the ion energy focusing mechanism (ion mirror). Briefly, the apparatus comprises two extraction plates, the field-free region, the ion mirror and the microchannel plate detector, as represented in figure 3.7.

The extraction region comprises two circular parallel electrodes separated by a distance of 10 mm. In this region the neutral potassium beam and the molecular target cross at right angles and the ionic species formed are extracted and accelerated into the transfer lens by a 400 V/cm electrostatic pulse. After the lens systems (two sets of lenses), the ions travel through two sets of deflecting plates which allow the adjustment of ions trajectory in the XY plane passing through a 1 mm diameter aperture for differential pumping. Deflection plates immediately after the transfer lens provide the means to point the ions at the detector.

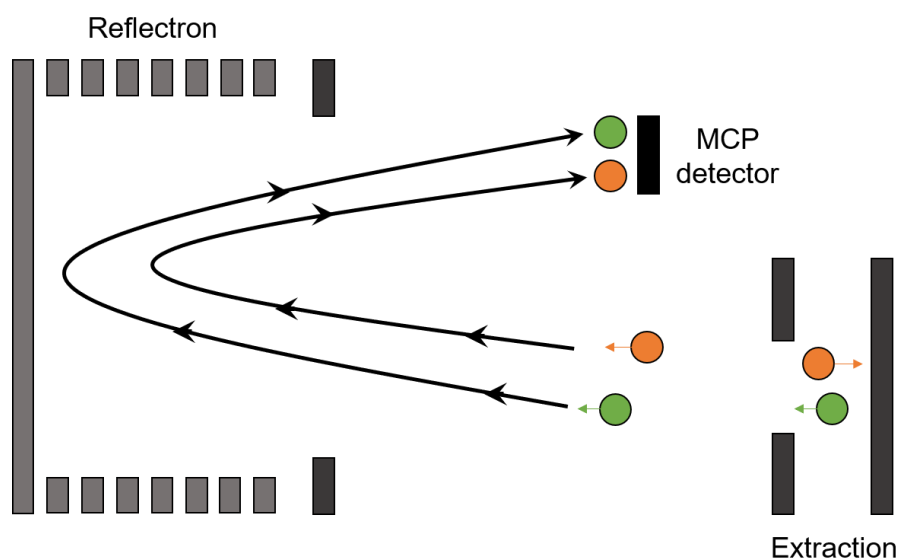


Figure 3.7. Schematic representation of the basic principle of a Reflectron TOF mass spectrometer showing two ions with the same  $m/z$  produced in the extraction region with different velocity distributions.

Then, the ions pass through a field-free region, where they must traverse without experiencing any further acceleration or deceleration and reach the ion mirror (reflectron). This region consists of a series of annular electrostatic lenses placed at the opposite end of the drift tube (figure 3.7). Here,

a constant electrostatic field is created to reflect the ion beam towards the detector. The reflectron is used to compensate for the initial kinetic energy distribution of the ions in the direction of the ion extraction. The more energetic ions penetrate deeper into the reflectron, thus taking a slightly longer path to the detector. The less energetic ions (of the same  $m/z$ ) penetrate a shorter distance into the reflectron and hence take a shorter path to the detector than their more energetic counterparts. After that, the ions reach the 25 mm diameter dual microchannel-plate (MCP) detector. The arrival times of the ions are recorded with up to 0.25 ns resolution.

### 3.1.6 Hemispherical Energy Analyser (HEA)

The energy analyser recently implemented consists of two concentric hemispheres with a potential difference acting as a narrow energy filter for charged particles, which in the present arrangement allows to analyse the  $K^+$  ions formed after collision. Let us consider a  $K^+$  ion passing through the centre of the hemispheric electrodes. The ion kinetic energy ( $E_0/z$ ), is given by equation 3.5.

$$V_p = \frac{E_0}{z} \left( \frac{R_2}{R_1} - \frac{R_1}{R_2} \right) \quad (3.5)$$

Where  $V_p$  is the voltage difference between the two hemispheres,  $R_1$  and  $R_2$  are the internal and external radius. According to the previous equation the transmitted energy ( $E_0/z$ ) is proportional to the potential  $V_p$ . An advantage of this energy analyser system is its large electrode gap which increases the resolution and transmission.

The analyser entrance slit is positioned aligned with the beam's optical path. Both entrance and exit slits are adjustable in width, varying from 1 to 3 mm. A set of Einzel lens is placed at the analyser's entrance in order to focus the  $K^+$  ions into the analyser without influencing its energy. With the current configuration and for a potassium collision energy of 100 eV in the lab frame, the energy resolution,  $\Delta E \approx 0.5$  eV at FWHM. This analyser can work in two energy scan modes: constant transmission (CT) and sector field sweep (SFS). For more details check elsewhere [120].

### 3.1.7 Vacuum system

The vacuum conditions are achieved by making use of two diffusion pumps with 1300 l/s and 1550 l/s pumping speed for the potassium and collision chamber, respectively. Both chambers are separated by a manual gate valve which guarantees a differential pumping, with an ultimate pressure of  $1 \times 10^{-6}$  mbar ( $1 \times 10^{-4}$  Pa) in the potassium chamber and  $2 \times 10^{-7}$  mbar ( $2 \times 10^{-5}$  Pa) in the collision chamber. A nitrogen trap is coupled to each pump to avoid oil migration into the chambers and undesired residues into the diffusion pump. The primary vacuum is guaranteed by a two-stage rotary pump with a pumping speed of 6 l/s that ensures an ultimate pressure around  $3 \times 10^{-2}$  mbar (3 Pa). A molecular sieve trap is placed to avoid contamination with rotary oil vapours. The sample's inlet

system for liquid and gas samples is pumped by a two-stage rotary pump. Both TOF spectrometers are differentially pumped by a Pfeiffer 600 l/s Turbo molecular pump achieving an ultimate pressure of  $1 \times 10^{-8}$  mbar ( $1 \times 10^{-6}$  Pa). Figures 3.8 and 3.9 depict the schematics of the vacuum system and the reflectron TOF spectrometer.

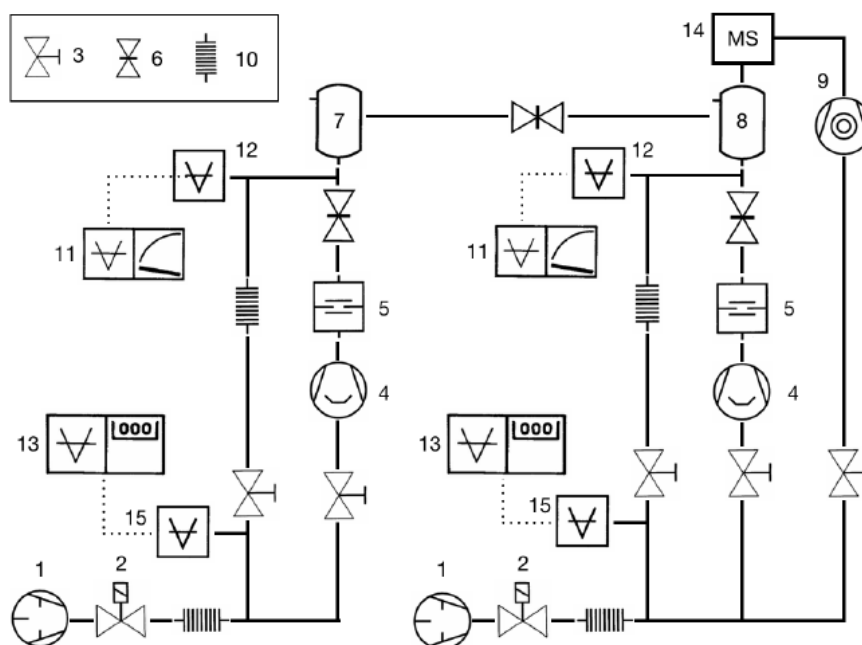


Figure 3.8. Vacuum system schematics: 1) Rotary pump; 2) Electro-magnetic valve; 3) Membrane valve; 4) Diffusion pump; 5) Baffle; 6) Gate valve; 7) Potassium chamber; 8) Collision chamber; 9) Turbomolecular pump; 10) Flexible tube; 11) Vacuum gauge control unit with dial indicator; 12) Penning gauge; 13) Vacuum gauge control unit with digital indicator; 14) TOF mass spectrometer; 15) Pirani gauge. Taken from ref. [120].

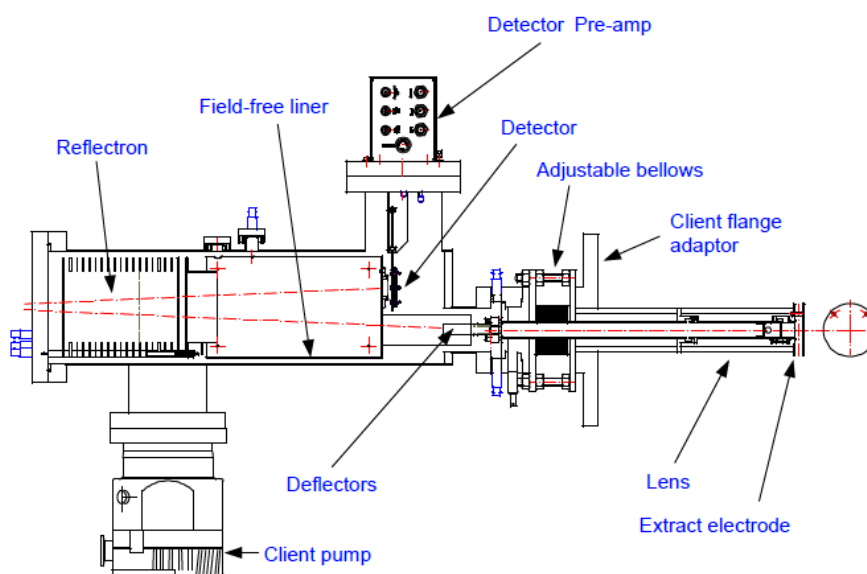


Figure 3.9. Reflectron TOF instrument overview recently installed from Kore Technology, UK. Image courtesy of © Kore Technology, Ltd.

## 3.2 O<sub>2</sub><sup>-</sup> – Molecule Collision Crossed Beam Experimental Setup

### 3.2.1 Overview

The second part of the experimental study performed throughout the course of this doctoral project is connected with collisions between oxygen negative ions and different gas-phase molecular targets. For that, a novel experimental system has been developed at CSIC, Madrid to analyse the interactions of negative radical species with biological relevant molecular targets.

The experimental setup comprises three interconnected high-vacuum chambers (projectile, collision and transmission collision chambers, respectively). They are differentially pumped and separated by a 2 mm diameter collimators which allow ultimate base pressures of  $4.6 \times 10^{-7}$  mbar ( $4.6 \times 10^{-5}$  Pa) for the projectile chamber and  $3.2 \times 10^{-8}$  mbar ( $3.2 \times 10^{-6}$  Pa) for the collision and transmission chambers. A schematic diagram is shown in figure 3.10.

The projectile chamber comprises a pulsed gas valve, a cathode and two anodes, and a set of Einzel lens. In this chamber, the anionic oxygen primary beam is produced through a pulsed hollow cathode discharge induced-plasma for applied cathode voltages between 500 and 600 V.

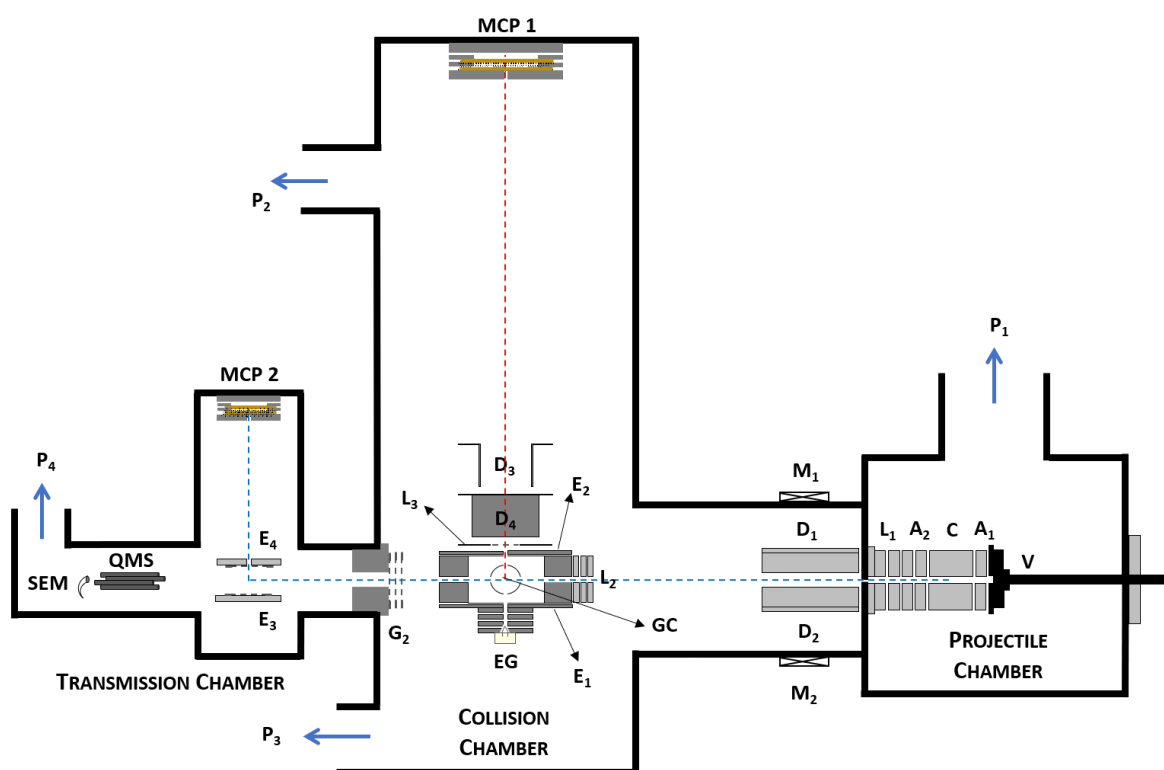


Figure 3.10. Schematics of the experimental setup with: V, pulsed supersonic valve; C, hollow cathode discharge; A<sub>1</sub> and A<sub>2</sub>, anodes; L<sub>1</sub>, L<sub>2</sub> and L<sub>3</sub>, Einzel lenses; D<sub>1</sub>, D<sub>2</sub>, D<sub>3</sub> and D<sub>4</sub>, deflecting plates; M<sub>1</sub> and M<sub>2</sub>, magnets; E<sub>1</sub>, E<sub>2</sub>, E<sub>3</sub> and E<sub>4</sub>, extraction plates; G<sub>2</sub>, focusing/attenuation grids; EG, electron gun; GC, gas cell; MCP 1 and MCP 2, multichannel plate detectors; QMS, quadrupole mass spectrometer; SEM, secondary electron multiplier detector; P<sub>1</sub>, P<sub>2</sub>, P<sub>3</sub> and P<sub>4</sub>, turbomolecular pumps.

The collision chamber is composed by a set of deflecting plates, an electron gun, a gas-cell where molecular samples maintained at a constant pressure, and the extraction region formed by two extractive parallel plates and a deflection plate system to direct the ionic species formed after the interaction through a drift tube constituting the first time of flight (TOF) spectrometer. Finally, the transmitted beam enters the transmission chamber where negative charges are deflected and directed to a second TOF spectrometer. A quadrupole mass spectrometer (QMS) is also placed in the anionic beam optical path direction to detect neutral fragments which may be produced during the interaction between the anionic projectile beam and the gas-phase molecules.

In the next sections a more detailed description of the main apparatus' components as well as some optimisation tests will be presented.

### 3.2.2 Anionic projectile beam

The negative oxygen ions ( $O_2^-/O^-$ ) that constitute the projectile beam are produced following the mechanism of a pulsed hollow cathode discharge induced-plasma. An electric potential difference ( $\sim 500$  V) is created between the hollow cathode and anode as shown in figure 3.11. Then utilising a commercial Parker pulsed valve (VAC1250) the precursor gas projectile ( $O_2$ ) was admitted through a supersonic expansion into the chamber. The valve is operated during  $350 \mu s$  width a 0.44 % duty-cycle under a gas pressure of  $4.0 \times 10^{-5}$  mbar. Oxygen negative ions are produced by the hollow cathode effect (HCE), which is basically an electrical phenomenon described by an exceptionally high discharge current produced inside the cathode accompanied by a high plasma density, light emission, cathode sputtering and chemical changes in the gas [122]. One of the main characteristics of this type of discharge is the electrostatic trapping of fast electrons in an oscillating motion inside the cathode, known as pendulum effect [123]. The HCE occurs in different stages [124]. Firstly, the electrons obtain enough energy from the electric field for electronic excitation. Then, inside the cathode the fast electrons are continually being repelled by the inner walls' potential and are accelerated leading mostly to ionisations in the gas, producing positive ions. Ionising processes produce a cascade of slow secondary electrons which results in intense excitation and recombination of ions and electrons. Since in this case is a pulsed mechanism, during a brief period of time in the afterglow, the secondary electrons lose almost all their energy and electron attachment and charge transfer processes can occur producing negative ions [125]. Equations 3.6, 3.7 and 3.8 indicate possible processes for the production of  $O^-$  and  $O_2^-$  (electron attachment and charge transfer).



The primary beam (O<sub>2</sub><sup>-</sup>/O<sup>-</sup>) is then focused towards the collision chamber through a set of three element Einzel lens (L<sub>1</sub>) placed just after the anode (figure 3.11). At the entrance of the second chamber XY deflecting plates are placed (figure 3.10) to control the direction of the beam across the collision chamber. Attached to these plates two magnets are positioned to avoid stray electrons passing to the collision region.

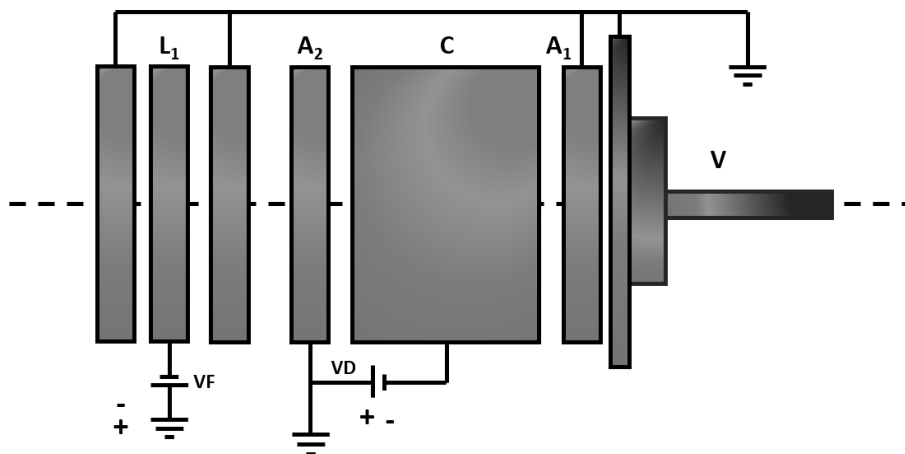


Figure 3.11. Electrical schematics of the anion beam source. V, pulsed supersonic valve; A<sub>1</sub> and A<sub>2</sub>, anodes; C, hollow cathode discharge; L<sub>1</sub>, Einzel lens; VD, discharge voltage; VF, focusing voltage.

### 3.2.3 TOF mass spectrometers

#### 3.2.3.1. Post-collisional negative and positive ions detection

As mentioned before, there are two different extraction regions with their respective TOF mass spectrometers in the collision and transmission chambers, respectively. The first TOF mass spectrometer is used to detect the ionic species (positive and negative) formed in the collision between the anionic projectile beam and the gas-phase molecules. Briefly, the O<sub>2</sub><sup>-</sup>/O<sup>-</sup> beam enters the scattering chamber (SC) through a small hole with 2 mm diameter after being focused by a set of Einzel lens (L<sub>2</sub>) placed just at the entrance of the SC, where it crosses orthogonally the gas-cell (GC) containing the molecular target (figure 3.10). The molecules in study are admitted into the GC through a sapphire leak valve and the pressure is monitored at two different points along the SC by means of a calibrated MKS-micro-Pirani gauge and an absolute capacitance MKS Baratron (627B) manometer, respectively.

The GC is basically a small cylindrical chamber with 36 mm in diameter and 27 mm in height (figure 3.12 (b)), where a negative or positive voltage is applied to accelerate or decelerate the anionic projectile beam so defining the kinetic energy of the O<sub>2</sub><sup>-</sup>/O<sup>-</sup> anions, and therefore the collision energy (in the lab frame). Throughout the course of the present PhD studies some modifications to the scattering chamber were implemented in order to optimize the interaction process and to allow measuring absolute total cross-section values. In figure 3.12 we show the commercial collision

system initially implemented (a) and the adjustments made, namely the addition of a gas-cell (b). Due to the projectile-target interactions, positive and negative anionic fragments of the target molecule can be formed via ionisation and electron transfer processes. These anionic species are extracted and accelerated by a pulsed voltage drop (varying between 0 and  $\pm 950$  V) applied between the extraction plates (E1 and E2) along the GC. The extractive pulse has a time duration of  $\sim 2$   $\mu$ s and pushes the resulting ions into a 1.4 m TOF mass spectrometer, where anions are mass analysed and detected by a microchannel plate (MCP1) under single pulse mode operation. Additionally, beneath the gas-cell a homemade electron gun is placed to provide an energy controlled electron beam (0-500 eV incident kinetic energy) crossing the GC perpendicularly to the anion beam direction and opposite to the TOF mass analyser. This electron beam is used to test the system's operation in order to guarantee the proper working conditions. (a)

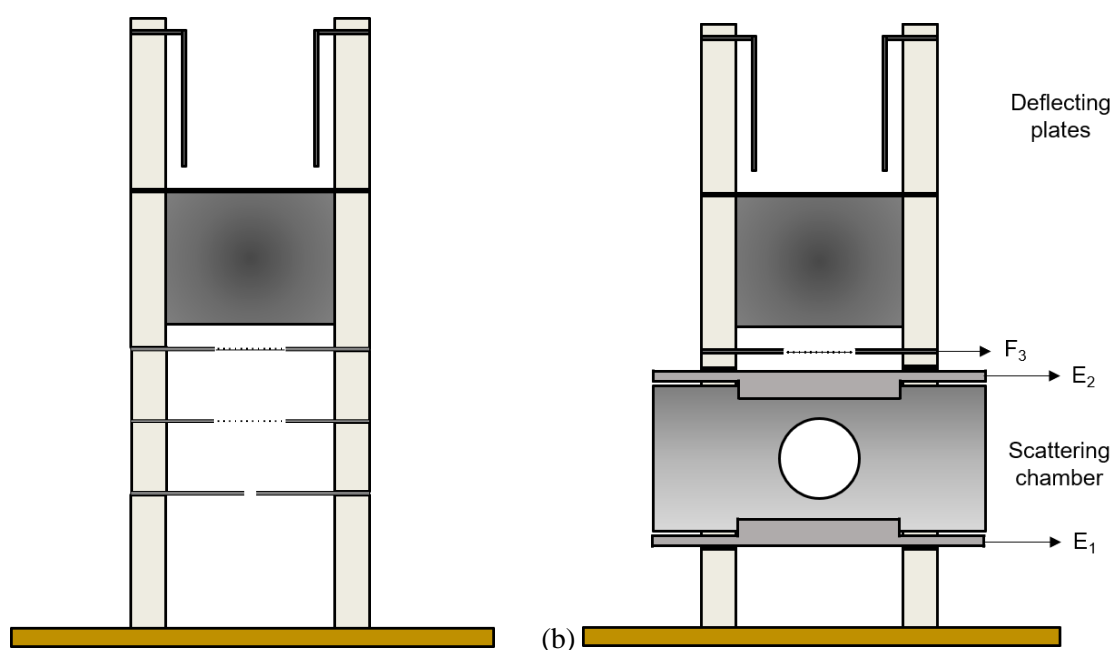


Figure 3.12. Schematics of the implemented TOF spectrometer with: a) the first commercial extraction system implemented into the chamber; b) the modified extraction system with a homemade cylindrical scattering chamber. E<sub>1</sub> and E<sub>2</sub> are the extraction plates and F<sub>3</sub> is an acceleration grid.

### 3.2.3.2. Post-collisional primary beam detection

The second TOF mass spectrometer in the transmission chamber is used to record and analyse the O<sub>2</sub><sup>-</sup>/O<sup>-</sup> incident beam before and after the interaction with the molecular target. This system comprises a set of attenuation/focusing grids (G<sub>2</sub>), an extraction region with two extraction plates (E<sub>3</sub> and E<sub>4</sub>) (see figure 3.13) and a TOF spectrometer.

If no extraction is applied to the collision region (gas cell), the anionic projectile beam reaches the second extraction region where it is repelled by a negative voltage applied to E<sub>3</sub> towards the second TOF mass spectrometer. The signal intensity of this beam is recorded by a microchannel plate



(MCP2) placed 10 cm above the initial beam direction at a total distance of 0.47 m from the hollow cathode source (figure 3.10).

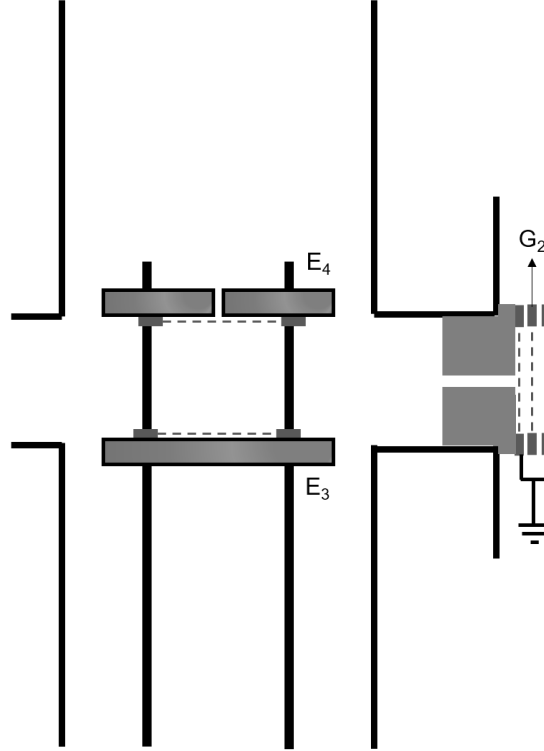


Figure 3.13. Schematics of the second extraction system implemented to detect and analyse the anionic primary beam.

At the entrance of this second extraction region, the anionic incident beam passes through a set of three grids ( $G_2$ ), the two externals are grounded and the central one is biased from 0 to -500 V. The main role of these grids is to determine the primary beam energy distribution and therefore, the energy resolution of the total cross-section measurements. In figure 3.14 a typical TOF mass spectrum of the projectile anionic beam is shown. The two local maxima are assigned to  $O^-$  and  $O_2^-$ , respectively.

### 3.2.4 Data acquisition methodology

#### 3.2.4.1. Total electron detachment cross-sections

The electron detachment cross-sections ( $\sigma_{exp}$ ) were determined by using the beam attenuation technique which is based on the well-known Beer-Lambert law (equation 3.9).

$$I = I_0 e^{-\frac{Pl\sigma_{exp}}{kT}} \quad (3.9)$$

Where  $I_0$  is the initial anion beam intensity,  $I$  is the transmitted anion signal through the gas cell,  $P$  is the gas pressure,  $l$  is the effective path length of the GC (36 mm),  $k$  is the Boltzmann constant and  $T$  is the temperature.  $T$  is derived from  $T = \sqrt{T_c T_m}$  where  $T_c$  and  $T_m$  are the temperature of the scattering chamber, as measured with a thermocouple device, and the operation temperature of the Baratron gauge, respectively. By assuming an ideal gas behaviour, equation 3.9 can be written as:

$$\ln\left(\frac{I}{I_0}\right) = -\frac{l\sigma_{exp}}{kT}P \quad (3.10)$$

According to the above procedure, a semi-logarithmic plot of  $\frac{I}{I_0}$  as a function of  $P$  provides the slope (m) which is related to  $\sigma_{exp}$  as:

$$\sigma_{exp} = \frac{mkT}{l} \quad (3.11)$$

Briefly, these measurements are performed by recording the TOF spectra of the transmitted anionic beam intensity as a function of the gas pressure. The  $\frac{I}{I_0}$  value is directly measured from the area of the  $O_2^-$  peak while it is reduced up to half of its initial value. This procedure ensures that only single scattering processes are taking place along the gas cell. The pressure range is then rearranged for each incident energy in order to ensure that multiple scattering effects are negligible. This is accomplished by checking that the attenuation of the transmitted beam intensity in this pressure range follows a single exponential decay. The pressure range varied from 0 to 6 mTorr depending the molecular sample under investigation. A LabView based acquisition and analysis data programme has especially been designed for this experiment. This software has also been programmed to display the attenuation of the beam and to calculate the slope of the corresponding semi-logarithmic plots (equation 3.11) giving directly the experimental cross-section values ( $\sigma_{exp}$ ).

As mentioned above, pressure gradients in the GC were determined by measuring the gas pressure at both sides of the cell with two different pressure gauges (a calibrated MKS-micro-Pirani gauge and an absolute capacitance MKS Baratron (627B) manometer). By assuming that the right gas pressure along the beam path is the average between both measurements, a correction factor of 1.15 has been applied to the MKS Baratron values. At least five attenuation measurements have been performed for each considered energy in order to obtain statistical uncertainties within 5%.

To improve the accuracy of the cross-section measurements a retarding voltage is applied to the grid system ( $G_2$ ) placed just before the extraction of the  $O_2^-/O^-$  signal. This allowed to find the best operational point, in terms of energy resolution, just before initiating the measurements for each molecular target under study.

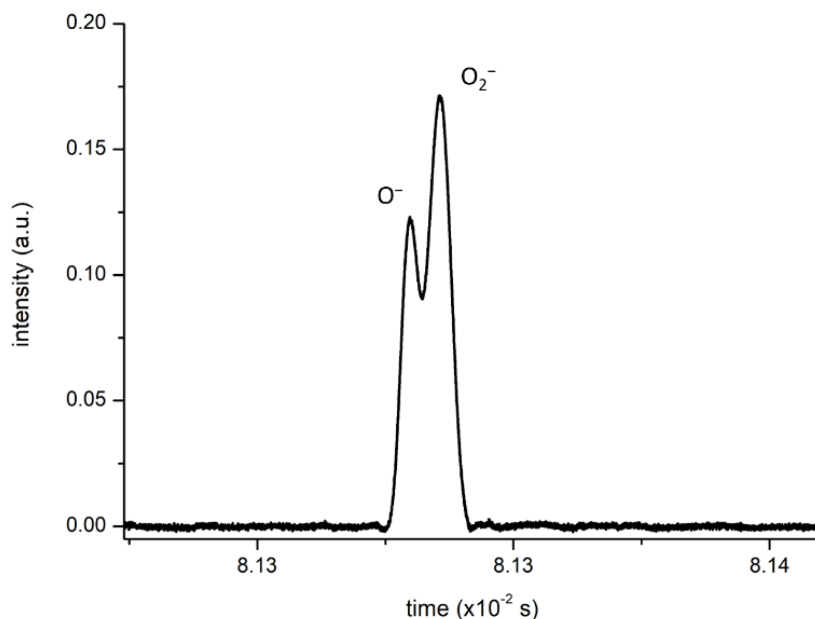


Figure 3.14. Typical Time-of-flight mass spectrum of the projectile beam (O<sub>2</sub><sup>-</sup>/O<sup>-</sup>) at 200 eV in laboratory frame.

#### 3.2.4.2. Positive and negative ions detection

As mentioned in Section 3.2.3.1, positive and/or negative ions are formed in the gas cell as a consequence of the interaction between the oxygen anionic beam and the neutral molecular target. These ionic fragments are detected by MCP1 and the corresponding signal are recorded by a high-resolution digital oscilloscope (Tektronix MSO 3034, 2.5GS/s). In order to obtain the corresponding signal, it is necessary to guarantee that the primary beam is coincident with the extraction pulse. This situation is illustrated in figure 3.15 in the case of N<sub>2</sub> as target molecule. The extraction pulse (black line) can be delayed to select which part of the primary beam (dashed pink line) is generating the extracted ions (green line). This timing procedure also allows to select the mass of the primary anion species (O<sup>-</sup> or O<sub>2</sub><sup>-</sup>) by simple time filtering. In other words, to ensure that the observed mass spectrum is the result of a collision between O<sub>2</sub><sup>-</sup> (and not O<sup>-</sup>) with a neutral target molecule, it is necessary to tune the extraction pulse to the intensity peak assigned to O<sub>2</sub><sup>-</sup>, as shown in figure 3.15. In this figure we can also appreciate that the primary beam signal is attenuated (pink line) when the positive/negative extraction pulse is applied and, in the case shown, the attenuation occurs at the O<sub>2</sub><sup>-</sup> local maximum.

Measuring the intensity of the corresponding ionic fragments formed during the collision is possible to evaluate the partial relative cross-sections for the production of these positive and negative ions as a function of the incident anion energy. These relative values are obtained through the ratio of the detected positive/negative fragment intensities to the corresponding oxygen (O<sub>2</sub><sup>-</sup>) primary beam intensity at the centre of the scattering chamber for different values of the target gas pressure (equation 3.12). For each incident energy, the intensity of the ions ( $I_{+/-}$ ) is directly recorded by the MCP1 microchannel plate and the intensity of the oxygen negative beam in the centre of the

chamber ( $I_0$ ) is determined from the  $O_2^-$  intensity measured by the MCP2 but corrected from the attenuation which is calculated from the corresponding total cross-section value. The total relative positive/negative ionisation cross-sections are then the sum of the corresponding partial cross-sections ( $\sigma_{+/-}$ ).

$$\sigma_{+-} = \frac{I_{+-}}{I_0} \frac{1}{nl} \quad (3.12)$$

Where  $n$  is the neutral molecular gas density and  $l$  is the effective collision length.

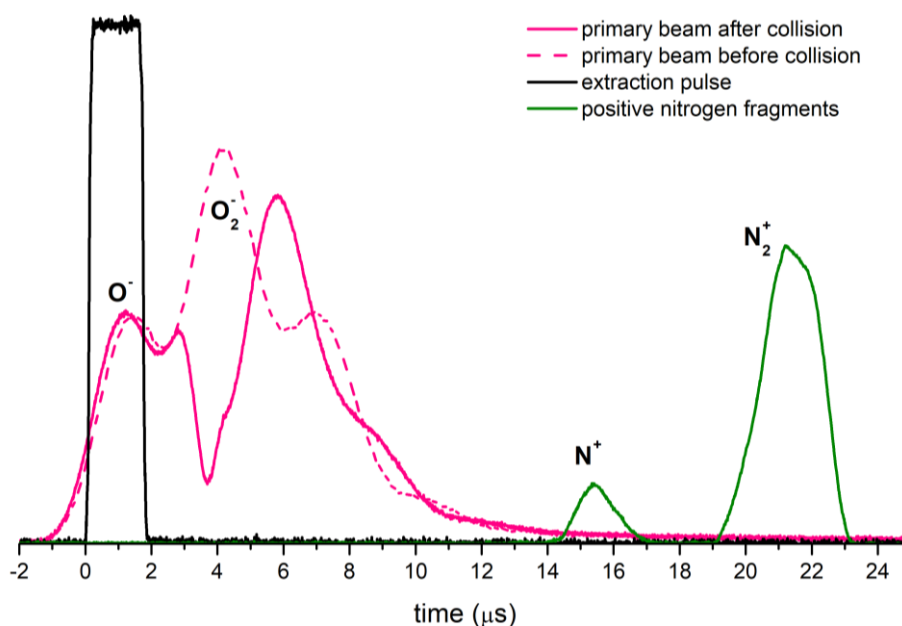


Figure 3.15. Example of a time-of-flight mass spectrum of  $N_2$  at 560 eV where: the black line is the extraction pulse at  $E_1$ , the pink line is the anionic incident beam and the green line is the collision resultant positive ions.

### 3.2.5 Optimisation procedures

Since this is a novel experimental system, several optimisation procedures were carried out in order to find the appropriate working conditions and verify its reliability. Time calibration tests were initially made for different discharge precursor gases: hydrogen ( $H_2$ ), oxygen ( $O_2$ ), carbon dioxide ( $CO_2$ ) and argon ( $Ar$ ). Considering the time of appearance of each mass a calibration curve was obtained to be used *a posteriori* for other precursor gases. In figure 3.16 we show four spectra obtained with different precursor gases (a) and the corresponding calibration curve (b).

In order to check the reliability of the entire system, first measurements were carried out for  $O_2^-$ -colliding with nitromethane ( $CH_3NO_2$ ), a benchmarking molecule for which the electron transfer fragmentation patterns are very well-known [66,98]. In addition,  $O_2^-$ -nitromethane collisions were previously studied by our research group and the results were already published by Oller *et al.* [126].

Since then, as a part of this doctoral project, important modifications of the system have been implemented and therefore, we can consider the present measurements with nitromethane as an additional calibration procedure. As an example, figure 3.17 shows a mass spectrum of the positive fragmentation induced to CH<sub>3</sub>NO<sub>2</sub> by O<sub>2</sub><sup>-</sup> collisions indicating the mass of the observed fragments.

After that, in order to analyse the composition and purity of the oxygen gas introduced into the projectile chamber, four different working conditions were tested by using a quadrupole mass spectrometer (with and without discharge). These situations are represented in figure 3.18. The first one is a background measurement which will be subtracted to all the subsequent measurements. The next situation corresponds to operating the pulsed valve letting the oxygen gas to enter the projectile chamber (O<sub>2</sub> gas situation). As seen from this figure there is an increment of the neutral 32 u mass fragment in the quadrupole mass spectrum. Once oxygen is inside the chamber, a voltage drop between the cathode and anode is applied to generate the discharge (O<sub>2</sub> gas + discharge situation) and the intensity of neutral oxygen decreases, as expected, since part of the neutral oxygen is ionised into the discharge. The final condition (O<sub>2</sub> gas + discharge situation + G<sub>2</sub> voltage) is similar to the previous one but applying a negative voltage to grid G<sub>2</sub>. No relevant change found in the latter situation indicates that negative ions are not distorting the O<sub>2</sub> intensity measured by the QMS.

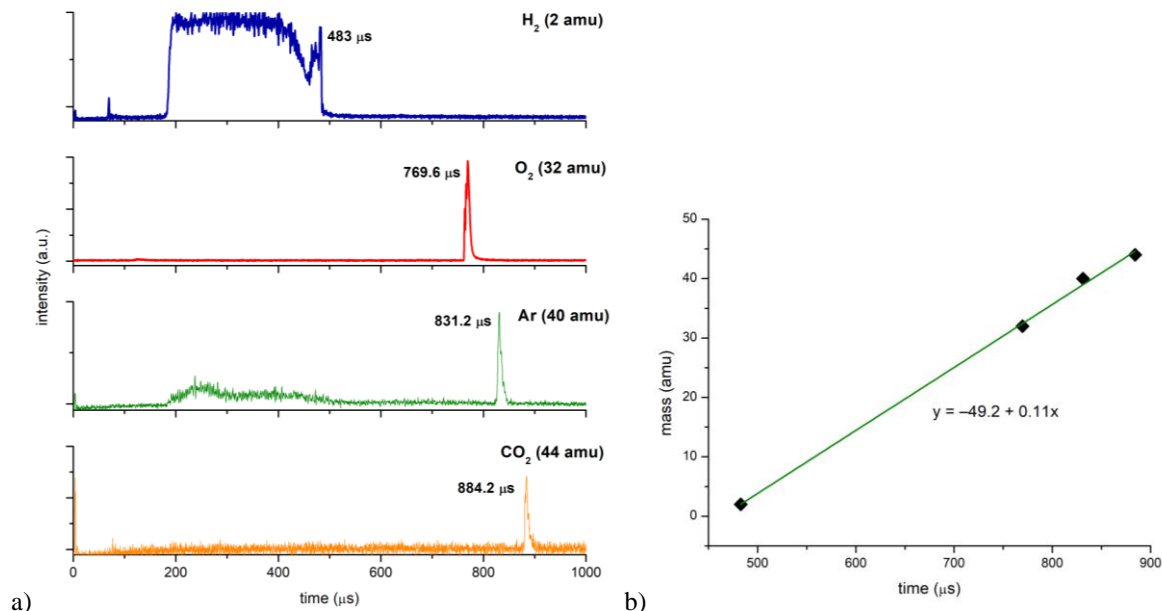


Figure 3.16. a) time-of-flight spectra of different discharge precursor gases: hydrogen (blue line), oxygen (red line), argon (green line) and carbon dioxide (yellow line); b) calibration curve time x mass.

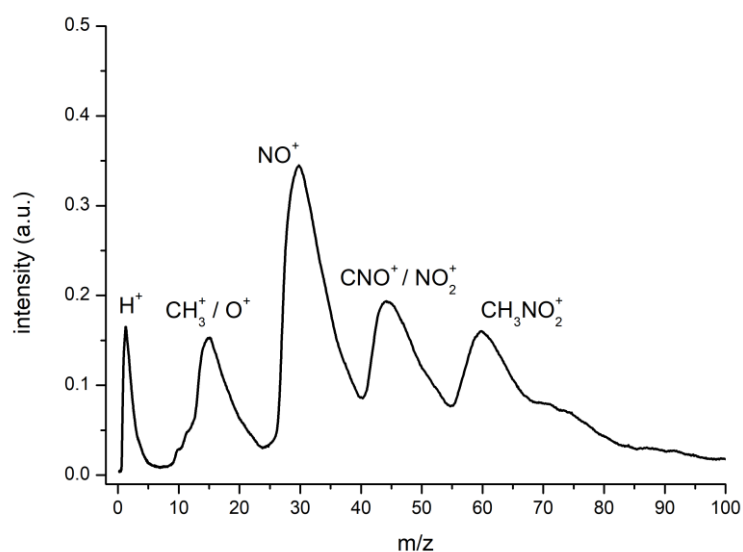


Figure 3.17. Time-of-flight mass spectrum of positive ions detection in  $O_2^- + CH_3NO_2$  at 1300 eV (lab frame).

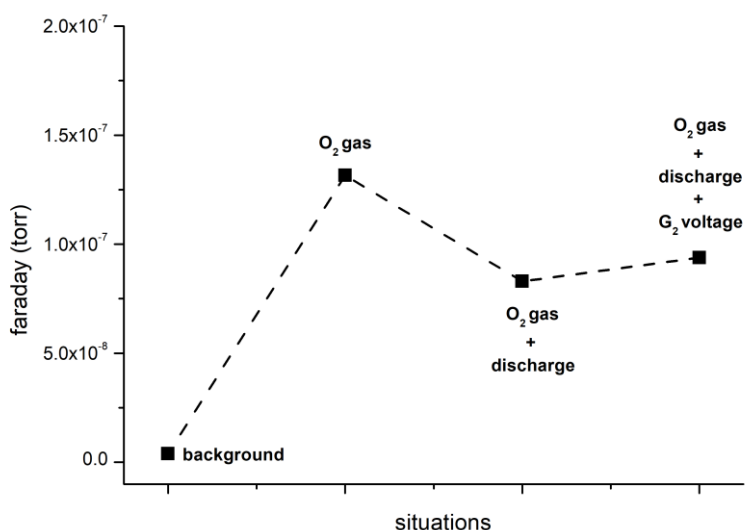


Figure 3.18.  $O_2$  precursor discharge gas analysis in four different situations.

### 3.2.6 Vacuum system

The vacuum conditions are achieved making use of four turbomolecular pumps, one for the projectile chamber (AGILENT 510 l/s), two for the collision chamber (Pfeiffer 445 l/s and Varian 210 l/s) and the last one for the transmission chamber (attached to the QMS). The three chambers are separated by 2 mm diameter collimator holes which guarantee a differential pumping, with an ultimate pressure of  $4.6 \times 10^{-7}$  mbar ( $4.6 \times 10^{-5}$  Pa) in the projectile chamber and  $3.2 \times 10^{-8}$  mbar ( $3.2 \times 10^{-6}$  Pa) in the collision and transmission chambers. The primary vacuum conditions of the three chambers are provided by two scroll and a two-stage rotary pumps with pumping speeds of 3.17 l/s, 1.8 l/s, and

0.92 l/s, respectively which ensure the normal operation conditions for the turbo pumps. The gas line to introduce the oxygen precursor into the pulsed valve is also pumped by an independent two-stage rotary pump.





# CHAPTER 4

## ELECTRON TRANSFER EXPERIMENTS IN K-MOLECULES COLLISIONS

### 4.1 Selective Bond Excision of Nitroimidazoles in Electron Transfer Experiments<sup>1</sup>

#### Abstract

We have performed comprehensive charge transfer experiments yielding negative ion formation in collisions of fast neutral potassium atoms with nitroimidazole and methylated derivative molecules. The anionic pattern reveals that in the unimolecular decomposition of the precursor parent anion, single and multiple bond cleavages are attained. Selective excision of hydrogen atoms from the N1 position in 4-nitroimidazole (4NI) is completely blocked upon methylation in 1-methyl-4-nitroimidazole (Me4NI) and 1-methyl-5-nitroimidazole (Me5NI). Additionally, only (4NI) and 2-nitroimidazole (2NI) are efficient in selectively producing neutral OH<sup>•</sup> and NO<sup>•</sup> radicals in contrast to (Me4NI) and (Me5NI). These findings present a novel experimental evidence of selective chemical bond breaking by just tuning the proper collision energy in atom-molecule collision experiments. The present work opens up an opportunity to contribute to the current need of pinpointing many more charge transfer collisions that can initiate selective reactivity of the kind demonstrated here, extending to tailored chemical control for different applications such as in tumour radiation therapy through nitroimidazole based radiosensitisation.

---

<sup>1</sup> This chapter is based on the following submitted publication: M. Mendes, M. Probst, G. García, P. Limão-Vieira. Selective Bond Excision of Nitroimidazoles in Electron Transfer Experiments (2019)

Nitroimidazoles and derivatives have been used as potential radiosensitiser chemical compounds in tumour hypoxia [79,127] and recently two new fluorine-18 labelled 2-nitroimidazole derivatives were successfully prepared to be used as potential PET radioligands for tumour imaging [128]. It is commonly accepted within the international community that the underlying molecular mechanisms that govern the radiosensitisation process of the nitroimidazole-based chemical compounds are still unknown. Yet, it is believed that the most relevant mechanism within cells deprived of oxygen is a complex redox reaction where the nitroimidazole ring facilitates such process via formation of negative radical ions [82,129]. Low-energy electrons (<15 eV) have been recognized to yield relevant by products of radiation induced damage to DNA/RNA molecular constituents [52,130]. Such high efficiency in changing the chemical environment is attained through formation of a transient negative ion (TNI) that can subsequently dissociate into stable fragment anions ( $X^-$ ) and neutral radical (R) species. Such mechanism is known as DEA. Interesting to note that electron induced bond breaking pertains to the role of electron transfer processes which may be more prevalent under physiological conditions rather than free electron attachment processes [51]. Electron transfer processes leading to ion-pair formation (reaction 4.1), can be properly investigated in atom-molecule collision experiments, where an electron donor (K=potassium) with low ionization energy (4.34 eV) delivers to the target molecule (M) the extra charge, leaving the molecular compound in a metastable state ( $M^{\#}$ ):



The electron transfer process, yielding a particular radical anion, is dictated by non-adiabatic transitions between the neutral (K M) and ionic ( $K^+ M^{\#}$ ) potential energy curves involved in the collision [91]. Such mechanism is operative if the relative kinetic energy of the collision partners is greater than  $\Delta E$ , the electron donor ionization energy (IE) minus the electron affinity (EA) of the target molecule. For the set of molecules investigated, a typical  $\Delta E$  value < 4 eV is obtained, meaning that the molecular anion can be formed with an excess of internal energy. Given that in the present experiments the lowest collision energy is 10 eV, the efficiency of such electron transfer process allows to explore complex reactions associated with concerted cleavage of several bonds and the formation of new molecules, such as radicals  $OH^\bullet$  and  $NO^\bullet$ . Recent theoretical studies in the DNA/RNA pyrimidine [131] and purine [132] bases, have shown that electron transfer can excise several bonds at a threshold value of 5 eV to yield  $CNO^-$  and  $CN^-$ , respectively.

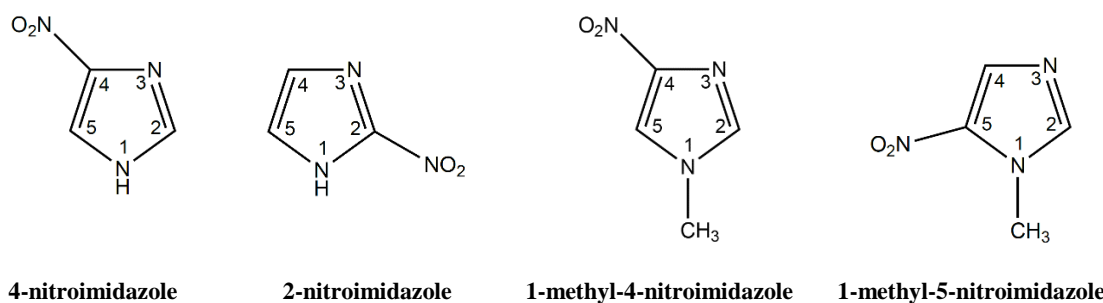


Figure 4.1. Molecular structures of 4-nitroimidazole (4NI), 2-nitroimidazole (2NI), 1-methyl-4-nitroimidazole (Me4NI) and 1-methyl-5-nitroimidazole (Me5NI).

The present study deals with negative ion formation in electron transfer experiments to 4-nitroimidazole (4NI), 2-nitroimidazole (2NI), 1-methyl-4-nitroimidazole (Me4NI) and 1-methyl-5-nitroimidazole (Me5NI) (figure 4.1) by means of a crossed molecular beam experiment coupled with time-of-flight (TOF) mass spectrometry for ion detection. In order to further our knowledge on the electronic structure of these molecules and helping with the assignment of the most relevant molecular orbitals, we have performed quantum chemical calculations at different levels of theory. In the gas-phase 4-nitroimidazole (4NI) and 5-nitroimidazole (5NI) coexist in a tautomeric equilibrium [133], where XPS measurements together with density functional theory (DFT) based theoretical calculations have found a relative population of 1:0.7 for 4NI:5NI at 390K [82]. Thus, 4NI and 5NI from now on referred as 4(5)NI. The negative ions TOF mass spectra at 100 and 10 eV lab frame collision energy (figure 4.2 and 4.3) show how sensitive the nitroimidazole molecules are to electron transfer induced decomposition. Interesting to note that 4(5)NI and 2NI, generally speaking, generate identical fragmentation patterns regarding the major anions formed, while a striking difference is observed with the methylated analogues, Me4NI and Me5NI.

The collision induced fragmentation pattern observed for 4(5)NI in electron transfer experiments, is remarkably suppressed at lower collision energy, viz. 10 eV, in their methylated forms (Me4NI and Me5NI). Such not only accounts for the loss of a hydrogen atom but to bond cleavages and intramolecular reactions yielding radical units. Such unprecedented electron transfer studies are here shown for H<sup>•</sup> loss, effective C–NO<sub>2</sub> bond breaking and complex reactions leading to OH<sup>•</sup> and NO<sup>•</sup> radicals formation.

Figure 4.2 depicts the negative ions TOF mass spectra where the closed shell dehydrogenated anion (M–H)<sup>–</sup> is only discernible for 4(5)NI and 2NI, although with a modest yield. Such loss of a neutral hydrogen atom may be described according to reaction (4.2):



In DEA experiments, the (M–H)<sup>–</sup> yield shows a series of sharp features below 2 eV and a broader resonance contribution at 3.4 eV. The former were assigned to vibrational Feshbach resonances

(VFRs) due to the considerable high dipole moments of 4NI (7.78 D) and Me4NI (8.50 D) [43], while the later to a  $\pi^*$  resonance subjected to vibronic coupling [43]. In electron transfer experiments, such VFRs are not expected to play a significant role unless highly excited Rydberg atoms have been used instead [134]. This is certainly not the case in the present experiments since the binding energy of the unpaired electron is 4.34 eV in the neutral potassium atom. TOF mass spectra were recorded at lab-frame collision energies of 10 and 100 eV ( $\sim 2.5$  and 65 eV in the centre-of-mass frame and from now on referred as available energy). For the lowest collision energy probed, the available energy is below the 3.4 eV  $\pi^*$  resonance, and so not expected to lead to dissociation as is the case of the TOF mass spectra depicted in figure 4.3. However, at an available energy of 5.7 eV (not shown here), 15 eV in the lab frame, no signal has been detected for Me4NI and Me5NI, indicating that in 4(5)NI the loss of H exclusively follows from the N<sub>1</sub> site and, as predictable, in the methylated forms that channel is completely blocked.

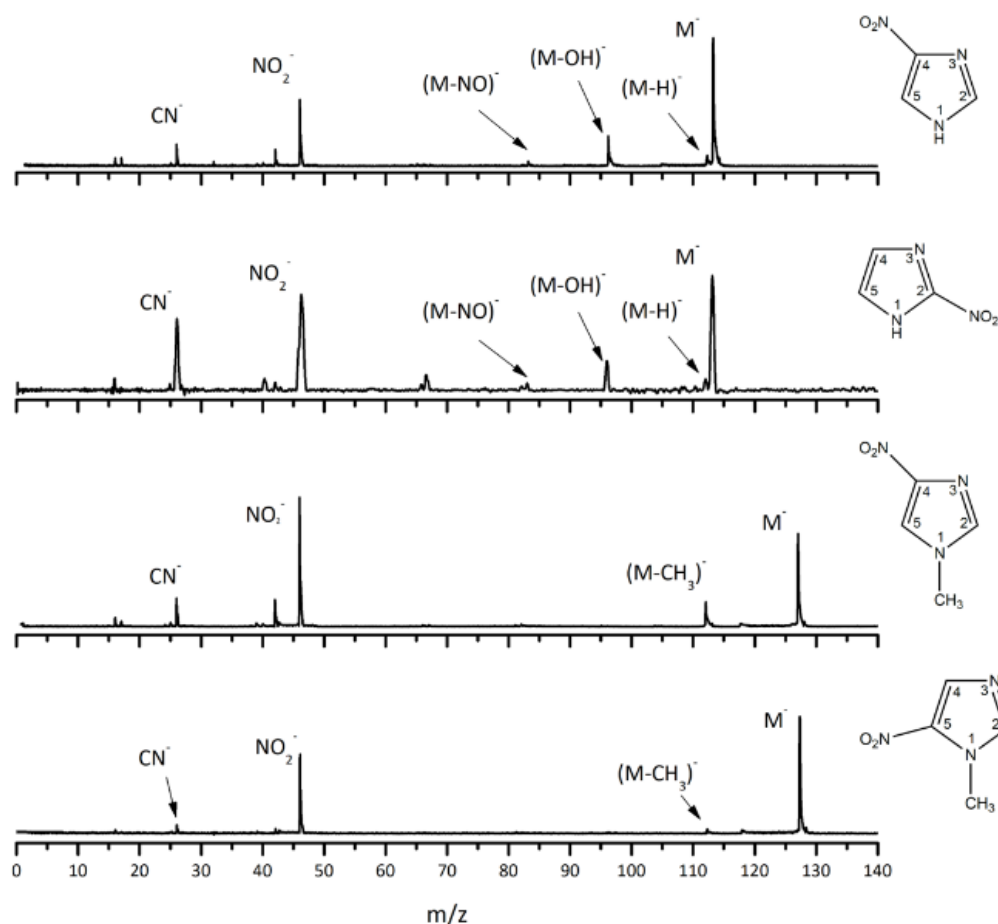


Figure 4.2. Time-of-flight mass spectra of negative ions from electron transfer experiments at 100 eV lab frame energy for 4(5)NI, 2NI, Me4NI and Me5NI.

Relevant to note that a similar behaviour has been observed in the DNA base adenine [132], where, as a function of the collision energy, the dehydrogenated parent anion is selective formed from the breaking of the C–H or N–H sites. Methylation at the N<sub>9</sub> and N-C<sub>6</sub> resulted in a complete quenching

of  $(M-H)^-$  meaning that the loss of H is exclusively from the N<sub>9</sub> site. It is remarkable that such fine control over reactivity can be achieved in an energetic collision between an atom and a relatively complex molecule with several competing relaxation channels. This reflects the specific dynamics of the three-body interaction involving the molecule, the transferred electron, and the donor atom, where a similar condition is expected in the present study.

Apart from the absence of H loss in the methylated forms, another relevant aspect pertains to a common pattern for all molecules investigated which are the  $NO_2^-$  and the metastable parent anion ( $M^-$ ) formations. Although the scope of the present contribution is not to address the formation of such anions,  $NO_2^-$  stems from the particular high electron affinity of  $NO_2$  while  $M^-$  long-lived lifetime (at least on the  $\mu s$  time scale of the TOF detection) is due to the different degrees of freedom, where the excess energy provided in the electron transfer process can be statically distributed, delaying autodetachment and successfully competing with dissociation.

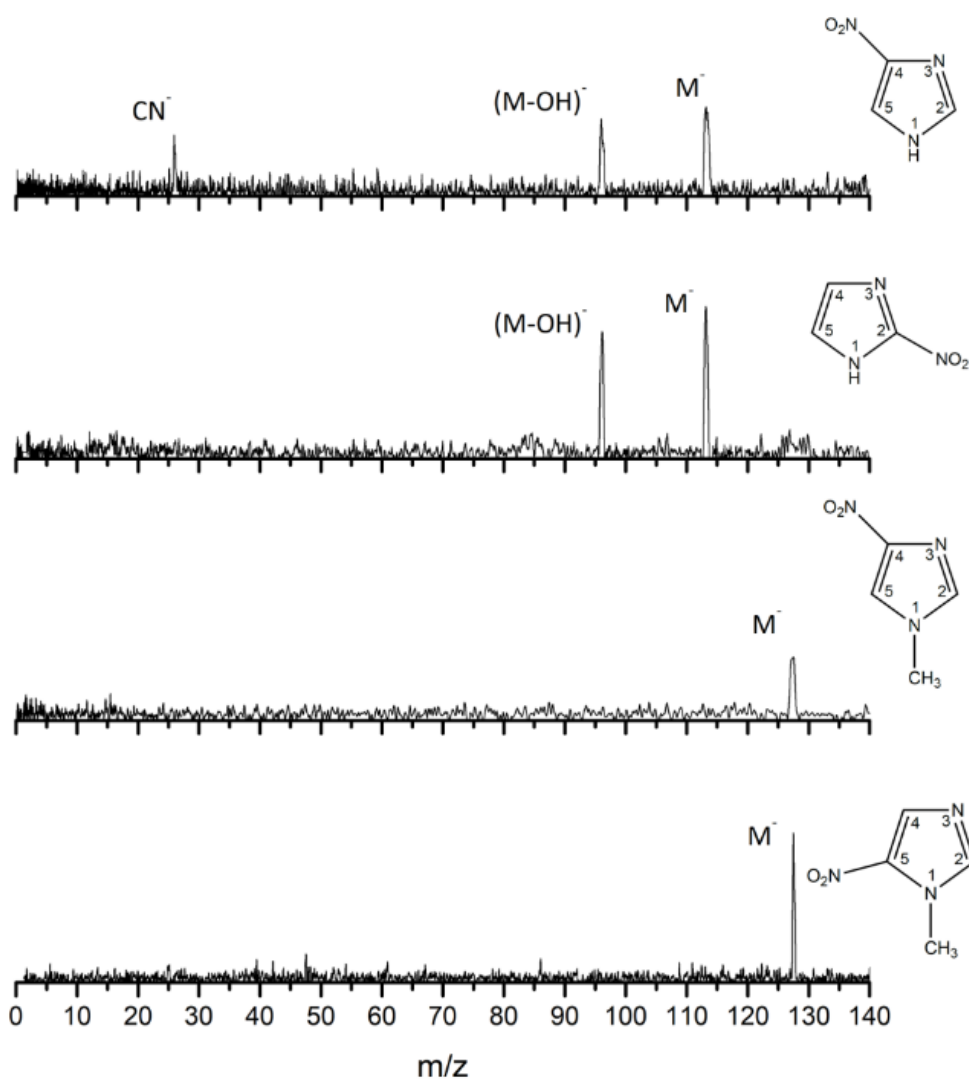


Figure 4.3. Time-of-flight mass spectra showing anions produced in electron transfer experiments at 10 eV lab frame energy for 4(5)NI, 2NI, Me4NI and Me5NI. The metastable parent anion  $M^-$  is visible for all cases while the loss of a  $OH^\bullet$  radical is only operative in 4(5)NI and 2NI, the former also showing  $CN^-$  formation.

We now turn our attention to the loss of the neutral OH<sup>•</sup> radical. The reaction yielding the hydroxyl radical requires the breaking of two bonds and the formation of an OH molecule. Such reaction is only operative for 4(5)NI and 2NI and is completely suppressed in Me4NI and Me5NI regardless the collision energy probed. This result is in striking contrast with DEA experiments where a single resonance centered at ~4 eV leads to (Me4NI–OH)<sup>•-</sup> formation [43]. The difference observed between the electron transfer process and the DEA mechanism can reside on the effect produced by the K<sup>+</sup> ion formed in the collision complex (K<sup>+</sup> M<sup>•+</sup>). Such strong coulomb interaction may delay autodetachment long enough, in particular in the low-collision regime (~83 fs for 10 eV), for the excess energy in the TNI to be redistributed through the different available degrees of freedom enhancing a favourable fragmentation channel. Moreover, for higher collision energies (~26 fs for 100 eV), such stabilization effect may no longer hold, and other fragmentation channels may be allowed in particular those resulting from statistical and/or direct dissociation. However, energy constraints cannot explain site selectivity and such differences may be also related to the electronic structure of the associated transient precursor ions accessed by electrons of different energies (either shape or core excited resonances) [135]. In recent occasions we have shown that the polarization by the potassium cation induces a global upward shift in energy of ~2 eV for the lowest  $\pi$  orbitals but the effect remains weak on the  $\sigma$  orbitals [131,136]. Although with a modest yield (figure 4.2), formation of (M–NO)<sup>•-</sup> results in the loss of a neutral NO<sup>•</sup> radical from the cleavage of the C–NO<sub>2</sub> and one of the two O=N=O bonds. This reaction is not effective at low-collision energies for the set of molecules studied (figure 4.3), while at higher energies (figure 4.2) such fragmentation channel is selectively limited to 4(5)NI and 2NI molecules only.

Finally, our attention turns to CN<sup>-</sup> formation, which is visible in the TOF mass spectra at 100 eV (figure 4.2) for all nitroimidazole molecules and the typical behaviour that methylation blocks its appearance at low collision energy (figure 4.3). The cyanide anion can be formed by involving an N atom either from the ring or the NO<sub>2</sub> group or simply from ring bond fragmentation. Such is supported by the quantum chemical calculations in Figure 4.4 (left column) where nodes in the wave functions are observed. Notwithstanding any of these complex reactions require substantial rearrangement in the TNI. DEA experiments in nitroimidazole and methyl nitroimidazole molecules, have shown that the reaction enthalpies yielding CN<sup>-</sup> are -3.2 eV and -3.3 eV, for 4NI and Me4NI (and Me5NI), respectively [137], making the former highly reactive in the presence of an extra electron whereas the later are blocked in their reactivity due to methylation. At 10 eV (figure 4.3) another interesting aspect of cyanide anion formation pertains to its discernibility only for 4(5)NI, where the signal is totally suppressed for 2NI. Such selectivity can be explained by looking at the radical anions electron spin densities for the single occupied molecular orbitals (SOMO) and  $\sigma^*$  orbitals in figure 4.4 for 4(5)NI, Me4NI and Me5NI, whereas for 2NI we convey the recent calculations in ref. [138]. Following the atoms numbering in figure 4.1, the wave function is delocalized along N<sub>1</sub>-C<sub>2</sub>, with nodes between N<sub>1</sub>-C<sub>5</sub> and N<sub>3</sub>-C<sub>2</sub> in 4(5)NI, but not in 2NI. Also

relevant the fact that in 2NI there is no delocalized wave function over any N–C bond, meaning that  $\text{CN}^-$  in this molecule can only be formed at higher energies from  $\text{O}_2\text{N}-\text{C}_2$  (figure 4.2). Moreover, in 4(5)NI the  $\sigma^*$  orbital is localized mainly between N1-H with a smaller contribution within the ring. A transition to a  $\pi^*$  state does not lead to direct bond excision unless a repulsive  $\sigma^*$  state is crossed diabatically. However, if the available energy is enough to permit intramolecular electron transfer ( $\sigma^* \rightarrow \pi^*$ ), this mechanism is possible if the nuclear wavepacket survives long enough along the reaction coordinate to allow diabatic coupling between the two states. In the low-energy collision, the presence of  $\text{K}^+$  in the vicinity of the TNI may allow intramolecular electron transfer from  $\text{N}_1-\text{H}$  to the ring yielding  $\text{CN}^-$  although with a modest intensity. Such mechanism has been observed in pyrimidine [131] and adenine [136] bases of DNA probed in electron transfer collisions with K as the electron donor.

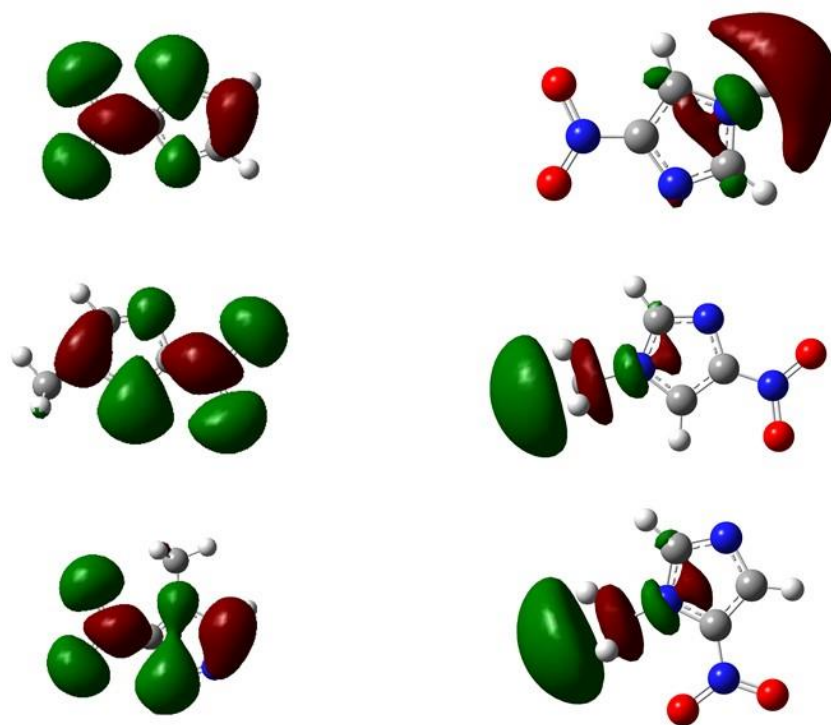


Figure 4.4. Left column: M06-2X/aug-cc-pvtz level of theory optimized structures of radical anions and their SOMOs; Right column: lowest  $\sigma^*$  orbitals from HF/D95VH level of theory, for 4(5)NI, Me4NI and Me5NI. C, N, and O atoms are represented in white, grey, blue and red colours, respectively. Positive and negative values of the wave function have a red and green colours, respectively.

In summary, it is shown that in collision induced electron transfer to nitroimidazole molecules, bond breaking selectivity is achieved upon methylation on the  $\text{N}_1$  site. Such methylation is not only responsible for blocking at low-collision energies the  $\text{N}_1-\text{CH}_3$  bond breaking channel but suppresses an essential decomposition channel yielding the neutral radical  $\text{OH}^\bullet$ . The modest yield of radical  $\text{NO}^\bullet$  is only operative at higher collision energies but limited to 4(5)NI and 2NI. Within the nitroimidazoles radiosensitisation potential use, the redox mechanism delivered in electron transfer

processes to these chemical compounds results in the formation of radicals with particular relevance to  $\text{NO}^\bullet$  and  $\text{OH}^\bullet$  to act as an indirect DNA damage agent triggered by ionizing radiation. In the case of nitric oxide, this radical has been acknowledged as a relevant cause to sensitize tumours to cytotoxic treatments (e.g. radiotherapy and chemotherapy) in hypoxic solid tumours, facilitating formation of new blood vessels (angiogenic effects), tumour perfusion, drug delivery and oxygenation [139].

#### 4.1.1 Experimental Section

The experimental setup is of a crossed molecular beam arrangement equipped with a high-resolution reflectron time-of-flight mass spectrometer (KORE R-500-6). A resonant charge exchange chamber allows neutral potassium beams to be generated in the laboratory frame from 8-1000 eV with an energy resolution of 500 meV [135] and an effusive beam of molecules was generated by vaporizing commercial molecular samples (4(5)-nitroimidazole, 2-nitroimidazole, 1-methyl-4-nitroimidazole and 1-methyl-5-nitroimidazole) in an oven heated to temperatures between 300 and 458 K depending on the sample. The samples were purchased from Sigma-Aldrich with a stated purity of  $\geq 97\%$  while Me4NI was purchased by Fluorochem with a stated purity of  $\geq 95\%$ . The energy scale was calibrated with the  $\text{K}^+$  energy loss features of  $\text{CH}_3\text{NO}_2$  and  $\text{CCl}_4$ , and mass scale with the well-known anions formed upon potassium collisions with  $\text{CH}_3\text{NO}_2$ . For more details see Section 3.1.

#### 4.1.2 Theoretical Section

The M062x/aug-cc-pVTZ level of theory for geometry optimization, calculation of molecular eigenfrequencies in the harmonic approximation, and exploration of parts of the potential energy surfaces was used. For calculation of the dipole-bound states of the considered anions, we re-optimized the neutral molecules at the MP2/cc-pVTZ level of theory before calculating the vertical electron affinities corresponding to dipole-bound states in subsequent single-point calculations employing large sets of diffuse basis functions. The resulting geometries were, however, very similar to those obtained with M062x. To describe the diffuse form of the wave function of the loosely bound electron, we generated an even-tempered sequence of diffuse functions according to the scheme given by Woon and Dunning [140] to construct a set of basis sets augmented with multiple diffuse functions based on the aug-cc-pVDZ and aug-pVTZ basis sets [141,142]. We found that, on inclusion of a sequence of four diffuse s and p functions on the H, C, N, and O atoms and a sequence of three diffuse d functions (and f functions in case of the quadruple-zeta basis) on the C, N, and O atoms, the VEAs of all three considered isomers could be regarded as converged and are not affected much by the number of used polarization functions. Electron correlation effects have been reported to significantly change the properties of dipole-bound anions [143–145]. In addition, the use of size-extensive methods such as MP2 is imperative, as the electron affinities are obtained by subtracting the energies of anion and respective neutral molecule [146]. Hence, we employed the spin-



unrestricted MP2 method. However, we found that HF already describes the identified dipole-bound states qualitatively correct. Following the guidelines of Gutowski *et al.* [147] we avoided erroneous results from the default direct SCF calculations due to the use of the large sets of diffuse functions by using full integral accuracy throughout the SCF calculations and evaluating two-electron integrals with an accuracy of  $10^{-20}$  au in the single-point calculations. All calculated structures and other details of the calculations are provided in ref. [138]. All calculations were performed with the Gaussian 09 program package [148].

## 4.2 Dynamics of Negative Ions in Potassium Collisions with Imidazole, Nitroimidazoles and Methylated Compounds<sup>2</sup>

### Abstract

We report on a combined experimental and theoretical study of electron-transfer-induced decomposition of nitroimidazole molecules and methylated compounds in collisions with neutral potassium (K) atoms. Time-of-flight negative ion mass spectra have been obtained in a wide collision energy range (10–1000 eV in lab frame), providing a comprehensive investigation of the fragmentation patterns of 4-nitroimidazole (4NI), 2-nitroimidazole (2NI), 1-methyl-4-nitroimidazole (Me4NI), 1-methyl-5-nitroimidazole (Me5N) and imidazole (IMI). Following Section 4.1 on site and bond selectivity in nitroimidazoles upon methylation which induced suppression of several fragmentation channels, this work focuses on the comprehensive description of the main fragment anions formed in such collisions. In the present work dissociation channels that are accessible in free electron attachment experiments are absent from the present mass spectra, notably formation of the parent anion in nitroimidazole compounds. This can be understood in terms of a relatively long transit time of the  $K^+$  cation in the vicinity of the temporary negative ion (TNI) enhancing intramolecular electron transfer in the TNI. In imidazole the most abundant anionic fragments have been assigned to the dehydrogenated parent anion and  $C_2H_2N^-$ . *Ab initio* theoretical calculations were performed for 4-nitroimidazole (4NI), 1-methyl-4-nitroimidazole (Me4NI), 1-methyl-5-nitroimidazole (Me5N) and imidazole (IMI) supporting the experimental results.

---

<sup>2</sup> This chapter is based on the following publication in preparation: Dynamics of negative ions in potassium collisions with imidazole, nitroimidazoles and methylated compounds (2019).

### 4.2.1 Introduction

The 4-nitroimidazole (4NI;  $C_3H_3N_3O_2$ ; 113 amu), 2-nitroimidazole (2NI;  $C_3H_3N_3O_2$ ; 113 amu), 1-methyl-4-nitroimidazole (Me4NI;  $C_4H_5N_3O_2$ ; 127 amu) and 1-methyl-5-nitroimidazole (Me5NI;  $C_4H_5N_3O_2$ ; 127 amu) are nitro compounds belonging to the big family of nitroimidazoles, with their molecular structures shown in figure 4.5. They have been under investigation especially because of their electron-affinic properties to be used as radiosensitisers in radiation treatments, namely in solid tumours growing in a hypoxic environment [78]. However a detailed knowledge of the underlying molecular mechanisms upon irradiation are still unknown. A working hypothesis is that these molecules undergo redox reactions inside the cells that are deficient in oxygen, and that the nitroimidazole ring facilitates reduction via the formation of radical anions. Nitroimidazoles investigation as radiosensitisers have advanced in the context of new compounds as oxygen mimics as well as inhibitors of carbonic anhydrase and new diagnostic imaging probes for hypoxic tumours [149]. In particular, the 5-nitroimidazole, nimorazole was shown to be effective in several clinical trials and it has been in routine use in the treatment of head and neck cancers in Denmark [79,150], especially for patients with high concentrations of osteopontin in their plasma. The molecular mechanisms related to the reactions involving nitroimidazoles after irradiation are not fully understood yet. Therefore its understanding means a key step for the development of new radiotherapeutic drugs and treatments. Feketeová *et al.* [81] have reported on the formation of radical ions from radiosensitisers using electrospray ionisation. The principal key finding was that radical anions are directly formed via electrospray ionization and was shown to be related to their electron affinities of misonidazole and nimorazole. Misonidazole shows more complex fragmentation which can be related to the observed higher toxicity in comparison to nimorazole. A more recent work by Pandeti *et al.* [151] also investigated the nitroimidazolic radiosensitisers by electrospray ionisation time-of-flight mass spectrometry and density functional theory. The photoelectron spectra and electronic structures of nimorazole were also investigated by Feketeová *et al.* [82], showing that 4-nitroimidazole (4NI) and 5-nitroimidazole (5NI) are regioisomers that in the gas phase coexist in a tautomeric equilibrium in a ratio of 1:0.7. The 4NI isomer was also found to be more stable than 5NI in water and in the crystalline state [10]. Tanzer and co-workers [43,84] demonstrated that low-energy electrons (0-8 eV) effectively decompose 4-nitroimidazole and two methylated isomers via DEA. The observation that neutral and radical anions are formed via DEA at high efficiency already at threshold (0 eV) show the significant importance of the study of the molecular mechanisms involved in these reactions and emphasises the implications of that for the development of nitroimidazole-based radiosensitisers in tumour radiation therapy. Yu and Bernstein [85] demonstrated that the decomposition of three distinct nitroimidazole model molecules following electronic excitation generates NO as an initial decomposition product at the nanosecond laser excitation wavelengths, with vibrational warm and rotational cold distributions of the NO product,

which are independent of excitation wavelengths. Cartoni *et al.* [152] have studied the 2- and 4(5)-nitroimidazole decomposition induced by VUV ionisation. Experimental and theoretical results have shown several resultant compounds, such as CO, HCN, NO and NO<sub>2</sub>. Theoretical fixed-nuclei scattering calculations using the Schwinger multichannel (SMC) method were performed by Kossoski and Varella [153] to interpret the consequences of methylation of nitroimidazoles at the N<sub>1</sub> site.

Imidazole (IMI; 68 amu) is a five-member aromatic molecule containing two nitrogen atoms. The molecular formula is C<sub>3</sub>H<sub>4</sub>N<sub>2</sub> (figure 4.1) and is polar in nature with a dipole moment of 3.8 D. This ring is present in several biological molecules, like histidine, purines, nitroimidazole, antifungal drugs and antibiotics [154]. The imidazole is also being used in the synthesis of new drugs and it is found in diverse molecules acting in anti-inflammatory, anticancer, antimicrobial, analgesic, and anti-tubercular activity [155]. At an atomic and molecular level some studies have been performed regarding the integrity of the IMI ring. In DEA, Ribar *et al.* [156] demonstrated that two low-energy shape resonances at 1.52 and 2.29 eV lead to the most abundant dehydrogenated anion (IMI-H)<sup>-</sup> through dehydrogenation at the N<sub>1</sub> position. They have also shown that upon electron attachment several more complex reactions involve the entire molecule, producing several small fragments associated to a complete dehydrogenation induced by a simple reaction. Modelli and Burrow [157] investigated by electron transmission spectroscopy, electron attachment energies of selected aza-derivatives including imidazole. They observed that the replacement of a CH group in a ring with a nitrogen atom increases the electron-acceptor properties. Additionally, they also found experimentally the value of 3.12 eV for the imidazole vertical attachment energy (VAE), and two  $\sigma^*$  orbitals ( $\sigma_{\text{ring}}^*$  and  $\sigma_{\text{NH}}^*$ ) at 7.6 eV and 5.9 eV, respectively. The excess electron binding energies of IMI was obtained by Rydberg electron transfer spectroscopy by Carles *et al.* [158]. Gianola *et al.* [159] investigated via negative ion photoelectron spectroscopy the imidazolidine anion, which corresponds to the de-hydrogenated parent anion and obtained the electron affinities of the imidazolyl radicals upon deprotonation at different sites.

In this chapter we report for the first time negative ion formation in neutral potassium-neutral nitroimidazoles/imidazole collisions, together with *ab initio* calculations to support the experimental findings. In the next sections we describe briefly the experimental s (further explained in Section 3.1) and the theoretical methods, the results obtained and the main conclusions that can be drawn from this investigation.

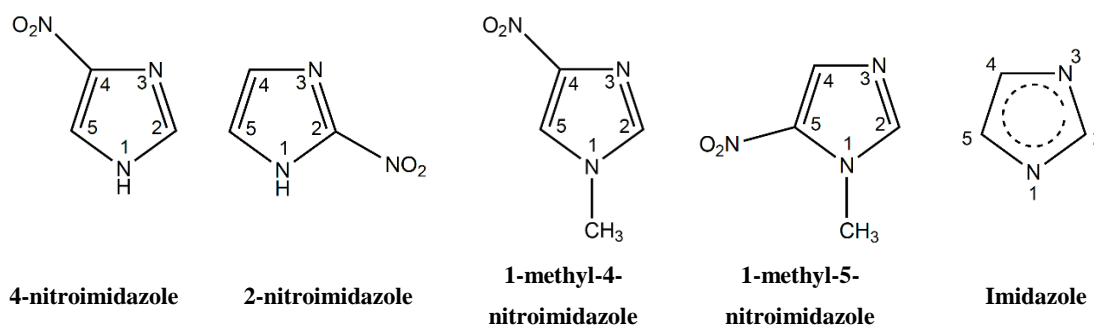


Figure 4.5. Molecular structure of 4-nitroimidazole, 2-nitroimidazole, 1-methyl-4-nitroimidazole, 1-methyl-5-nitroimidazole and imidazole.

### 4.2.2 Experimental Methods

The crossed molecular beam setup used to study collisions of neutral potassium (K) atoms with neutral nitroimidazoles and related molecules, has been described in Section 3.1. Briefly, an effusive target molecular beam crosses a primary beam of fast neutral K atoms and the product anions are analysed using a reflectron (KORE R-500-6) and dual-stage linear time-of-flight (TOF) mass spectrometers. The K beam is produced in a resonant charge exchange chamber from the interaction of  $K^+$  ions from a potassium ion source (10–1000 eV in the lab frame) with gas-phase neutral potassium atoms from an oven source. Mass spectra (resolution  $m/\Delta m \approx 800$ ) were obtained by subtracting background measurements (without the sample) from the sample measurements. Mass calibration was carried out on the basis of the well-known anionic species formed after potassium collisions with nitromethane [160]. The molecular samples 4-nitroimidazole, 2-nitroimidazole and 1-methyl-5-nitroimidazole were supplied by Sigma Aldrich with a stated purity of  $\geq 97\%$ . The 1-methyl-4-nitroimidazole was purchased by Fluorochem with a stated purity of  $\geq 95\%$ , and imidazole was supplied by Alpha Aesar with a stated purity of 99%. The solid samples were used as delivered.

### 4.2.3 Theoretical Method

The M062x/augcc-pVTZ level of theory for geometry optimization, calculation of molecular eigenfrequencies in the harmonic approximation, and exploration of parts of the potential energy surfaces was used. For more details see Section 4.1.

### 4.2.4 Results and Discussion

This chapter is complementary to Section 4.1 on electron transfer from neutral potassium atoms to 4NI, Me4NI and Me5NI showing that methylation at  $N_1$  site can selectively block several fragmentation channels. In this section we present results on negative ion formation in electron transfer from neutral K atoms to a set of molecules, 4NI, 2NI, Me4NI, Me5NI and imidazole, combining experimental and theoretical methods to analyse the full fragmentation pattern.

Dissociative electron transfer TOF mass spectra were obtained at laboratory frame collision energies of 10–1000 eV (~1.4–680 eV available energy in the centre-of-mass frame). Table 4.1 is a compilation of all the assignments for the anions detected for the five molecules investigated.

Figures 4.6, 4.8 and 4.10 depict the TOF mass spectra recorded at 30, 100 and 500 eV lab frame collision energy for 4NI, 2NI, Me4NI and Me5NI, respectively. Figure 4.12 shows the TOF mass spectra for imidazole at 30, 100 and 500 eV lab frame, while branching ratios (BRs) for the major fragments of 4NI, Me4NI, Me5NI and imidazole as a function of the collision energy are presented in figures 4.7, 4.9, 4.11 and 4.13, respectively.

The TOF mass spectra yields of 4NI and 2NI are very similar and reveal that they are, generally speaking, dominated by the parent anion ( $4\text{NI}^-$  and  $2\text{NI}^-$ ),  $\text{NO}_2^-$ ,  $\text{CN}^-$  and the loss of OH. The methylated compounds also show a strong evidence of parent anion ( $\text{Me}4\text{NI}^-$  and  $\text{Me}5\text{NI}^-$ ),  $\text{NO}_2^-$  and  $\text{CN}^-$  formation. The loss of OH is not observed for the methylated molecules as explained in Section 4.1. Regarding the simple ring, imidazole, no parent ion is observed which can be rationalized in terms of the high electron affinity of the imidazolyl radical  $[\text{IMI} - \text{H}]^\cdot$  to be 2.613 eV in the case of deprotonation at the  $\text{N}_1$  position, and 1.992 eV in the case of deprotonation at the  $\text{C}_5$  position [159]. Moreover, imidazole the major anionic fragments are the dehydrogenated parent anion  $(\text{IMI}-\text{H})^-$ ,  $\text{CN}^-$  and  $\text{C}_2\text{H}_2\text{N}^-$ . The latter is related with the loss of a HCN unit from the dehydrogenated parent anion, which also leads to  $\text{CH}^-$  formation (loss of another HCN unit). Such HCN loss mechanism is also operative in more complex molecules and was already observed for potassium collisions with adenine and derivative compounds [1] and pyrimidine [161]. One of the most important difference found in the present results compared with DEA measurements [84] is the parent anion formation for all molecules, except the case of imidazole. Such differences can be explained by the presence of cation potassium ( $\text{K}^+$ ) in the vicinity of the TNI formed upon electron transfer, i.e.  $\text{K} + \text{M} \rightarrow \text{K}^+ \text{M}^-$ . The strong Coulombic interaction may delay autodetachment allowing time enough to “stabilize” the system and redistribute the excess energy in the TNI through the different available degrees of freedom leading to different fragmentation channels. Identical rationale was put forward in the case of nitromethane as molecular target in potassium collisions [160], but the parent anion was not the strongest anionic fragment formed. Moreover, in electron transfer processes, an electronic transition accessing  $\pi^*$  states does not lead to direct bond cleavage unless a repulsive  $\sigma^*$  is crossed diabatically. However, the available energy is enough to give access to intramolecular electron transfer ( $\pi^* \rightarrow \sigma^*$ ), which is possible if the nuclear wavepacket survives long enough along the reaction coordinate to allow diabatic coupling between the two states.

We now discuss the majority of the anions formed in such potassium-molecule collisions. Note that formation of the dehydrogenated parent anion was already discussed in Section 4.1 and no further discussion will be performed here.

## Nitroimidazoles and methylated compounds

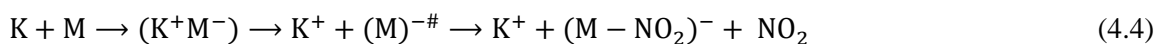
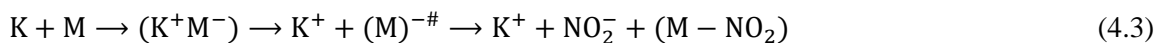
### Parent anion formation

The parent anion formation detected in all molecules in study is one of the most interesting processes observed in these measurements, especially for high impact collision energies. The BRs of these molecules as a function of the available energy (figures 4.7, 4.9 and 4.11) show that the parent anion is formed for all energies and, in the case of 4NI, represents the most intense anion between 5.7 eV and 664 eV available energy. At higher collision energies 4NI<sup>-</sup> accounts for around 60% of the total anion yield. In collisions using methylated nitroimidazole compounds, the parent anion accounts for ~70% and ~60% of total anion yield, in Me5NI and Me4NI, respectively. However, for Me5NI at energies between 6 and 13 eV the most intense fragment is (Me5NI – CH<sub>3</sub>)<sup>-</sup>, and for Me4NI at energies between 16 and 51 eV the most intense anion is NO<sub>2</sub><sup>-</sup>. Moreover, it seems that methylation at the N<sub>1</sub> position enhances parent anion formation. In DEA studies, the parent anion formation in 4NI is not observed, but in Me4NI and Me5NI [43,84]. Tanzer *et al.* have shown that the non-decomposed parent anion in Me4NI and Me5NI are formed within a very narrow resonance right at threshold (close to 0 eV). Such was explained based on the assumption that the electronic energy of the electron-attaching system, consisting by the energy of the incoming electron and the electron affinity of the molecule, is transferred to the vibrational degrees of freedom of the TNI, which delays autodetachment, into the μs time scale. The nitroimidazole molecules studied in this thesis have strong dipole moments (see table 4.2), well above the threshold of 2.5 D [162], and therefore can support stable dipole bound state (DBS). Indeed, the theoretical calculations in table 4.3 corroborate such statement. This means that under appropriate conditions, a weakly bound electron (e.g. in a Rydberg state) can be transferred to form a dipole-bound anion which may lead to valence states [163]. These molecules also have positive electron affinities (see table 4.2) which means that the ground state of the anion lies below the neutral molecule. Molecules with positive electron affinities lead to the formation of stable anions where the extra electron exists in a bound state [34]. Following this rationale, observation of the parent anion for all molecules in study is not surprising. However, for higher energy collisions, which means fast collisions, the presence of the parent anion is still evident as the most intense anion. Such observation is quite interesting since it seems do not follow completely the so-called adiabatic principle (see Chapter 2). The adiabatic principle describes that if the internuclear distance changes rapidly (fast collisions), the valence electron does not get sufficient time to switch from one atom to another atom or molecule. In that case the system remains in the same electronic configuration or diabatic state [164]. In the low-energy collision regime, the electron is transferred from the potassium atom to the nitroimidazole during the approximation, it means at the first crossing. Given the positive electron affinity of the target, a TNI can be formed where the excess of internal energy may be distributed over the different degrees of freedom delaying autodetachment. In this regime with typical collision times of the order of several tens of fs, the

presence of the  $K^+$  ion in the vicinity of the TNI (strong coulomb interaction) can also allow intramolecular electron transfer yielding dissociative channels, in particular fragments with high electron affinities as are the cases of  $NO_2$  and  $CN$ , with the resulting anion with a lifetime long enough to be detected through mass spectrometry. This description is much more attuned to adiabatic processes. Such rationale seems plausible since in the low-energy regime, typically below 50 eV, we observe the highest yields of fragment anions. However, when the collision energy is increased, the potassium atom may not transfer its electron at the first crossing but rather at the second. In this case, as the  $K^+$  ion flies away, there is no time enough for efficient intramolecular electron transfer and a non-adiabatic description is favourable, i.e. diabatic states can be described as those where the electronic character does not change with respect to the nuclear coordinates. Such makes sense since at high-collision energies, typically of the order of few fs, some vibrational modes within the molecular frame can be considered frozen [69]. Feketeová *et al.* [81] have performed electrospray measurements using different nitroimidazole molecules and derivatives to study radical anions formation in solution (viz. methanol). They observed that the parent anion radical ( $M^{\bullet-}$ ) is the most abundant in nimorazole, a derivative of 5-nitroimidazole. Such observations allow to suggest that these molecules can be used as potential radiosensitisers since the formation of radical anions is crucial in radiation therapy, especially in environments with deficiency in oxygen.

### **Formation of $NO_2^-$ , loss of neutral $NO_2$ and related multiple dehydrogenation ( $HNO_2^-$ , $H_2NO_2^-$ , $H_3NO_2^-$ )**

The  $NO_2^-$  yield is, together with the parent anion, one of the most intense in the nitroimidazoles TOF mass spectra, which is unsurprising because of its electron affinity, 2.27 eV [165]. For lower collision energies (e.g. 30 eV in the lab frame, figure 4.6) and in the case of the methylated compounds,  $NO_2^-$  corresponds to the most intense anion. Formation of  $NO_2^-$  occurs after cleavage of the simple  $C-NO_2$  bond (equation 4.3). However such bond breaking may also lead to the complementary reaction yielding  $(M-NO_2)^-$  (equation 4.4).



The BRs (figures 4.7, 4.9 and 4.11) show that the threshold of  $NO_2^-$  formation is 5.7 eV (15 eV lab frame), 6 eV (15 eV lab frame) and 2.5 eV (10 eV lab frame), for 4NI/2NI, Me4NI and Me5NI, respectively. This is consistent with DEA resonances found for these molecules [84]. Moreover, the BRs also provide an interesting aspect of the collision dynamics, where the parent anion and  $NO_2^-$  have complementary behaviour as function of the collision energy. Thus  $NO_2^-$  formation is more efficient at lower collision energies where direct electron transfer to the  $C-N$  bond is more favourable. Comparing the two methylated molecules where the  $NO_2$  group is in different positions



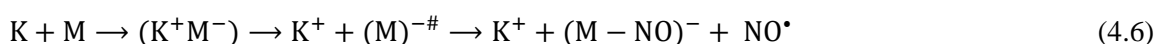
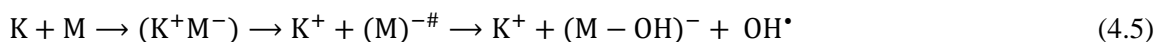
(C<sub>4</sub> for Me<sub>4</sub>NI and C<sub>5</sub> for Me<sub>5</sub>NI), the efficiency of NO<sub>2</sub><sup>-</sup> formation is higher for Me<sub>5</sub>NI at lower collision energies. The yield of formation can reach ~60% of the total anion yield at 6 eV, while in Me<sub>4</sub>NI it does not increase more than 30%. For higher collision energies both molecules show a similar behaviour as to the NO<sub>2</sub><sup>-</sup> yield accounting for ~20% of the total anion yield. In the case of methylated compounds, this means that, the position of the NO<sub>2</sub> group affects the strength of the C–N bond.

The loss of a neutral NO<sub>2</sub> leading to (M–NO<sub>2</sub>)<sup>-</sup> formation is also observed for all nitroimidazole molecules studied. However the intensity of such fragments is much lower than to the complementary reaction yielding NO<sub>2</sub><sup>-</sup>. These results are in quite good agreement with DEA studies [43,84], where for methylated compounds, below 2 eV, the reaction in equation 4.4 is completely suppressed, meaning that the methylation blocks the C<sub>4</sub> and C<sub>5</sub> positions. Such is not observed in the present results where the appearance of (M–NO<sub>2</sub>)<sup>-</sup> occurs at approximately the same energy for 4NI, 2NI and methylated molecules (around 30 eV lab frame).

Another interesting set of reactions related to the nitroimidazoles is the formation of anionic fragments at 66, 65 and 64 m/z, which are assigned to (M–HNO<sub>2</sub>)<sup>-</sup>, (M–H<sub>2</sub>NO<sub>2</sub>)<sup>-</sup> and (M–H<sub>3</sub>NO<sub>2</sub>)<sup>-</sup>. These ions are only observed for 4NI and 2NI (not shown here) but have not been reported in DEA measurements [84] at low electron impact energies. Such anion formation in potassium-4NI/2NI collisions may result from the loss of neutral H atom from the N<sub>1</sub> site together with the loss of NO<sub>2</sub> resulting in (M–HNO<sub>2</sub>)<sup>-</sup> formation. This is different to what occurs in DEA measurements [84] where they actually observed a block in formation of (M–HNO<sub>2</sub>)<sup>-</sup> upon methylation at low energies.

### Loss of neutral OH and NO

The loss of a neutral OH• (96 m/z) is one of the most intense anionic fragments observed in 4NI and 2NI (see figures 4.6, 4.8 and 4.10). Yet, after methylation at the N<sub>1</sub> site, the channel that leads to the formation of such anion is completely blocked, as explained in Section 4.1. A similar process seems to occur in (M–NO)<sup>-</sup> formation although the yield is much lower. These two anions can be formed through the reaction in equations 4.5 and 4.6.



The formation of these two negative ions requires the cleavage of several bonds, namely the cleavage of C–N, C–H and N–O bonds. Since the loss of neutral OH is suppressed upon methylation, we can assume that the H involved is originating from the position N<sub>1</sub>. The BRs (figures 4.7, 4.9 and 4.11) show that the threshold of (M–OH)<sup>-</sup> formation is 5.7 eV (15 eV lab frame) and 2.5 eV (10 eV lab frame), for 4NI and 2NI, respectively. Although (M–NO)<sup>-</sup> BR is not shown here, the threshold in the case of 4NI (19.8 eV) is much more higher than in 2NI (5.7 eV). This is consistent with DEA

resonances [84] and Ribar *et al.* [138]. These authors have observed that 2NI presents an enhancement in the fragmentation pattern compared to 4(5)NI. These two reactions seem to be of extremely importance within the biological environment further to low-energy electron transfer collisions. As discussed in Chapter 1 of this thesis, formation of highly reactive species as OH and NO in the cellular environment induces a set of reactions resulting in damage of the biocomponents including the DNA molecule. Since nitroimidazoles are being investigated as attuned radiosensitisers in radiotherapy of hypoxic tumours, the presence of such reaction channels may be extremely useful in the improvement of dedicated radiation protocols.

Table 4.1. Assignment of the negative ions formed in potassium collisions with 4-nitroimidazole (4NI), 2-nitroimidazole (2NI), 1-methyl-4-nitroimidazole (Me4NI), 1-methyl-5-nitroimidazole (Me5NI), and imidazole (IMI).

Mass m/z	4NI	2NI	Me4NI	Me5NI	IMI
1	H <sup>-</sup>	H <sup>-</sup>	H <sup>-</sup>	H <sup>-</sup>	H <sup>-</sup>
12					C <sup>-</sup>
13				CH <sup>-</sup>	CH <sup>-</sup>
14					CH <sub>2</sub> <sup>-</sup>
15				CH <sub>3</sub> <sup>-</sup> / NH <sup>-</sup>	CH <sub>3</sub> <sup>-</sup> / NH <sup>-</sup>
16	O <sup>-</sup> / NH <sub>2</sub> <sup>-</sup>	O <sup>-</sup> / NH <sub>2</sub> <sup>-</sup>	O <sup>-</sup> / NH <sub>2</sub> <sup>-</sup>	O <sup>-</sup> / NH <sub>2</sub> <sup>-</sup>	O <sup>-</sup> / NH <sub>2</sub> <sup>-</sup>
17	OH <sup>-</sup>	OH <sup>-</sup>	OH <sup>-</sup>	OH <sup>-</sup>	
24			C <sub>2</sub> <sup>-</sup>	C <sub>2</sub> <sup>-</sup>	C <sub>2</sub> <sup>-</sup>
25	C <sub>2</sub> H <sup>-</sup>		C <sub>2</sub> H <sup>-</sup>	C <sub>2</sub> H <sup>-</sup>	C <sub>2</sub> H <sup>-</sup>
26	CN <sup>-</sup>	CN <sup>-</sup>	CN <sup>-</sup>	CN <sup>-</sup>	CN <sup>-</sup>
39	C <sub>2</sub> HN <sup>-</sup> / C <sub>3</sub> H <sub>3</sub> <sup>-</sup>		C <sub>2</sub> HN <sup>-</sup> / C <sub>3</sub> H <sub>3</sub> <sup>-</sup>	C <sub>2</sub> HN <sup>-</sup> / C <sub>3</sub> H <sub>3</sub> <sup>-</sup>	C <sub>2</sub> HN <sup>-</sup> / C <sub>3</sub> H <sub>3</sub> <sup>-</sup>
40	C <sub>2</sub> H <sub>2</sub> N <sup>-</sup>	C <sub>2</sub> H <sub>2</sub> N <sup>-</sup>	C <sub>2</sub> H <sub>2</sub> N <sup>-</sup>	C <sub>2</sub> H <sub>2</sub> N <sup>-</sup>	C <sub>2</sub> H <sub>2</sub> N <sup>-</sup>
41					C <sub>2</sub> H <sub>3</sub> N <sup>-</sup> / CHN <sup>-</sup>
42	CNO <sup>-</sup> / CH <sub>2</sub> N <sup>-</sup>	CNO <sup>-</sup> / CH <sub>2</sub> N <sup>-</sup>	CNO <sup>-</sup> / CH <sub>2</sub> N <sup>-</sup>	CNO <sup>-</sup> / CH <sub>2</sub> N <sup>-</sup>	
46	NO <sub>2</sub> <sup>-</sup>	NO <sub>2</sub> <sup>-</sup>	NO <sub>2</sub> <sup>-</sup>	NO <sub>2</sub> <sup>-</sup>	
50					C <sub>3</sub> N <sup>-</sup>
64	(4NI – H <sub>3</sub> NO <sub>2</sub> ) <sup>-</sup>				
65	(4NI – H <sub>2</sub> NO <sub>2</sub> ) <sup>-</sup>				
66	(4NI – HNO <sub>2</sub> ) <sup>-</sup>	(2NI – HNO <sub>2</sub> ) <sup>-</sup>	(Me4NI – CH <sub>3</sub> NO <sub>2</sub> ) <sup>-</sup>	(Me5NI – CH <sub>3</sub> NO <sub>2</sub> ) <sup>-</sup>	
67	(4NI – NO <sub>2</sub> ) <sup>-</sup>	(2NI – NO <sub>2</sub> ) <sup>-</sup>			(IMI – H) <sup>-</sup>
68					(IMI – H) isotope
81			(Me4NI – NO <sub>2</sub> ) <sup>-</sup>	(Me5NI – NO <sub>2</sub> ) <sup>-</sup>	
82	(4NI – HNO) <sup>-</sup>		(Me4NI – CH <sub>3</sub> NO) <sup>-</sup>	(Me5NI – CH <sub>3</sub> NO) <sup>-</sup>	
83	(4NI – NO) <sup>-</sup>	(2NI – NO) <sup>-</sup>			
96	(4NI – OH) <sup>-</sup>	(2NI – OH) <sup>-</sup>	(Me4NI – HNO) <sup>-</sup>	(Me5NI – HNO) <sup>-</sup>	
112	(4NI – H) <sup>-</sup>	(2NI – H) <sup>-</sup>	(Me4NI – CH <sub>3</sub> ) <sup>-</sup>	(Me5NI – CH <sub>3</sub> ) <sup>-</sup>	
113	4NI <sup>-</sup>	2NI <sup>-</sup>			
114	4NI <sup>-</sup> isotope				
127			Me4NI <sup>-</sup>	Me5NI <sup>-</sup>	
128			Me4NI <sup>-</sup> isotope	Me5NI <sup>-</sup> isotope	

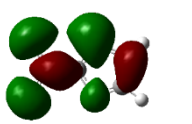
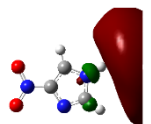
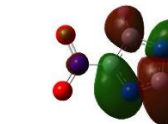
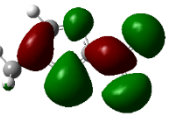
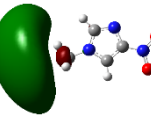
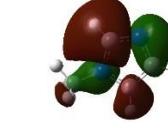
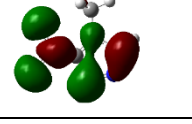
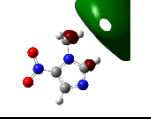
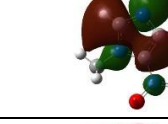
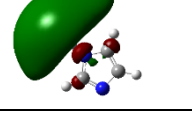
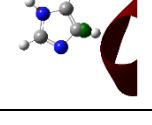
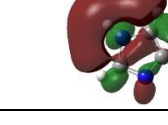
Table 4.2. Calculated dipole moments obtained with HF/aug-cc-pvtz level of theory and vertical electron affinities (VEAs) obtained with HF/D95V level of theory, for 4-nitroimidazole, 1-methyl-4-nitroimidazole, 1-methyl-5-nitroimidazole and imidazole.

Molecule	Dipole moment (D)		VEA (eV)
	Neutral	Anion	
4-nitroimidazole	7.78	11.18	0.99
1-methyl-4-nitroimidazole	8.45	13.5	1.47
1-methyl-5-nitroimidazole	4.40	7.98	0.91
Imidazole	3.79	11.52	-3.02

### CN<sup>-</sup> formation

The TOF mass spectra in figures 4.6, 4.8 and 4.10 show that CN<sup>-</sup> anion also contribute significantly to the total anion pattern of 4NI, 2NI, Me4NI and Me5NI. The CN<sup>-</sup> ion can be formed through the loss of an N atom from the NO<sub>2</sub> group or from the ring, or by excision of a CN unit directly from the ring. Both of these processes are formed after a complex rearrangement of the molecules after formation of the transient negative ion. The cyanide anion, CN<sup>-</sup>, was already observed for many biomolecules, such as pyrimidine [161], adenine [136], thymine and uracil [75] upon electron transfer with potassium as electron donor. According to the BR (not shown here) CN<sup>-</sup> threshold of formation is 9 eV for all the molecules except for 4NI, which is below 2.35 eV. This agrees with DEA experiments where a resonance near 0 eV and 4 eV for 4NI and 2NI, and around 4 eV in the case of methylated molecules [84,138] are operative.

Table 4.3. Calculated highest occupied molecular orbitals (HOMOs) and lowest unoccupied molecular orbitals (LUMOs) for 4-nitroimidazole (4NI), 1-methyl-4-nitroimidazole (Me4NI), 1-methyl-5-nitroimidazole (Me5NI) and imidazole (IMI) anions obtained at the M06-2X/aug-cc-pvtz level of theory.

	HOMO	LUMOs	
		$\pi^*$	$\sigma^*$
4NI			
Me4NI			
Me5NI			
IMI			

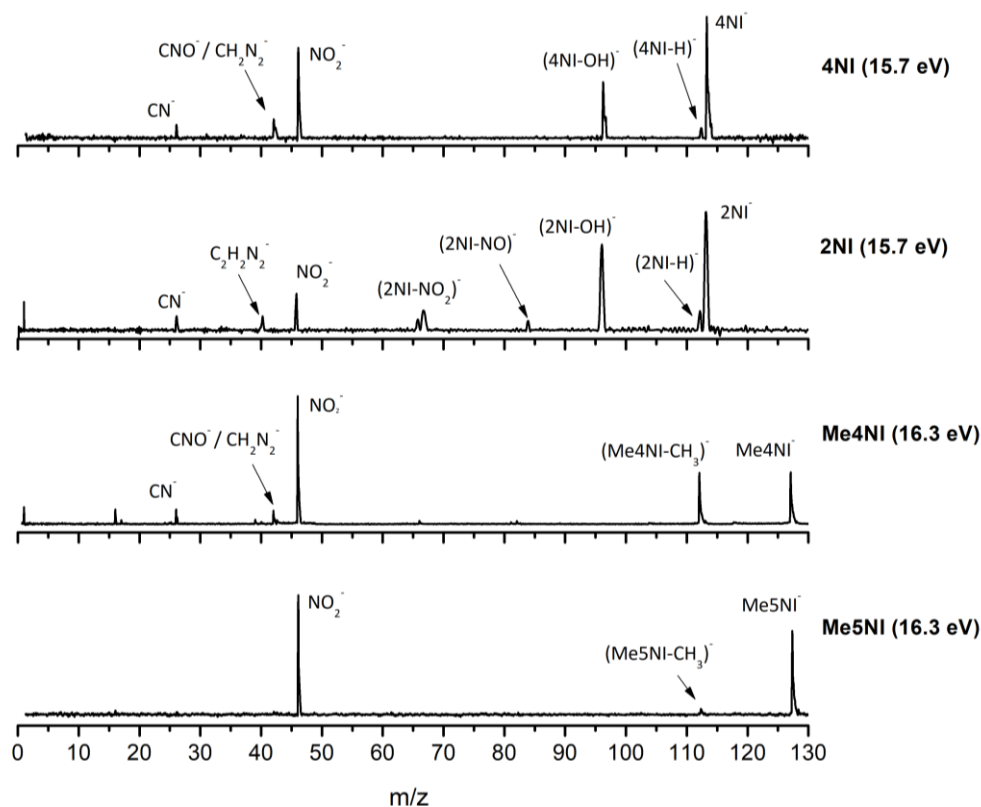


Figure 4.6. Time-of-flight negative ion mass spectra in potassium collisions with 4-nitroimidazole (4NI), 2-nitroimidazole (2NI), 1-methyl-4-nitroimidazole (Me4NI), 1-methyl-5-nitroimidazole (Me5NI) at 30eV lab frame energy (15.7 and 16.3 eV available energy in the centre-of-mass, respectively). See text for details.

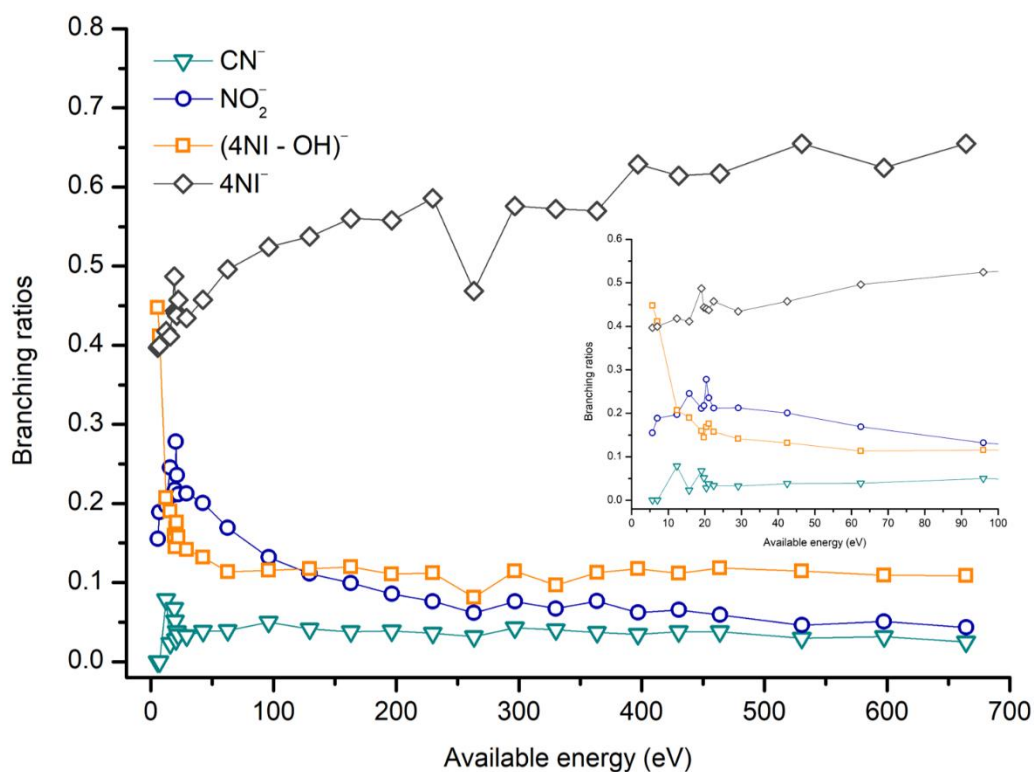


Figure 4.7. 4-nitroimidazole (4NI) branching ratios (fragment anion yield/total anion yield) of the main negative ions formed as a function of the collision energy in the centre-of-mass frame. See text for details.

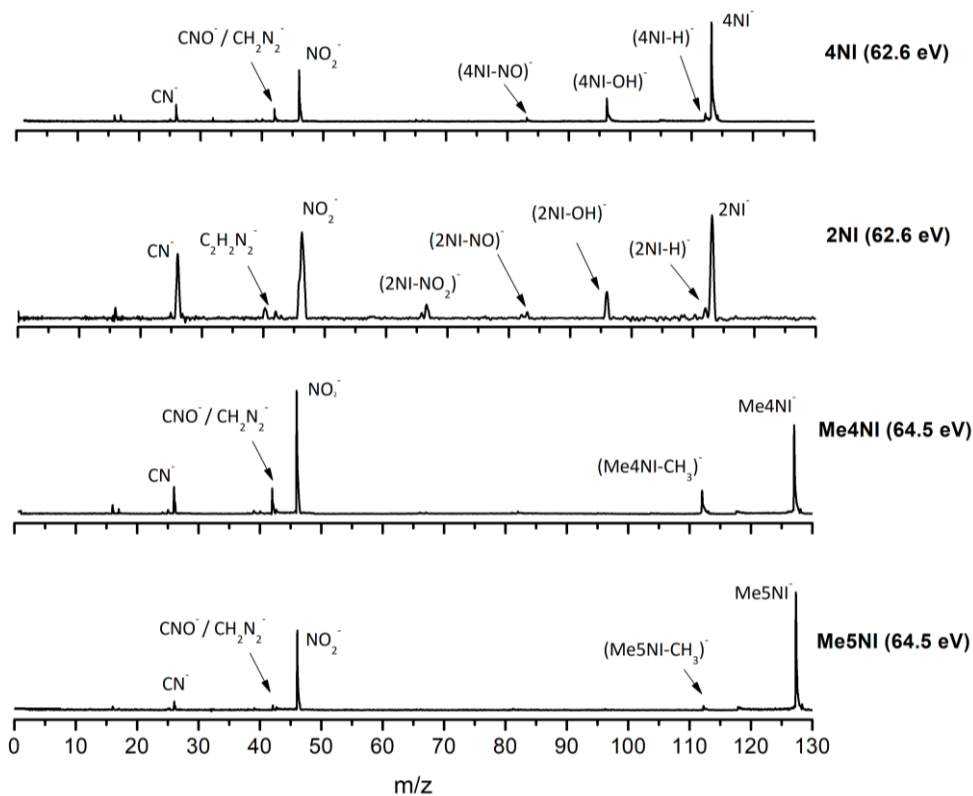


Figure 4.8. Time-of-flight negative ion mass spectra in potassium collisions with 4-nitroimidazole (4NI), 2-nitroimidazole (2NI), 1-methyl-4-nitroimidazole (Me4NI), 1-methyl-5-nitroimidazole (Me5NI) at 100 eV lab frame energy (62.6 and 64.5 eV available energy in the centre-of-mass, respectively). See text for details.

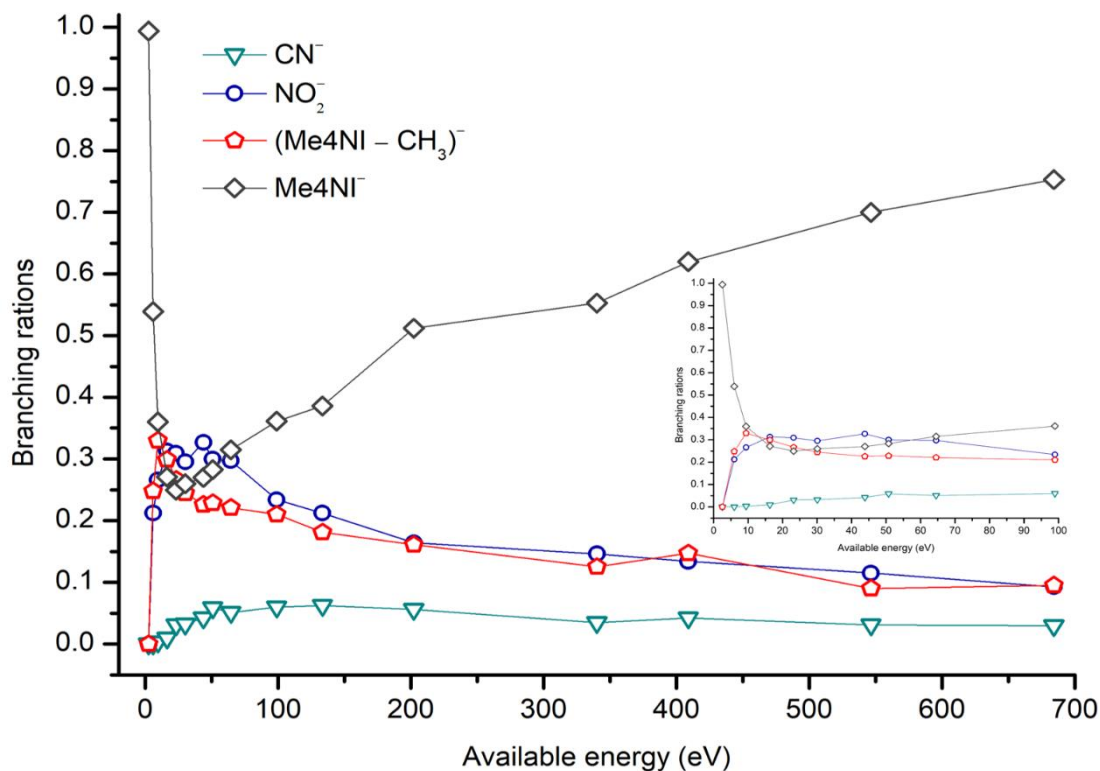


Figure 4.9. 1-methyl-4-nitroimidazole (Me4NI) branching ratios (fragment anion yield/total anion yield) of the main negative ions formed as a function of the collision energy in the centre-of-mass frame. See text for details.

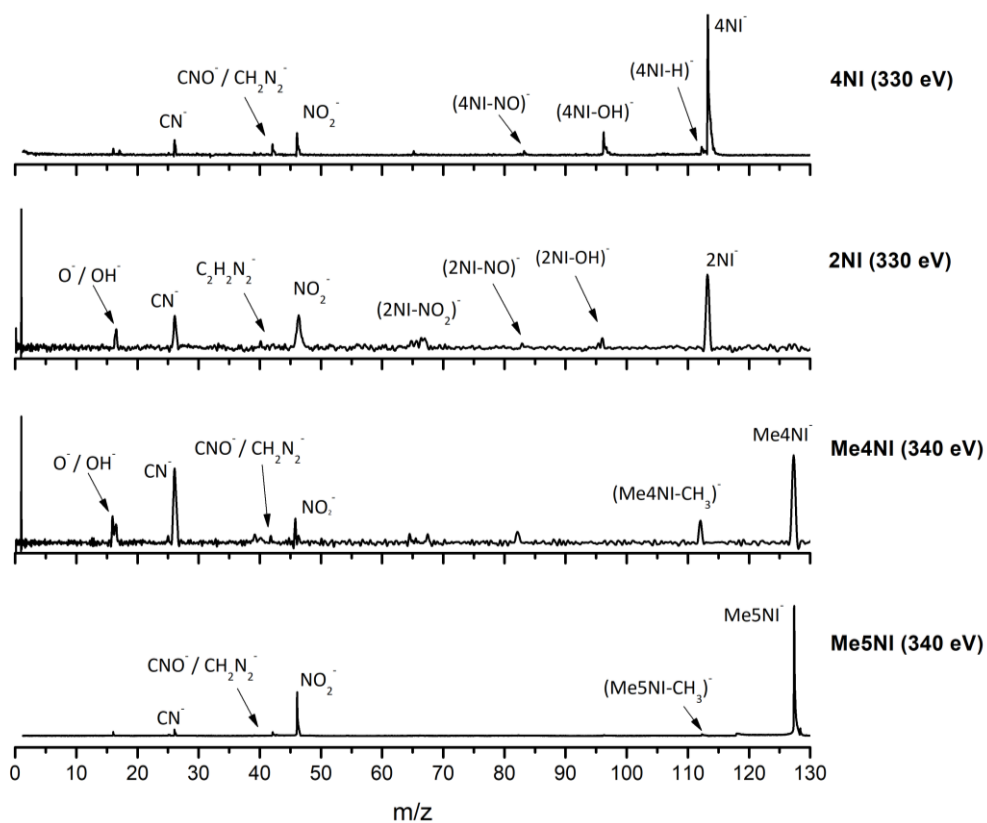


Figure 4.10. Time-of-flight negative ion mass spectra in potassium collisions with 4-nitroimidazole (4NI), 2-nitroimidazole (2NI), 1-methyl-4-nitroimidazole (Me4NI), 1-methyl-5-nitroimidazole (Me5NI) at 500 eV lab frame (330 and 340 eV available energy in the centre-of-mass, respectively). See text for details.

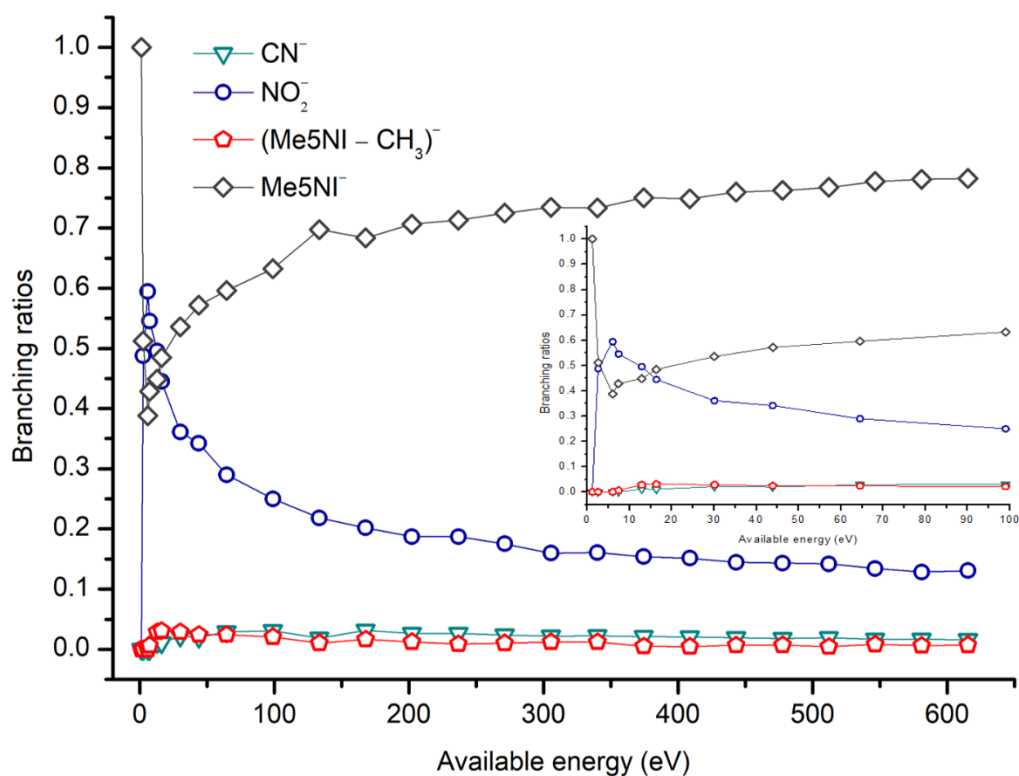
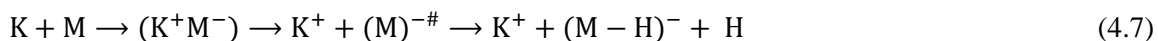


Figure 4.11. 1-methyl-5-nitroimidazole (Me5NI) branching ratios (fragment anion yield/total anion yield) of the main negative ions formed as a function of the collision energy in the centre-of-mass frame. See text for details.

## Imidazole molecule

### (IMI-H)<sup>-</sup> formation

The most intense anionic fragment observed in K–imidazole collisions over the energy range (15–1000 eV) is the dehydrogenated parent anion, (IMI-H)<sup>-</sup> (figures 4.12 and figure 4.13). The BRs show that the (IMI-H)<sup>-</sup> yield decreases from 5.4 eV (17 eV lab frame) to 52.8 eV (100 eV lab frame) where it reach a plateau contributing to ~ 40% of the total anion yield. In figure 4.8 is also discernible that the (IMI-H)<sup>-</sup> BR decreases with energy while other fragments as CN<sup>-</sup> and C<sub>2</sub>H<sub>2</sub>N<sup>-</sup> their BRs increase. This indicates that the hydrogenated parent anion seems to be a precursor in the formation of other anions. Such behaviour was already demonstrated in electron transfer collisions in neutral potassium with adenine [136], a molecule that generally speaking is a combination of a pyrimidine and an imidazole ring. Formation of (IMI-H)<sup>-</sup> can occur from the cleavage of an C–H or N–H bond, described as follows:



From the BRs (figure 4.13) the appearance threshold of (IMI-H)<sup>-</sup>, which is around 5.4 eV (17 eV lab frame). This is consistent with DEA measurements [156] showing two low-energy shape resonances at 1.52 eV and 2.29 eV leading to formation of this anion through dehydrogenation at the N<sub>1</sub> position. Two other resonances have been reported for higher energies (~7 and 11 eV) and assigned to core excited resonances. From table 4.3 we note that the loss of a neutral H can proceed through a coupling between a π\* resonance and a dissociative σ\* state localized at the N–H bond. Alternatively, a direct initial electron transfer to the σ\* state and consequent dissociation can take place, which may explain (IMI-H)<sup>-</sup> higher yields at higher collision energies. Cunha *et al.* [132] have shown in adenine and derivative molecules that the dehydrogenated parent anion is formed from the loss of an H atom from the N<sub>9</sub> site which corresponds to the N<sub>1</sub> position in the imidazole moiety.

### C<sub>2</sub>H<sub>2</sub>N<sup>-</sup> and CH<sup>-</sup> formation

Formation of C<sub>2</sub>H<sub>2</sub>N<sup>-</sup> may proceed from the loss of a HCN unit from the dehydrogenated parent anion, while CH<sup>-</sup> formation may result from the loss of another HCN unit from C<sub>2</sub>H<sub>2</sub>N<sup>-</sup>. Thus, the dehydrogenated parent anion seems to be a precursor of such reactions. Formation of such anions results from ring opening. The BR in figure 4.13 show that C<sub>2</sub>H<sub>2</sub>N<sup>-</sup> and CH<sup>-</sup> thresholds of formation are 10 eV (25 eV lab frame) 24.3 eV (50 eV lab frame), respectively. Another interesting aspect of the BR is that between 52.9 eV and 167.2 eV C<sub>2</sub>H<sub>2</sub>N<sup>-</sup> represents the second most intense anionic fragment, competing with CN<sup>-</sup>, especially at higher energies. In DEA experiments C<sub>2</sub>H<sub>2</sub>N<sup>-</sup> formation exhibits two resonances at 6.6 and 10.0 eV [156].

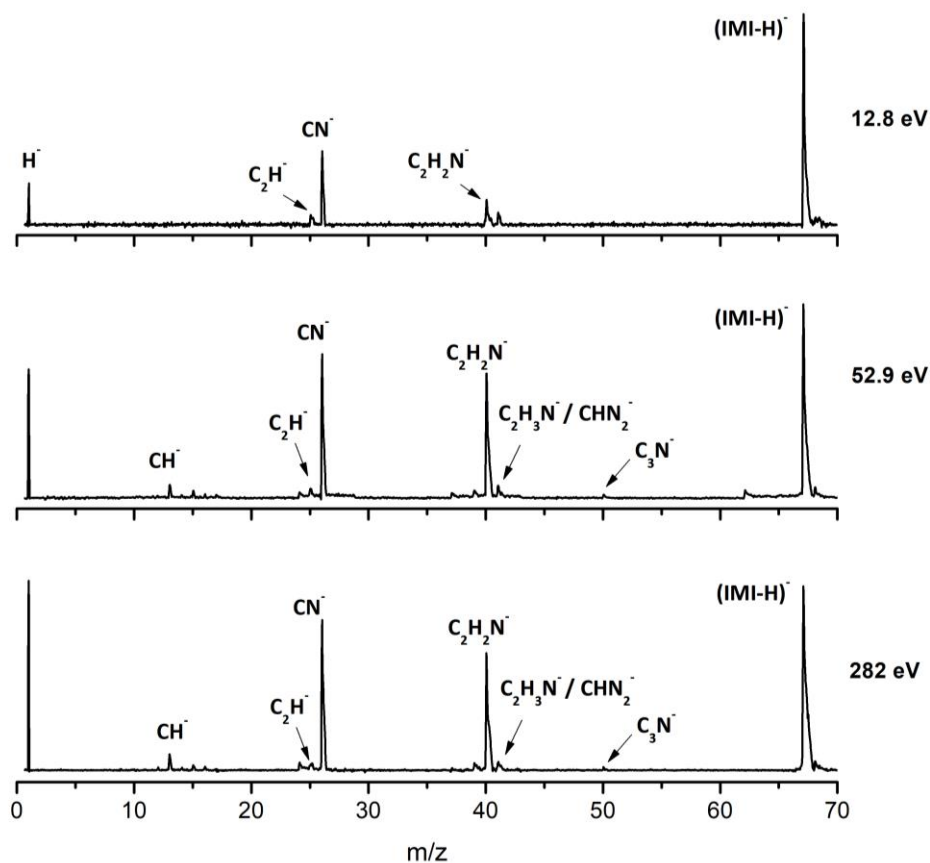


Figure 4.12. Time-of-flight negative ion mass spectra in potassium-imidazole (IMI) collisions at 30, 100 and 500 eV lab frame energy (12.8, 52.9 and 282 eV available energy in the centre-of-mass, respectively). See text for details.

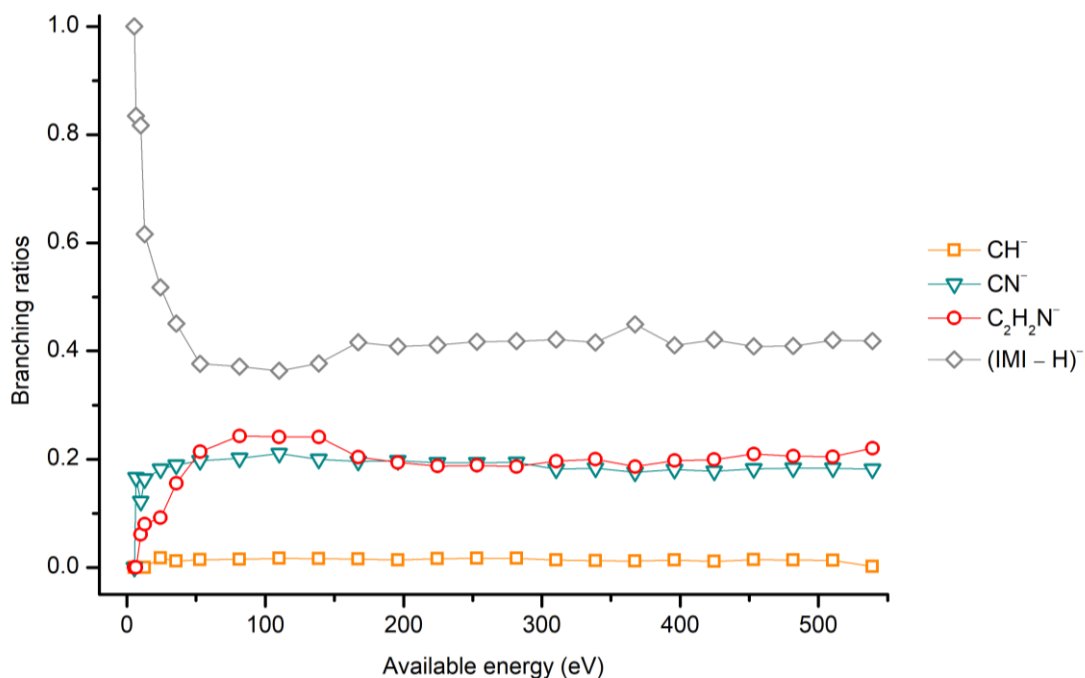


Figure 4.13. Imidazole (IMI) branching ratios (fragment anion yield/total anion yield) of the main negative ions formed as a function of the collision energy in the centre-of-mass frame. See text for details.



### CN<sup>-</sup> formation

The TOF mass spectra in figure 4.12 and the BRs in figure 4.13 show CN<sup>-</sup> as one of the most relevant negative ions formed in K–imidazole collisions. Indeed, it is the second most intense fragment between 6.5 and 35.7 eV (19 eV and 70 eV lab frame). For higher energies, especially for 167 eV (300 eV lab frame), we also observe a strong competition between CN<sup>-</sup> and C<sub>2</sub>H<sub>2</sub>N<sup>-</sup> formation. From figure 4.13 we observe that CN<sup>-</sup> threshold of formation is 6.5 eV (19 eV lab frame). Similarly to K–pyrimidine studies [161] and in contrast to adenine [136], uracil and thymine [75], in the case of imidazole the dehydrogenated parent anion is not a precursor in the formation of CN<sup>-</sup>.

### 4.2.5 Conclusions

The present work provides the first comprehensive investigation of the decomposition mechanisms of neutral nitroimidazoles and methylated compounds (4NI, 2NI, Me4NI, Me5NI and IMI) in electron transfer collisions with neutral potassium atoms. The major fragment anion channels have been investigated as a function of the available energy in the centre-of-mass frame. In the case of nitroimidazoles (4NI, 2NI and methylated molecules) the parent anion was identified as the most intense fragment over the entire energy range (10–1000 eV lab frame) investigated, as opposed to DEA studies, where the parent anion is only observed in the case of methylated molecules for very low energies (near 0 eV). Such difference may be explained considering the high dipole moment of these molecules and the presence of a third body (K<sup>+</sup>) in the collisional complex system (K<sup>+</sup> M<sup>-</sup>). Other important anionic species were assigned as part of the fragmentation pattern of nitroimidazoles, such as NO<sub>2</sub><sup>-</sup>, the loss of OH and NO. Some differences were also found between the 4NI and 2NI molecules, and between the methylated compounds, suggesting that the position of the nitro group may influence the fragmentation pattern. Additionally, the studies with imidazole show that the presence of a NO<sub>2</sub> group in the imidazole ring brings considerable modifications in the fragmentation pattern, as compared to the nitroimidazoles. In the imidazole molecule, the TOF mass spectra are dominated by the dehydrogenated parent anion, CN<sup>-</sup> and C<sub>2</sub>H<sub>2</sub>N<sup>-</sup>. We have also observed that the dehydrogenated parent anion seems to be a precursor in the formation of other fragment anions. The decomposition channels presented here upon electron transfer showing formation of parent anion and other radicals even at higher energies, demonstrate the capability of these nitroimidazole compounds to act as radiosensitisers in treatments using radiation. Some differences found between nitroimidazole molecules and related methylated compounds as well as the differences observed in imidazole molecules (which is basically a replacement of the nitro group by an H atom) demonstrate the importance of these studies in understanding the underlying molecular mechanisms that govern such electron induced decomposition which can be used to formulate new radiopharmaceutical compounds or new methodologies to make these chemical compounds more attuned to key specific reaction.

### 4.3 Ion-Pair Formation in Neutral Potassium-Neutral Pyrimidine Collisions: Electron Transfer Experiments<sup>3</sup>

#### Abstract

We report novel data on ion-pair formation in hyperthermal (30–800 eV) neutral potassium collisions with neutral pyrimidine (Pyr, C<sub>4</sub>H<sub>4</sub>N<sub>2</sub>) molecules. In this collision regime, negative ions formed by electron transfer from the alkali atom to the target molecule were time-of-flight mass analysed and the fragmentation patterns and branching ratios have been obtained. The most abundant product anions have been assigned to CN<sup>-</sup> and C<sub>2</sub>H<sup>-</sup> and the electron transfer mechanisms are comprehensively discussed. Particular importance is also given to the efficient loss of integrity of the pyrimidine ring in the presence of an extra electron, which is in contrast to dissociative electron attachment experiments yielding the dehydrogenated parent anion. Theoretical calculations were performed for pyrimidine in the presence of a potassium atom and provided a strong basis for the assignment of the lowest unoccupied molecular orbitals accessed in the collision process. In order to further our knowledge about the collision dynamics, potassium cation (K<sup>+</sup>) energy loss spectrum has been obtained and within this context, we also discuss the role of the accessible electronic states. A vertical electron affinity of (-5.69±0.20) eV was obtained and may be assigned to a  $\pi_3^*(b_1)$  state that leads to CN<sup>-</sup> formation.

---

<sup>3</sup> This chapter is based on the following submitted publication: M. Mendes, B. Pamplona, S. Kumar, F. Ferreira da Silva, A. Aguilar, G. García, M.-C. Bacchus-Montabonel, P. Limão-Vieira. Ion-pair formation in neutral potassium-neutral pyrimidine collisions: electron transfer experiments (2019).

### 4.3.1 Introduction

Radiation induced damage by low-energy electrons (<15 eV) has proven to be an efficient mechanism to promote local chemical changes when attaching to DNA/RNA molecular constituents [37]. In such electron attachment process as a function of the phase and stage of aggregation, formation of a transient negative ion (TNI) can subsequently dissociate into stable fragment anions and neutral radical species [60], where the latter may also trigger complex chemical damage within the biological environment. Another interesting aspect of such electron induced bond breaking pertains to the role of electron transfer processes which may be more prevalent under physiological conditions rather than free electron attachment processes [166]. As far as electron induced processes are concerned, pyrimidine (Pyr) has been extensively studied as a prototype molecule of DNA and RNA building blocks (thymine, cytosine, and uracil) both in the gas [52] and condensed phases [167,168]. Electron interactions with pyrimidine nucleobases are well represented in the literature, where we note relevant experimental studies on electron transmission spectroscopy [169], DEA experiments [170,171], and electron impact ionisation studies [172]. More recently, site-selective bond excision of selected pyrimidines yielding the dehydrogenated parent anion upon electron transfer in collisions with neutral potassium atoms [173] and with low-energy electrons [174] have been reported. N-site de-methylation in pyrimidine bases as studied by low-energy electrons and ab initio calculations gave a comprehensive description into the dynamics of the decaying transient anion and more precisely into the competition between dissociation and auto-detachment [71]. Potassium-uracil/thymine ring cleavage enhancement was reported in electron transfer experiments and theoretical calculations [131]. Studies on threshold behaviour in metastable dissociation of multi-photon ionized thymine and uracil [175] have been also investigated.

The topic of this contribution deals with electron transfer experiments with Pyr ( $C_4H_4N_2$ ) and within this context, a literature survey reveals that Nenner and Schulz experimental electron transmission spectroscopy data report the three shape resonances at 0.25 ( $\tilde{X}^2A_2$ ), 0.77 ( $\tilde{A}^2B_1$ ) and 4.24 ( $\tilde{B}^2B_1$ ) eV [176] while Modelli and Burrow [177], and more recently Modelli et al. [178], placed the three lowest electron affinities of  $\pi^*$  character at 0.39 [ $\pi_1^*(a_2)$ ], 0.82 [ $\pi_2^*(b_1)$ ] and 4.26 [ $\pi_1^*(b_1)$ ] eV and a core-excited resonance at 5.5 eV. An unprecedented investigation on the effect of solvation on electron attachment to pure and hydrated Pyr clusters, has shown that hydration quenches all fragmentation channels in the pyrimidine molecule [31]. Regarding theoretical calculations, we note a detailed study of the effect of the third  $\pi^*$  resonance on the angular distributions for electron-pyrimidine scattering [179] and electron affinities and ionisation potentials of DNA radical ions [180]. Total electron-scattering cross-sections have been thoroughly investigated in several occasions [181,182] together with differential cross-sections for low-energy electron-impact excitation [183–185]. Theoretical elastic and electronic excitation cross-sections and experimental electronic excitation cross-sections for electron collisions with pyrimidine have been reported by

Masin and co-workers [186]. Additionally, fragmentation of pyrimidine induced by core ionisation by photoelectron-photoion-photoion coincidence (PEPIPICO) spectroscopy [187] and the absolute total and partial dissociative cross-sections of pyrimidine at electron and proton intermediate impact velocities [188] have been probed. The electronic state spectroscopy of pyrimidine has been comprehensively investigated by different methods, with threshold-electron excitation reported up to 12.5 eV [189], absolute cross-sections for electronic excitation have been obtained by electron impact up to 18 eV [190] and absolute cross-sections by high-resolution VUV photoabsorption up to 11 eV [191]. Low-energy (2–12 eV) electron vibrational and electronic electron-energy-loss [192] and electron stimulated desorption from condensed pyrimidine [46,168] have also been reported. Finally, a comparative study on the role of pyrimidine and water as underlying molecular constituents for describing radiation damage in living tissue, in terms of energy deposition (absorbed dose and stopping power) but also in terms of the number of induced molecular processes [193] has been reported. Thus we consider that the present data on collisional electron-transfer induced dissociation of pyrimidine may serve for future applications in nanoscale models of radiation damage in DNA/RNA as we have recently proposed for the purines [132,136] and other biological relevant molecules as uridine [74] and small amino acids [194] just to mention a few.

In this manuscript we therefore report for the first time negative ion formation in neutral potassium-neutral pyrimidine collisions, together with  $K^+$  energy loss data and novel ab initio calculations to support the experimental findings. In the next sections, we describe our experimental methods and theoretical methodology. Afterwards, our results are presented and discussed and conclusions from this work are finally summarised.

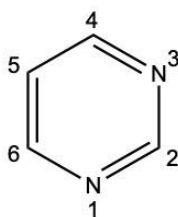


Figure 4.14. Molecular structure of pyrimidine (Pyr).

### 4.3.2 Experimental Methods

The crossed molecular beam setup used to study collisions of neutral potassium (K) atoms with neutral pyrimidine (Pyr), has been described in detail in Section 3.1. Briefly, an effusive target molecular beam crosses a primary beam of fast neutral K atoms and the product anions are analysed using a reflectron time-of-flight (TOF) mass spectrometer (KORE R-500-6). The K beam is produced in a resonant charge exchange chamber from the interaction of  $K^+$  ions from a potassium ion source (30–800 eV in the lab frame) with gas-phase neutral potassium atoms from an oven source. Residual ions were removed from the primary beam by electrostatic deflecting plates outside the oven. The

neutral potassium beam's intensity was monitored using a Langmuir–Taylor ionisation detector before and after the collection of each TOF mass spectrum and the beam energy resolution in the collision energy range as measured as  $\sim 0.5$  eV (FWHM) using a hemispherical electrostatic energy loss analyser to characterise the  $K^+$  ion signal at a fixed energy, following K collisions with nitromethane ( $CH_3NO_2$ ). The effusive beam of pyrimidine from an oven source was admitted into vacuum through a 1 mm diameter capillary where it was crossed with the neutral fast potassium beam. Negative ions formed in the collision region were extracted by a  $\sim 380$  V  $cm^{-1}$  pulsed electrostatic field. The typical base pressure in the collision chamber was  $6 \times 10^{-5}$  Pa and the working pressure was  $4 \times 10^{-4}$  Pa. Mass spectra (resolution  $m/\Delta m \approx 800$ ) were obtained by subtracting background measurements (without the sample) from the sample measurements. Mass calibration was carried out on the basis of the well-known anionic species formed after potassium collisions with nitromethane [66]. Pyrimidine (Pyr) was supplied by Sigma Aldrich with a stated purity of  $\geq 98\%$ . Repeated freeze-pump-thaw cycles were performed before each spectrum collection. The extraction region and the TOF system were heated during the measurements in order to prevent any sample condensation and thus charge accumulation on the electrodes.

The entrance slit of the hemispherical energy analyser used in the  $K^+$  energy loss measurements is aligned in the forward direction with the neutral K beam's optical path. The analyser was operated in constant transmission mode, hence keeping the resolution constant throughout the entire scan where the energy resolution for the present measurements was  $\sim 0.6$  eV in the lab frame. The energy loss scale was calibrated using the experimental threshold energy of formation of  $4.5$  eV from  $CN^-$  since it is the most intense fragment anion formed in K-Pyr collisions.

### 4.3.3 Theoretical Method

The theoretical description of the charge transfer process in the interaction of a neutral potassium atom with a selected nucleobase, is based on the evolution of the quasi-molecular system formed by the potassium projectile and the molecular target along the reaction coordinate within the framework of the molecular representation. We have implemented with success the one-dimension coordinate approximation in previous ion/neutral-biomolecule collision systems [131,195,196], where the atom-nucleobase collision system is thus treated as a pseudo-diatomic molecule evolving along the coordinate associated with the distance between the impinging atom and the nucleobase [197,198]. Within the frame of such approximation, we do not consider the internal degrees of freedom of the biomolecular target, which is reasonable since in very fast collision processes where nuclear vibration and rotation motions are much slower than the collision time, these can be considered frozen during the collision. The geometry of pyrimidine has been optimized at the MP2 level of theory from the work of [199]. A perpendicular approach of the potassium atom, pointing at the centre of the pyrimidine ring (see figure 4.14) has been considered, as the charge transfer process has been clearly shown to be favoured in such orientation for the case of pyrimidine targets [200,201].

Ab-initio molecular calculations have been performed with the MOLPRO code [202], where the pyrimidine target is kept frozen in its ground state geometry during the collision process. The calculation has been performed in Cartesian coordinates, with no symmetries. All electrons have been considered for C, N and H atoms with the VTZ basis set, although the 18 core electrons of potassium have been treated through the ECP18sdf core-electron pseudopotential [203], with the corresponding basis set. The natural molecular orbitals for K–Pyr have been determined by CAS(3,11) state-averaged CASSCF calculations for the reaction coordinate  $R = 10 \text{ \AA}$  corresponding to the asymptotic region. The 1s orbitals of carbon, nitrogen and oxygen are treated as frozen cores. The resultant lowest unoccupied molecular orbitals (LUMOs) for pyrimidine are shown in figure 4.4 together with the corresponding orbitals without the presence of potassium. The polarization by the potassium atom induces a global shift in energy of  $\sim 1.5\text{--}2.0 \text{ eV}$  for the  $\pi^*$  orbitals and  $2.0 \text{ eV}$  for the  $\sigma^*$  orbital.

#### 4.3.4 Results and Discussion

This is the first investigation on negative ion formation in electron transfer from neutral K atoms with Pyr combining experimental and theoretical methods to comprehensively analyse the full fragmentation pattern. Dissociative electron transfer TOF mass spectra were recorded at lab-frame collision energies of  $30\text{--}800 \text{ eV}$  ( $\sim 14\text{--}480 \text{ eV}$  in the centre-of-mass frame and from now on referred as available energy). Table 4.5 is a compilation of all fragment anions detected and their proposed assignments in the wide energy range of collisions investigated. Figure 4.15 shows the Pyr negative ions TOF mass spectra recorded at  $30, 100$  and  $700 \text{ eV}$  lab frame energy ( $13.8, 56.2$  and  $419.3 \text{ eV}$  available energy), while in figure 4.16 we present the  $\text{K}^+$  energy loss spectrum measured in the forward direction in collisions of potassium atoms with pyrimidine at  $111 \text{ eV}$  lab frame energy ( $67.2 \text{ eV}$  available energy). Branching ratios (BRs) for the major fragments of Pyr as a function of the collision energy are presented in figure 4.17.

A careful inspection of the TOF mass spectra reveals that they are dominated by the cyanide anion ( $\text{CN}^-$ ) and show no evidence of parent anion formation ( $\text{Pyr}^-$ ), which is expected since the vertical electron affinity of pyrimidine lies between  $-0.39$  and  $-0.54 \text{ eV}$  [176,178]. Another interesting aspect of the collision induced fragmentation pertains to the loss of different HCN units from the dehydrogenated parent anion of Pyr,  $(\text{Pyr-H})^-$ , yielding  $\text{C}_3\text{H}_2\text{N}^-$  (and/or the isobaric species  $\text{C}_2\text{N}_2^-$ ) and  $\text{C}_2\text{H}^-$  (table 4.5), with such mechanism also reported in the case of potassium-adenine electron transfer experiments [132,136]. The presence of the  $\text{K}^+$  ion in the vicinity of the TNI formed upon  $\text{K} + \text{Pyr} \rightarrow (\text{K}^+ \text{Pyr}^-)$  plays a significant role in the decomposition mechanism yielding particular fragmentation channels, which are different from those observed in DEA experiments [31]. Such strong coulomb interaction in the collision complex ( $\text{K}^+ \text{Pyr}^-$ ) may delay autodetachment allowing time enough, in particular in the low-collision regime, for the excess energy in the TNI to be redistributed through the different available degrees of freedom enhancing a favourable

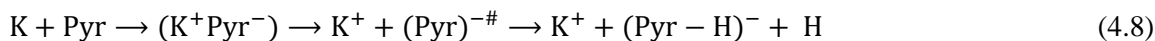
fragmentation channel. In Pyr the fragmentation predominantly results in  $\text{CN}^-$  formation which is not surprisingly given its high electron affinity ( $3.8620 \pm 0.0050$ ) eV [165]. The ab initio calculations in table 4.4 show that the lowest-lying  $\pi^*$  states are considerably shifted to higher energies in the presence of a potassium atom in comparison to respective calculated MOs without the presence of K. During the electron transfer process, an electronic transition accessing a  $\pi^*$  state does not lead to direct cleavage of a bond unless a repulsive  $\sigma^*$  state is crossed diabatically. In the present experiments the available energy is larger than the threshold for electron transfer ( $\Delta E = \text{IE}(\text{K}) - \text{EA}(\text{Pyr}) = 4.34 + 0.39 = 4.73$  eV), with  $\text{IE}(\text{K})$  the ionisation energy of the potassium atom and  $\text{EA}(\text{Pyr})$  the Pyr electron affinity), and if the lifetime of the metastable ion is long enough, intramolecular energy redistribution may occur competing with direct dissociation. Such is possible if the nuclear wavepacket survives long enough along the reaction coordinate to allow diabatic coupling between the two states, i.e.  $\pi^*$  and  $\sigma^*$ . This is discussed in the next sections within the scope of the different  $\pi^*$  and  $\sigma^*$  MOs involved in the formation of specific fragment anions.

### **K<sup>+</sup> energy loss spectrum**

The energy loss spectrum of  $\text{K}^+$  ions formed in the forward direction from the collision of potassium atoms with pyrimidine at 111 eV lab frame energy, is shown in figure 4.16. Note that the lowest energy loss scale appears above  $\sim 4$  eV to account for the potassium ionisation energy, 4.34 eV. Two features are visible at 10.03 and 11.91 eV, the former more intense than the latter and with a full width at half-maximum (FWHM) of  $\sim 1.2$  eV. The position of the maxima does not shift with the collision energy within  $\pm 0.2$  eV. The main anionic yield from the TOF mass spectra at all collision energies is due to  $\text{CN}^-$  (figures 4.15 and 4.17). The energy loss  $\Delta E$  at the maximum of the features is given by  $\Delta E = \text{IE}(\text{K}) - \text{EA}_{\text{max}}$ , which results on an electron affinity of  $(-5.69 \pm 0.20)$  eV and  $(-7.57 \pm 0.20)$  eV, assigned to  $\pi_3^*(b_1)$  and a  $\pi_{CH}^*$  core-excited resonance, respectively. This is in good agreement with the theoretical calculations presented in table 4.4.

### **(Pyr-H)<sup>-</sup>**

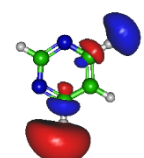
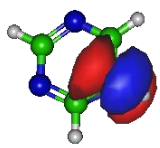
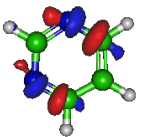
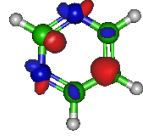
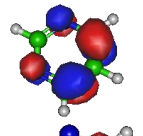
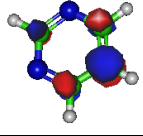
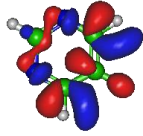
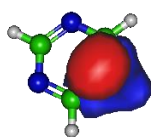
The dehydrogenated closed shell anion  $(\text{Pyr-H})^-$  is formed through the ion-pair reaction:



which represents a direct cleavage of the (C-H) bonds and  $(\text{Pyr})^{-\#}$  stems for a TNI formed with an excess of internal energy. Formation of the parent anion with H abstraction has been reported in DEA experiments on pyrimidine through a core-excited resonance at 5.5 eV [31], where the three lowest  $\pi^*$  resonances do not contribute to such anion formation due to their short-lived character. Moreover, recent R-matrix calculations [186] predict higher excited states which may contribute to  $(\text{Pyr-H})^-$  formation. Pyrimidine BR as a function of the available energy (figure 4.17), shows that  $(\text{Pyr-H})^-$

yield only accounts for 10-20 % of the total anions in the 50–480 eV energy region, and vanishes below the threshold of formation at ~26 eV. Such low anion yield in respect to the other fragment anions is in sharp contrast to the experimental observations in the low-energy collision regime of potassium atoms with DNA/RNA pyrimidines, thymine and uracil [170,173]. Such is certainly due to the different sort of molecular bonding where the presence of N–H bonds (in contrast to the C–H bond) lowers the threshold of the de-hydrogenated parent anion formation, which does not prevail in the case of pyrimidine.

Table 4.4. Calculated lowest unoccupied molecular orbitals (LUMOs) for pyrimidine (Pyr) and pyrimidine (Pyr) in the presence of a potassium atom in the perpendicular geometry inside the pyrimidine ring. Energies in eV.

	pyrimidine	K + pyrimidine
LUMOs	$\sigma^*_{CH}$ 1.8 eV 	$\sigma^*_{CH}$ 9.4 eV 
	$\sigma^*_{CN}$ 7.6 eV 	
	$\pi^*_{ring}$ 3.9 eV 	$\pi^*_{ring}$ 5.0 eV 
		$\pi^*_{ring}$ 6.6 eV 
	$\pi^*_{CH}$ 5.9 eV 	$\pi^*_{CH}$ 8.0 eV 

In table 4.4 we show the three lowest calculated  $\pi^*$  MOs at 5.0 eV ( $\pi^*_{ring}$ ), 6.6 eV ( $\pi^*_{ring}$ ) and 8.0 eV ( $\pi^*_{CH}$ ) and at higher energy a  $\sigma^*$  resonance at 9.4 eV ( $\sigma^*_{CH}$ ) along the C<sub>5</sub>–H bond. Pyrimidine BRs in figure 4.17 shows that (Pyr–H)<sup>−</sup> cannot be produced < 25 eV which can be related to an electron promotion to the  $\pi^*_{ring}$  orbitals yielding instead CN<sup>−</sup>. Accessing a  $\pi^*_{CH}$  state may be only possible by increasing the collision energy, and so (Pyr–H)<sup>−</sup> formation certainly occurs through access of the  $\sigma^*_{CH}$  state via curve crossing. The present energy loss data provides evidence that the feature at 11.91 eV, 7.57 eV for the electron affinity, (see figure 4.16) is indicative of the vertical transition energy to the  $\pi^*_{CH}$  state, and the closeness with the  $\sigma^*_{CH}$  state allows us to specify the dominant pathway to dissociation. Alternatively, a direct initial transfer to the  $\sigma^*$  state and subsequent dissociation may be



considered, playing a relevant role in the higher-energy collision region where the  $(\text{Pyr-H})^-$  yield predominates in respect to the fragment anions produced through the  $\pi_{ring}^*/\pi_{CH}^*$  resonances. Interesting to note the resonances that are prominent in the excitation functions for vibrational excitation, and peaking at  $\sim 10$  eV, have been assigned to  $\sigma^*$  with pronounced C–H stretching character although ring breathing modes may be present [190].

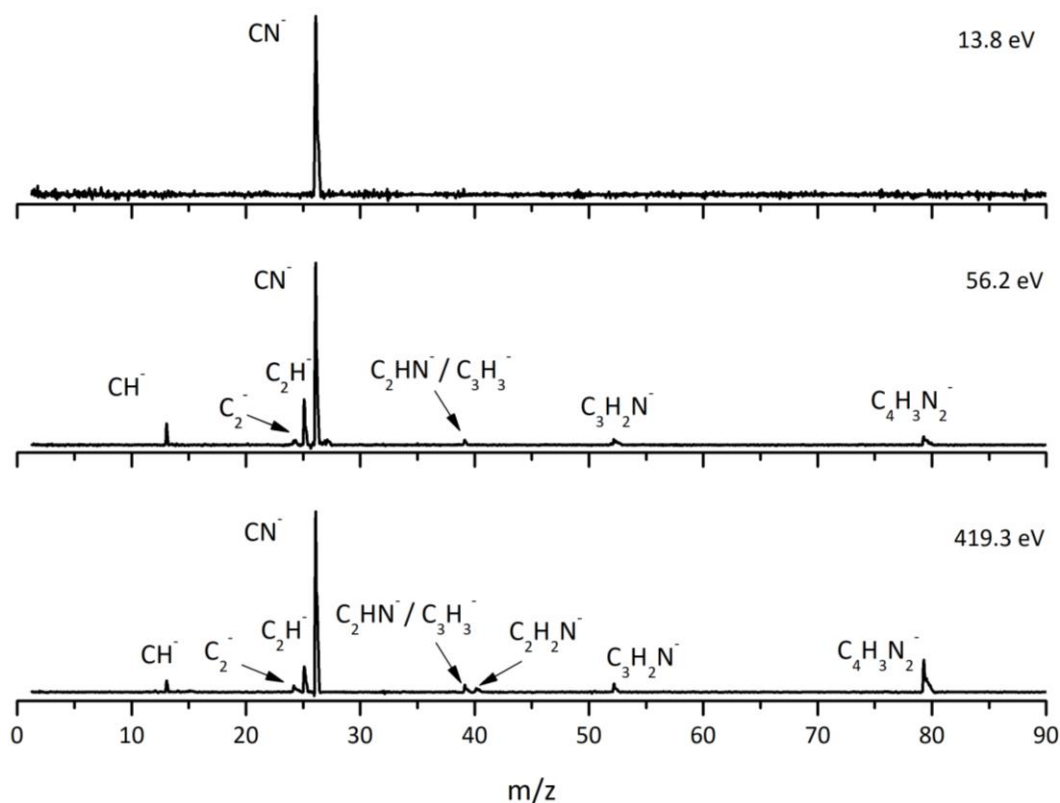


Figure 4.15. Time-of-flight negative ion mass spectra in potassium-pyrimidine (Pyr) collisions at 30, 100 and 700 eV lab frame energy (13.8, 56.2 and 419.3 eV available energy in the centre-of-mass, respectively). See text for details.

### $\text{C}_3\text{H}_2\text{N}^-/\text{C}_2\text{N}_2^-$ , $\text{C}_2\text{H}^-$

Hydrogen cyanide abstraction is operative from the de-hydrogenated parent anion leading to pyrimidine ring opening, with assignment of the fragment anions indicated in table 4.5. Formation of  $\text{C}_3\text{H}_2\text{N}^-$  (and/or the isobaric  $\text{C}_2\text{N}_2^-$ ) from potassium collisions with pyrimidine occurs at threshold  $> 38$  eV while for  $\text{C}_2\text{H}^-$  above 14 eV in the centre-of-mass frame (see 4.17), the latter the second most intense fragment anion up to 250 eV. However, owing to  $\text{C}_2\text{H}$  electron affinity,  $(2.969 \pm 0.006)$  eV [204] in contrast with  $-0.27$  eV for  $\text{C}_3\text{H}_2\text{N}$  adiabatic electron affinity (from our present VTZ basis/CASSCF calculation), the former anion may prevail in the electron transfer induced decomposition of the pyrimidine molecule. We also observe a strong competition between  $\text{C}_2\text{H}^-$  and  $(\text{Pyr-H})^-$  formation which is enhanced above 250 eV. The LUMOs of Pyr in table 4.4 show relevant  $\pi^*$  antibonding character with nodes along the C–N bonds. Such electron spin densities are indicative

of favourable bond breaking in particular where curve crossing in the diabatically frame description may be relevant (i.e.  $\pi_{CH}^*/\sigma_{CH}^*$ ). However, at low collision energies ( $\leq 26$  eV), the de-hydrogenated parent anion channel is not operative but is  $C_2H^-$  although with modest intensity. The dominant  $K^+$  energy loss features peaks at 10.03 eV (figure 4.16), 5.69 eV for the electron affinity and lends support to the electron spin densities suggesting that the electron may be initially transferred to the  $\pi_{ring}^*$  states. This  $(Pyr-H)^-$  suppression can be rationalised in terms of a slow collision process ( $> 46$  fs) enhancing a coulombic stabilization of the TNI by the proximate  $K^+$  ion, increasing the probability of intramolecular electron transfer that may favour dissociation or may favour autodetachment (supressing dissociation), certainly explaining the low yields observed in this energy region. As far as authors are aware, no DEA experiments to pyrimidine have been produced these fragment anions. Within the collision energy range studied for pyrimidine, i.e. for the available energy (14–480 eV), such loss of HCN units is operative since the estimated threshold of the decomposition reaction requires  $-0.89$  eV given that  $\Delta_f H_g^\circ (C_4H_4N_2) = 196.65$  kJ/mol (2.04 eV) [205],  $\Delta_f H_g^\circ (C_3H_2N) = -242$  kJ/mol ( $-2.51$  eV) [206], EA ( $C_3H_2N$ ) =  $-26.05$  kJ/mol ( $-0.27$  eV, from our present VTZ basis/CASSCF calculation),  $\Delta_f H_g^\circ (HCN) = 135.14$  kJ/mol (1.4 eV) and  $\Delta_f H_g^\circ (H) = 218$  kJ/mol (2.26 eV) [165].

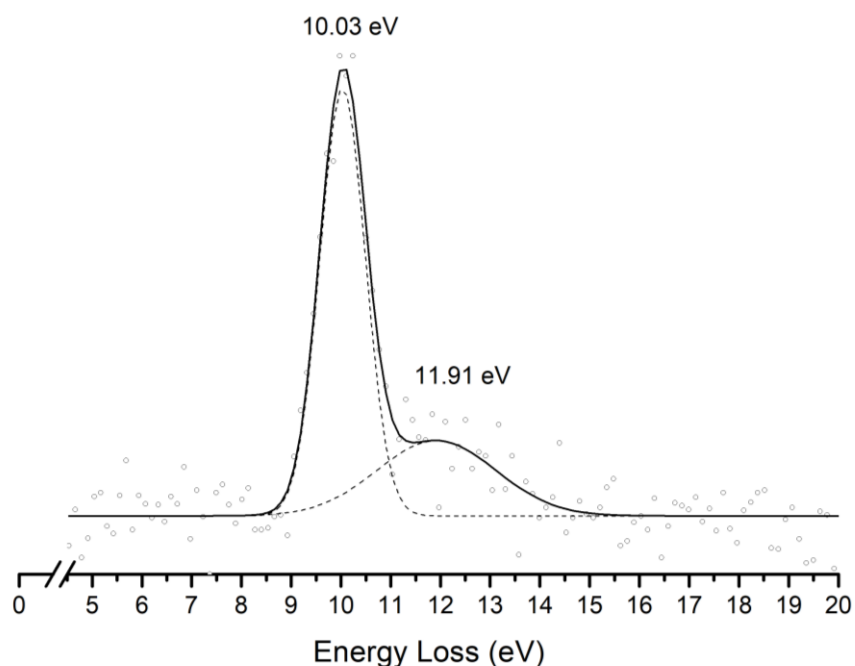


Figure 4.16. Energy loss spectrum of  $K^+$  ions measured in the forward direction in collisions of potassium atoms with pyrimidine (Pyr) at 111 eV lab frame energy (67.2 eV in the centre-of-mass system). See text for details.

**CN<sup>-</sup>**

The TOF mass spectra in figure 4.15 and the BRs in figure 4.17 are dominated by the cyanide anion in all collision energy range investigated. In sharp contrast to uracil and thymine collisional electron transfer experiments where the unimolecular decomposition process proceeds through the dehydrogenated parent anion as a precursor in the formation of fragments that require bond cleavages in the ring, namely CN<sup>-</sup> [170], that is not the case in pyrimidine. DEA experiments on pyrimidine report CN<sup>-</sup> formation via two broad resonances at 5.5 and 9.0 eV [31]. In order to aid our understanding of the underlying molecular mechanisms and the accessed states that are responsible for CN<sup>-</sup> formation in K-Pyr collisions, table 4.4 shows the three low-lying calculated  $\pi^*$  orbitals at 5.0, 6.6 eV and 8.0 eV. At higher energy a  $\sigma^*$  resonances at 9.4 eV is present with antibonding character along the C5-H bond. We now turn again our attention to the energy loss data in figure 4.16 where the features have been assigned to transitions to electronic states through  $\pi_{ring}^*$  ( $\pi_3^*(b_1)$ ) and a  $\pi_{CH}^*$  core-excited resonances at 5.69 and 7.57 eV, respectively. In the collision energy range investigated, CN<sup>-</sup> is the major fragment anion and is mainly formed through an electron promotion to the  $\pi_{ring}^*$  orbitals. Such finding lends support to the theoretical prediction of the  $\pi_{ring}^*$  orbitals at 5.0 and 6.6 eV. Accessing the different  $\pi^*$  orbitals is achieved by increasing the collision energy and efficient bond breaking should proceed through access of  $\sigma^*$  states. However, the present calculations for K-Pyr do not predict any  $\sigma_{CN}^*$  states close in energy to the  $\pi_{ring}^*$  orbitals since these were performed without the presence of the K<sup>+</sup> ion post-collision. From table 4.4 and in the case of the MOs for pyrimidine (left column), the  $\sigma_{CN}^*$  state shows strong antibonding character between C<sub>6</sub>-N<sub>1</sub> and C<sub>4</sub>-N<sub>3</sub> bonds. Owing to the similarity in the calculated electron spin densities between Pyr and K+Pyr in table 4.4, and apart from the differences in energies, we can anticipate a similar character for the C-N bonds. Notwithstanding, the proposed mechanism as suggested before in the case of the pyrimidines thymine and uracil [75,131], accounts for the initial access to one of the  $\pi^*$  states and subsequent intramolecular electron transfer into one of the highly antibonding  $\sigma^*$  states enhancing an effective ring-breaking pathway. Such is achieved in electron transfer studies since the presence of the K<sup>+</sup> ion in the vicinity of the TNI may suppress autodetachment long enough for the fragmentation pathway successful competition [75,131].

**4.3.5 Conclusions**

The present work provides the first comprehensive investigation of the decomposition mechanisms of neutral Pyr in collisions with neutral potassium atoms yielding ion-pair formation. The major negative ions formed have been investigated as a function of the available energy in the centre-of-mass frame, and assigned to the cyanide anion, the de-hydrogenated parent anion, and fragment anions related to the pyrimidine ring opening due to abstraction of HCN units from (Pyr-H)<sup>-</sup>. The theoretical calculations reveal detailed information about the electronic structure of K+Pyr and hence

provide insight into the electronic states that are most likely participate in the major fragment anion channels. We have also shown that ion-pair formation in collisions of potassium atoms with pyrimidine molecules, yields two different electronic states of the metastable parent anion. These states have vertical electron affinities of  $(-5.69 \pm 0.20)$  and  $(-7.57 \pm 0.20)$  eV, assigned to  $\pi_3^*(b_1)$  and a  $\pi_{CH}^*$  states, the latter accessible through a core-excited resonance.

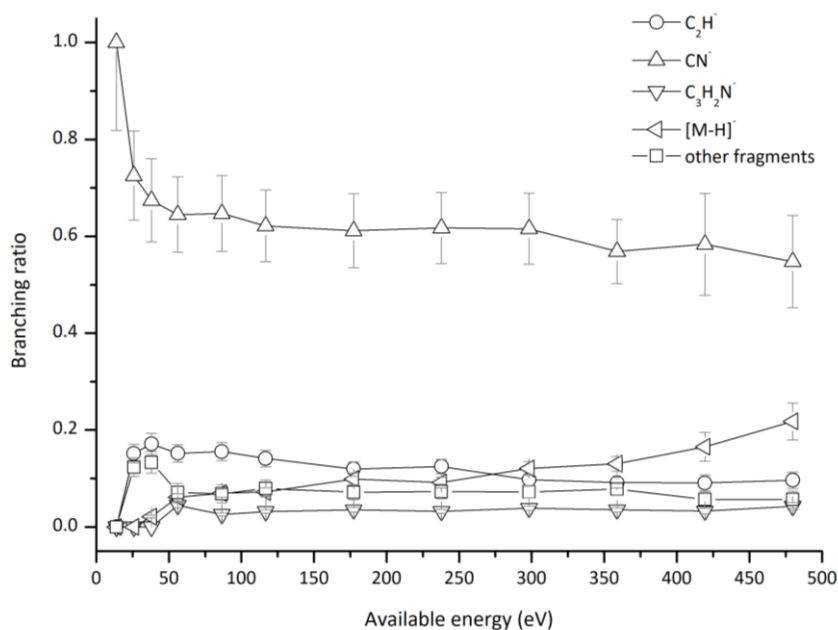


Figure 4.17. Pyrimidine (Pyr) branching ratios (fragment anion yield/total anion yield) of the main negative ions formed as a function of the collision energy in the centre-of-mass frame. See text for details.

Table 4.5. Negative ions formed in potassium collisions with pyrimidine (Pyr).

Mass (u)	Proposed assignment
12	$C^-$
13	$CH^-$
14	$CH_2^-$
15	$CH_3^-$
24	$C_2^-$
25	$C_2H^-$
26	$CN^- / C_2H_2^-$
39	$C_2HN^- / C_3H_3^-$
40	$C_2H_2N^-$
50	$C_3N^-$
52	$C_3H_2N^- / C_2N_2^-$
79	$C_4H_3N_2^-$

# CHAPTER 5

## ELECTRON TRANSFER EXPERIMENTS IN $O_2^-$ – MOLECULES COLLISIONS

### 5.1 Experimental Electron Detachment Cross-sections for Collisions of $O_2^-$ with $N_2$ Molecules in the Energy Range 50-7000 eV<sup>4</sup>

#### Abstract

A novel experimental setup has been implemented to perform gas-phase collision experiments between anionic beams and neutral molecular targets. The experimental arrangement can be found in Chapter 3. The primary anionic beam is produced through a pulsed hollow cathode discharge-induced plasma, deflected and focused towards the collision region where impact with the gas-phase target molecule occurs. Electron detachment cross-sections are measured from the attenuation of the anionic beam after the interaction with a well-known  $N_2$  molecular density. During the collision, negative and positive fragment ions are produced, and mass analysed by time-of-flight (TOF) mass spectrometry. Here we present absolute total electron detachment cross-sections and relative ionisation cross-sections in the energy range 50-7000 eV.

---

<sup>4</sup> This chapter is based on the following publication in preparation: Experimental electron detachment cross-sections for collisions of  $O_2^-$  with  $N_2$  molecules in the energy range 50-7000 eV (2019).

### 5.1.1 Introduction

Collisions between electrons and atoms/molecules have been extensively studied for decades within the scope of different research fields (fundamental and applied) and more thoroughly during the last 20 years regarding their interaction with biomolecules to understand the underlying molecular and atomic mechanisms of radiation induced interaction with such constituents [35,37,207–209]. However, free electron attachment processes may not be sufficiently representative to completely describe the interactions within a particular environment. However, studies on electron transfer processes are also predominant in several mechanisms and play relevant roles in a variety of environments in particular within the biological environment [69,73,75,98,131,210].

A particular interest is being given to the comprehensive knowledge of ion interactions with atoms and molecules, especially in themes related to astrophysics and interstellar medium but with increasingly interest to biological effects. The production of excited negative and positive ions and free radicals especially those oxygen-derived, termed reactive oxygen species (ROS), plays a significant role in planetary systems and in biology and medicine [211]. The overproduction of ROS results in oxidative stress in cellular environment destabilizing cells integrity, a mechanism which seems to be operative in the case of tumour cells. Additionally, the interaction of radiation with biological matter, in the case of radiation therapy, yields high levels of ROS. In the living systems the superoxide anion ( $O_2^-$ ) is one of the products formed by the interaction of free electrons with oxygen molecules, which subsequently interact with other surrounding molecules producing several highly reactive species, like hydrogen peroxide and peroxyxynitrite, resulting in severe damage for key physiological components [59]. Therefore, accurate cross-section results for these interactions are extremely relevant to the use of radiation in medicine and in the development and optimization of new radiotherapy protocols. However the molecular description regarding electron transfer processes and the efficiency of such radiation induced processes are still poorly known. Another interesting aspect pertains to simple molecules such as  $O_2$ ,  $N_2$ ,  $CO$ ,  $CO_2$  and  $CH$  that are important constituents of numerous interstellar environments [212,213]. For instance, it was shown that the superoxide radical ion ( $O_2^-$ ) can be formed directly on Mars-analogue mineral surfaces exposed to ultraviolet radiation under a simulated Martian atmosphere [214].

From a literature survey, we note that several studies have been published regarding collisions between ions and atoms/molecules, with special relevance to positive ions as projectiles, in ionization cross-section measurements [212,215–219]. However, the studies using negative oxygen ions as projectiles are still relatively scarce and old, particularly for low-energy collisions ( $< 1000$  eV). Some studies regarding collisions of  $O_2^-$  with  $N_2$  reported experimental and theoretical calculations for electron detachment cross-sections of negative ions. For high energy collisions ( $> 30$  keV) Jalbert *et al.* [115] have demonstrated that the electron detachment cross-section for different incident ions in  $N_2$  shows a maximum at a velocity 0.4 a.u, which was interpreted to a shape-resonance that appears in electron- $N_2$  collisions. These authors have also proposed a semi-empirical model to extrapolate

cross-section values for lower energies. At intermediate and low energies, ion- $N_2$  collisions have been also investigated emphasizing the role of the  $^2\Pi_g$  shape resonance of  $N_2$ . Interesting to note that in  $H^- - N_2$  collisions, a similar behaviour has been observed [97,103,220]. Bennett *et al.* [110] have also performed measurements using different incident beams and different targets (including  $O_2^-$  in  $N_2$ ) in the energy range 1 to 4 keV. Moreover, Doering [112] and Matić and Čobić [113] also demonstrated a cross-section enhancement ( $10^{-16}$ – $10^{-15}$  cm<sup>2</sup>) with ion incident energy. Inelastic collisions between ions ( $H^-$ ,  $O^-$  and  $Cl^-$ ) and atoms ( $H_2$ ,  $O_2$  and  $Cl_2$ ) were also investigated by Hasted and co-workers [108,109,221,222], where large cross-section values at low energies have been obtained and interpreted as due to the prevalence of excited states of the negative ions.

In this study we report on the absolute total electron-detachment cross-sections in the energy range from 50 eV to 7 keV as measured in a transmission-beam attenuation experiment. In addition, total and partial ionisation cross-sections have been derived by correlating the observed ionic fragment intensities with the  $O_2^-$  beam intensity.

More details on the experimental setup and procedure followed to determine the present cross-section data on nitrogen are given in Section 3.2.

### 5.1.2 Results and Discussion

A comprehensive investigation of the electron detachment cross-sections ( $\sigma_{\text{exp}}$ ) has been performed in a wide range of energies, from 50 up to 7000 eV with total uncertainty limits within 7-9 %. These include statistical uncertainties (5%) and the sum *in quadrature* of all the known error sources. The experimental results are presented in figure 5.1 for collisions of  $O_2^-$  with  $N_2$  molecules, and the numerical values are also listed in table 5.1. The experimental cross-section values between 50 and 3000 eV show a rather constant behaviour ( $\sim 9.0 \times 10^{-16}$  cm<sup>2</sup>) with the exception of a minimum at  $\sim 100$  eV and a significant enhancement at  $\sim 200$  eV (peaking at  $13.3 \times 10^{-16}$  cm<sup>2</sup>). Above 3000 eV the cross-section takes off reaching a value of  $14.4 \times 10^{-16}$  cm<sup>2</sup> at 7000 eV cross-section.

As far as we know, studies in collisions between negative oxygen ions ( $O^-$  and  $O_2^-$ ) and neutral gas-phase molecules are quite scarce and old, and normally performed at higher energies than those presented in this work. Figure 5.2 shows the experimental total electron detachment cross-sections (TEDCS) together with two other set of results from Jalbert *et al.* [115] and Bennett *et al.* [110]. Jalbert *et al.* [115] data reported a maximum TEDCS value at 0.4 a.u. ( $\sim 130$  keV) decreasing as the energy decreases down to 30 keV (blue triangles). Additionally, these authors presented a semiempirical model to extrapolate their data down to 200 eV (green dashed line), by assuming that the anion projectile can be viewed as a superposition of a neutral projectile ( $O_2$  core) plus a free electron simultaneously interacting with the molecular target. Interesting to note that this model provides cross-section values at 200 eV and 7 keV in relatively good agreement with the present data albeit the energy dependence fails to reproduce the local minimum that we observed at  $\sim 1$ -3 keV.

Older measurements from Bennet *et al.* [110] for incident energies from 1 to 4 keV (see figure 5.2) report absolute values for the TEDCS of  $O_2^-$  with  $N_2$  at 1 keV, 57% higher than the present data and about 13% lower than the semi-empirical model from ref. [115]. The origin of the discrepancies between Bennet *et al.*'s [110] and Jalbert *et al.*'s [115] is not clear. Notwithstanding, we believe that the semiempirical model from ref. [115] cannot be safely extrapolated to much lower energies, since in the 200–7000 eV incident anion energy range is equivalent (same velocity) to the electron 0.003–0.12 eV energy range. We now turn to a close comparison with the data of Bennett and co-workers [110], where their results are about 35% higher than ours, showing however cross-section values approximately constant in this energy range. Such discrepancy could be attributed to systematic errors in the sample target pressure reading and ion beam current measurements. Additionally we note that these authors used a Faraday cup to measure the projectile ion beam current. At these collision energies, positive ions can be formed from the impinging ion beam on the metal surface of the Faraday cup, which tend to underestimate the real negative ion current being collected.

Collisional detachment cross-sections for  $O_2^-$  and  $O^-$  on nitrogen were also reported by Doering [112] in the energy range 1.6–10 keV. The results show a similar behaviour with the present data. In terms of absolute values, and comparing the present data with Doering's, we note that the agreement is much better for  $O^-$  rather than for  $O_2^-$ , the former yielding  $9 \times 10^{-16} \text{ cm}^2$  at  $\sim 900 \text{ eV}$  and  $15 \times 10^{-16} \text{ cm}^2$  at  $\sim 7000 \text{ eV}$ , while the later showing differences of about 50–65% higher. Moreover, the results of Ranjan and Goodyear [114] for collisions at incident energies from 20 to 100 eV show a reasonable agreement with the present data, although with some discrepancies as to the behaviour of the cross-section as a function of the energy. Additional comparison with other results for collisions of  $O^-$  with  $N_2$  [111,223] also show a reasonable good agreement in terms of magnitude, although not in energy dependence up to 100 eV. From 100 to 400 eV the cross-section values increase with energy likewise in the present measurements but with no evidence of a local maximum.

Studies performed by Hasted and co-workers [109] in collisions of  $O_2^-$  and  $O^-$  with different atomic and molecular targets in an energy range of 5–3600 eV are also used to compare with the present set of measurements. Detachment cross-sections results of  $O^-$  in  $N_2$  and  $H^-$  in  $H_2$  show an increasing tendency up to 400 eV where a plateau is reached, decreasing up to 3600 eV. These authors concluded that the dominant process is due to direct detachment, and no negative ions can be formed. However, for the case of  $O^-$  in  $O_2$  and  $O_2^-$  in  $O_2$  a very pronounced local maximum is visible at around 100 eV following a similar behaviour to that of the present measurements. Hasted and co-workers associated this with a strong dominance of charge transfer processes, following Massey's assumption [224,225] that a simplified form of 'near-adiabatic' theory governs the charge transfer of negative ions. Indeed, some other studies using  $H^-$  as incident projectile and  $N_2$  as target have shown that electron detachment can proceed via formation of a temporary negative ion, in a process known as charge transfer to shape resonances (CTSR) [97,103,105]. Theoretical and



experimental measurements using electron spectroscopy have attributed this to the post-collisional decay of the  $N_2^- 2\Pi_g$  shape resonance formed by charge exchange during the collision.

Comparing cross-section absolute values for the same incident anions and different targets ( $O^-$  with  $N_2$ ,  $O_2$ , Ar and Ne) also shows that the type of neutral target is not the principal governing factor in determining its detachment cross-sections in the low-energy collision regime, i.e.  $< 100$  eV.

Another interesting aspect of the collisional process pertains to the possible role of excited states of the negative ions. In the case of collisions of  $O^-$  with rare gas atoms, a maximum around 200 eV has been reported (note that such is also observed in the present data although with a  $O_2^-$  projectile) by Hasted [108] and attributed to excited states of long lifetimes in the negative ion beam. Moreover, identical rationale was put forward in  $Cl^-$  collisions with rare gases (Xe, Ar, He) [108]. Therefore, large cross-sections at low energies can be interpreted as being due to the presence of excited states of the ion.

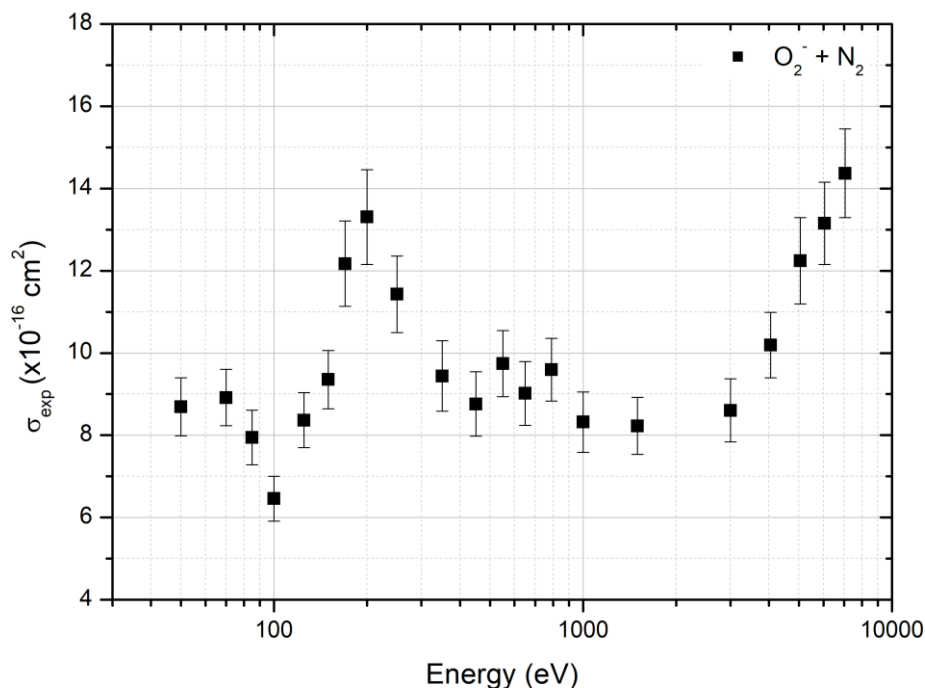


Figure 5.1. Electron detachment cross-sections in the 50-7000 eV energy range for  $O_2^-$  collisions with  $N_2$ .

In figure 5.2 we also present the results of the  $N_2^+$  and  $N^+$  partial ionisation cross-sections for three different collision energies (200, 550 and 1000 eV). These are relative values since we cannot give an accurate measure of the absolute beam intensity of the oxygen projectile in the collision region. From the total relative cross-section values we have established an approximation considering that no attenuation occurs after the beams exists the collision chamber. At 200 eV the partial relative ionisation cross-section for  $N^+$  production shows a local maximum. This may indicate that the maximum of the total electron detachment cross-section can be associated with ionisation processes

between  $O_2^-$  and  $N_2$ , especially those yielding dissociative ionisation (i.e.  $N^+$  formation). Recently, Takahashi *et al.* [226] (and references therein) have reported doubly excited states of molecular nitrogen in the generalised oscillator strength distributions of  $N_2^+$  and  $N^+$ , showing their mainly auto-ionising character. It has been commonly accepted that optically allowed doubly excited states of  $N_2$  are observed for photon excitation energies in the 20–40 eV range as broad features [227]. We note that in the photoabsorption spectrum of Codling [228] a discrete structure at 23 eV was assigned to doubly excited Rydberg states  $(1\pi_u)^{-1}(3\sigma_g)^{-1}(1\pi_g)^1(ns\sigma_u)^1$  with principal quantum number  $n = 4, 5$  converging to the  $C^2\Sigma_u^+$  state of  $N_2^+$ . Additionally, fluorescence data extended those Rydberg states for  $n = 3-10$  and dissociative doubly excited states correlating with satellites of  $N_2^+$  as broad peaks in the range 23–33 eV were reported by Ukai and co-workers [229]. At 200 eV energy ion impact an average of 10% energy loss to the target may be expected [161] and so, we suggest that the enhancement feature at 200 eV (figure 5.1) is due to the role of such double excited states, which by their nature result in either auto-ionisation or neutral dissociation [226]. Such assumption seems reasonable since we note in figure 5.2 higher  $N_2^+$  and  $N^+$  yields at 550 eV rather than at 1000 eV.

Table 5.1. Present experimental results of total electron detachment cross-sections for  $N_2$  in collisions with  $O_2^-$ .

Energy (eV)	$\sigma_{\text{exp}}$ ( $\times 10^{-16} \text{ cm}^2$ )	Statistical uncertainty (%)
50	8.6	8.09
70	8.9	7.68
85	7.9	8.32
100	6.5	8.46
125	8.4	7.99
150	9.4	7.57
170	12.2	8.51
200	13.3	8.64
250	11.4	8.17
350	9.4	9.10
450	8.8	8.95
550	9.7	8.27
650	9.0	8.58
790	9.6	7.98
1000	8.3	8.81
1500	8.2	8.40
3000	8.6	8.90
4050	10.2	7.83
5050	12.2	8.56
6050	13.2	7.62
7050	14.4	7.52

### 5.1.3 Conclusions

A novel experimental setup for investigating collisions between anionic beams and neutral gas-phase molecular targets has been described. The precursor anionic beam projectile is produced in a hollow cathode discharge-induced plasma, guided to the interaction region by a set of deflecting plates and made to interact with a neutral target beam in an interaction region. With this configuration it was possible to measure total electron-detachment cross-sections for molecular oxygen anions impinging

on nitrogen molecules at selected incident energies between 50 and 7000 eV. Positive TOF mass spectra for  $N_2$  were obtained and partial and total ionisation cross-sections were obtained.

The total cross-section measurements have an increasing behaviour with energy, showing a local maximum at 200 eV (lab frame). Since no measurements of this type covering the entire energy range were reported previously, some tentative assignments have been put forward here. Comparisons with other studies [108–110,112,113,115] using different projectile anionic beams ( $O_2^-$ ,  $O^-$ ,  $H^-$ ) and different target molecules have shown reasonably good agreement with the present results in magnitude and energy dependence. The structure at 200 eV was interpreted on the light of different processes either through the decay of a temporary negative ion of  $N_2^-$   $^2\Pi_g$  shape resonance formed by charge exchange [97,103,105] or reactions involving excited states of  $O_2^-$ . Relative ionisation cross-sections were also reported for  $N^+$  and  $N_2^+$  and the energy behaviour related to  $N^+$  formation (dissociative ionisation) discussed on the basis of double excited states of the molecular nitrogen [226–229].

Future improvements and comprehensive work exploring the mechanism in anion-molecule collisions, especially through energy loss experiments are mandatory to help interpreting the interaction processes involved in these type of collisions as well as relevant theoretical contribution to further our knowledge about this processes.

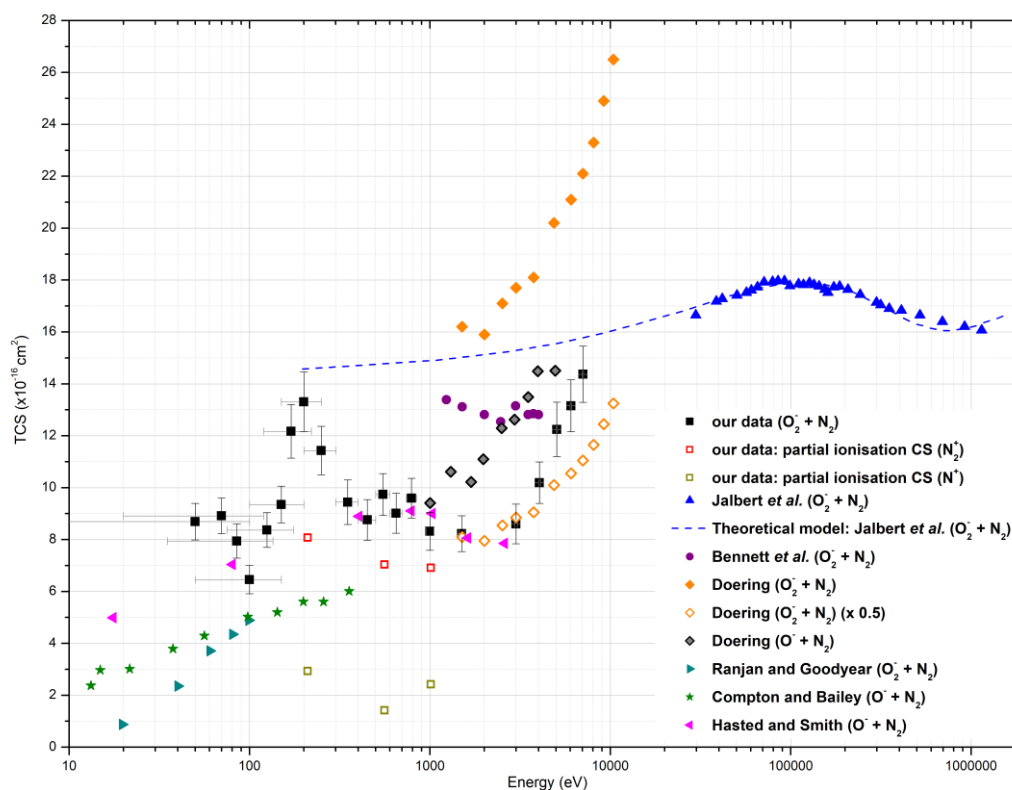


Figure 5.2. Total electron detachment cross-sections for  $O_2^-$  on  $N_2$  (black squares) compared with previously published experimental results from Jalbert *et al.* (blue triangles) and Bennett *et al.* (violet circles), and a theoretical model from Jalbert *et al.* (green dash line). The red circles represent the total ionization cross-sections for the formation of  $N_2^+$  and  $N^+$ . See also the legend on the plot for other symbols.

## 5.2 Experimental Electron Detachment Cross-sections for Collisions of $O_2^-$ from Water and Pyridine Molecules in the Energy Range 10–4000 eV<sup>5</sup>

### Abstract

In this section, we report an experimental study of electron detachment cross-sections for  $O_2^-$  in water and pyridine molecules. Following the results discussed in Section 5.1, these experimental results were obtained by making use of a novel homemade crossed beam apparatus described in detail in Section 3.2. Relative cross-sections for the formation of positive and negative ions were also obtained as well as time-of-flight negative ion mass spectra in a wide collision energy range (10–4000 eV in lab frame), providing the first measurements of such ionic projectile in water and pyridine molecular targets.

---

<sup>5</sup> This chapter is based on the following publication in preparation: Experimental electron detachment cross sections for collisions of  $O_2^-$  from water and pyridine molecules in the energy range 10–4000 eV (2019).

### 5.2.1 Introduction

In Chapter 1 we have discussed the role of indirect effects of radiation caused by the production of secondary low-energy electrons (LEE) and highly reactive species due to water radiolysis. In fact, after high-energy radiation impact a set of reactions are triggered in the physiological environment in particular those due to the interaction of such LEE with biomolecules. Since living organisms are composed by ~70/80 % of water ( $H_2O$ ), the interaction of LEE with such molecule may result in the production of ions and radical species, such as  $H^\cdot$ ,  $OH^\cdot$ . Furthermore, the presence of oxygen in the cellular systems and the interaction of LEE with  $O_2$  also leads to the formation of ions and reactive compounds such as the superoxide anion ( $O_2^{\cdot-}$ ). Further to this, the study on the interaction between  $O_2^-$  and molecular constituents of living systems is crucial to understand the role of such processes and the consequences they may have in cellular damage. The role of the oxygen and water are not exclusive of the living organisms, but also important in astrophysics. Indeed, studies on water-vapour photonucleation demonstrate the formation of water droplets upon UV radiation of supersaturated air [230]. This was explained using a theory based on the excitation by a UV photon of a collision complex ( $H_2O \cdot O_2$ ) to a charge transfer complex ( $H_2O^+ O_2^-$ ). Owing to its large dipole moment, the complex acts as an effective nucleation centre, attracting the polar water molecules and promoting the formation of a cluster (Wilson cluster). Studies on the water molecule, have been performed for many years, using several spectroscopic techniques and methods. Dissociative electron attachment to  $H_2O$  and  $D_2O$  was studied using ion momentum imaging spectrometry [231]. Fuss *et al.* [232] have developed a model based on electron interaction cross-sections with water which allows the study of radiation effects not only in terms of energy deposition (absorbed dose and stopping power) but also in terms of the number of induced molecular processes. Itakawa and Mason [233] presented a compilation of cross-section data for electron collision with water molecules. Total elastic, total inelastic, and elastic differential cross-section measurements were performed by Tattersall and co-workers in positron interactions with water [234]. Total absorption and photoionisation cross-sections of water vapour between 100 and 1000 Å were reported by Haddad and Samson [109]. Gobet *et al.* [235] reported cross-section for electron-loss and ionisation of water vapour molecules by neutral atomic hydrogen impact at velocities of the order of the Bragg peak (20–150 keV). These are only some of the many research studies performed using the water molecule.

Pyridine ( $C_5H_5N$ ) is the simplest aromatic azabenzene heterocyclic compound with a N atom replacing the CH bond in the benzene ring (figure 5.3). It is present in many compounds of biological relevance as nicotine, B group vitamins and nucleotides cytosine, uracil and thymine [1]. It is naturally occurring and synthetic pyridines led to investigations into their pharmacological properties, as well as agrochemical properties [237]. Therefore, pyridine has attracted considerable attention due to its industrial and biological relevance. The replacement of a carbon atom by a nitrogen atom in the benzene ring leads to perturbations in the energy levels and, consequently results in new transitions due to excitation of the lone-pair electrons [238,239]. The need to understand at

the molecular level radiation damage induced processes in biomolecules, such as water and pyridine, has motivated numerous theoretical and experimental studies, especially for electron scattering. This data is extremely useful to model radiation tracks within the biological medium since it gives a description of both energy deposition and angular distributions. Pyridine has been investigated in many research experimental and theoretical studies. It has a relatively high permanent dipole moment ( $\sim 2.2$  D [240]) so the dipole driven cross-section behaviour (magnitude) at low scattering angles may be particularly enhanced among the differential cross-sections (DCSs). The formation of temporary negative ions (TNIs) (shape resonances) in electron interactions with pyridine and other azo-related compounds was also investigated [176,177,241]. Three  $\pi^*$  shape resonances were identified at 0.72, 1.18 and 5.58 eV by Modelli and Burrow [177]. Total electron-scattering cross-sections from pyridine were experimentally measured by Lozano *et al.* [242] and Traoré *et al.* [243]. Theoretical calculations on electron scattering cross-section for elastic and inelastic processes were also explored using R-Matrix and IAM-SCAR methods [244], as well as the Schwinger Multichannel Method (SMC) with pseudopotentials [245]. Electron impact ionisation cross-sections were measured by Jiao *et al.* [246] and Bull *et al.* [247]. Dissociative electron attachment to pyridine and other molecules containing the pyrazine ring was studied in the gas phase for low energy electron interactions [238] showing the dehydrogenated parent anion as the dominant yield. Electronic excitation and ionisation of pyridine were also investigated by Wan *et al.* [239], while the ionisation energies for both outer and inner valence orbitals and new adiabatic values were also reported [248]. Finally, we note VUV photoionisation studies of free azabenzenes such as pyridine [249].

Studies on ion impact with water and pyridine are scarce in the literature and those available are more related to the impact of positive ions at higher energies, i.e. in the keV domain [250–254]. In Section 5.1, we have presented a set of results regarding the impact of  $O_2^-$  in  $N_2$  combining a comprehensive literature inspection about collisions between negative ions and molecules. We have discussed the possible mechanisms that can lead to the high cross-section values observed for lower impact energies which may be associated with the presence of excited states of the molecular target. In studies on collision detachment cross-sections for  $O^-$ ,  $H^-$  and  $Cl^-$  in different neutral atoms and simple molecules (including  $O^-$  in  $H_2O$ ), Hasted and Smith [109] have discussed the fact that the type of neutral target with which the projectile negative ion collides is not the principal governing factor in determining its detachment cross-section at energies between 10 and 2500 eV. Tuan *et al.* [100,102] have also investigated the electron detachment in  $H^-$  and  $F^-$  with  $CO_2$  demonstrating that in such processes the influence of the charge transfer to shape resonances and the excitation of the target molecule constitute an important detachment channel. Doering and Moore [255] studied the excited states of pyridine by proton-impact and  $He^+$ -impact energy-loss spectra in gas-phase at low pressure.

Therefore, the deficiency in studies on negative ion impact in neutral biomolecules incited us to explore the fragmentation spectra and electron detachment cross-sections for collisions between  $O_2^-$

and water and pyridine molecular compounds, over the impact-energy range from low to intermediate energies, i.e. 10 to 4000 eV.

Details on the experimental setup and procedure followed to determine the present cross-section data on water and pyridine are given in Section 3.2.

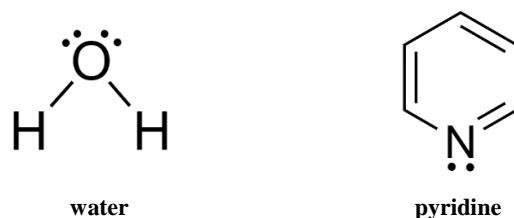


Figure 5.3. Molecular structure of water (H<sub>2</sub>O) and pyridine (C<sub>5</sub>H<sub>5</sub>N).

### 5.2.2 Results and Discussion

In this section we present the results obtained in collisions between oxygen anions and neutral molecules of water and pyridine. In table 5.2 we present the experimental electron detachment cross-sections ( $\sigma_{\text{exp}}$ ) (in cm<sup>2</sup>) for  $O_2^-$  in water and pyridine in the energy range 10 to 4000 eV, together with their respective statistical uncertainties. These values are also plotted in figure 5.4. The relative cross-section values related to the negative and positive ions formation are shown in figures 5.5 and 5.6, for water and pyridine, respectively together with the electron detachment cross-section values. Figures 5.7 and 5.8 depict typical TOF mass spectra of ions from both molecules, and tables 5.3 and 5.4 present the assignments to the anionic fragments detected (negative and positive ions).

The  $\sigma_{\text{exp}}$  values for water decrease with energy showing a maximum value of  $19.9 \times 10^{-16}$  cm<sup>2</sup> at 10 eV (lab frame) and a minimum value of  $5.1 \times 10^{-16}$  cm<sup>2</sup> at 4000 eV. A careful inspection of figure 5.2 also reveals that in the cross-section data two main local structures with higher  $\sigma_{\text{exp}}$  values at 250 eV and 500 eV are observed. At 1500 eV it seems that there is also a slightly increase in the  $\sigma_{\text{exp}}$  values. In the case of pyridine, the  $\sigma_{\text{exp}}$  results in figure 5.4 show a decreasing tendency with energy with a maximum value at 10 eV ( $57.2 \times 10^{-16}$  cm<sup>2</sup>) and minimum value of  $15.3 \times 10^{-16}$  cm<sup>2</sup> at 4000 eV. This means that the cross-section values for pyridine are approximately three times higher than for water. Similarly to the water molecule, pyridine  $\sigma_{\text{exp}}$  values also show three main local maxima at 130, 400 and 1200 eV. This resemblance is in agreement with the discussion in Hasted and Smith [109], where these authors have verified that the type of neutral target is not the principal governing factor in determining the detachment cross-section. In collisions of negative ions with neutral atoms, the large cross-section values obtained in the first few hundred eV have been interpreted as being due to the presence of ions in an excited state near the continuum [108].

We also note that there are some other studies using  $H^-$  as a projectile in collisions with molecules, showing that in addition to a continuous distribution, which can be attributed to a direct detachment process, the H atoms energy loss spectra display prominent peaks at the position of the shape

resonance  $^2\Pi_g$  of the molecular target. Such results indicate the importance of CTSR in negative ion-molecule collisions in fast collisions. However, unlike this case, in other studies using  $F^-$  and  $Cl^-$  this CTSR process is not visible in the low velocity collision regime. Therefore, there is some controversy about the influence of such collisional reaction in negative ion-molecule collisions [100,102,103]. Although these studies have been performed for simple molecules like  $N_2$  or  $CO$  they can give some highlights to the present results where structures associated with high cross-section values are observed, for both water and pyridine molecules.

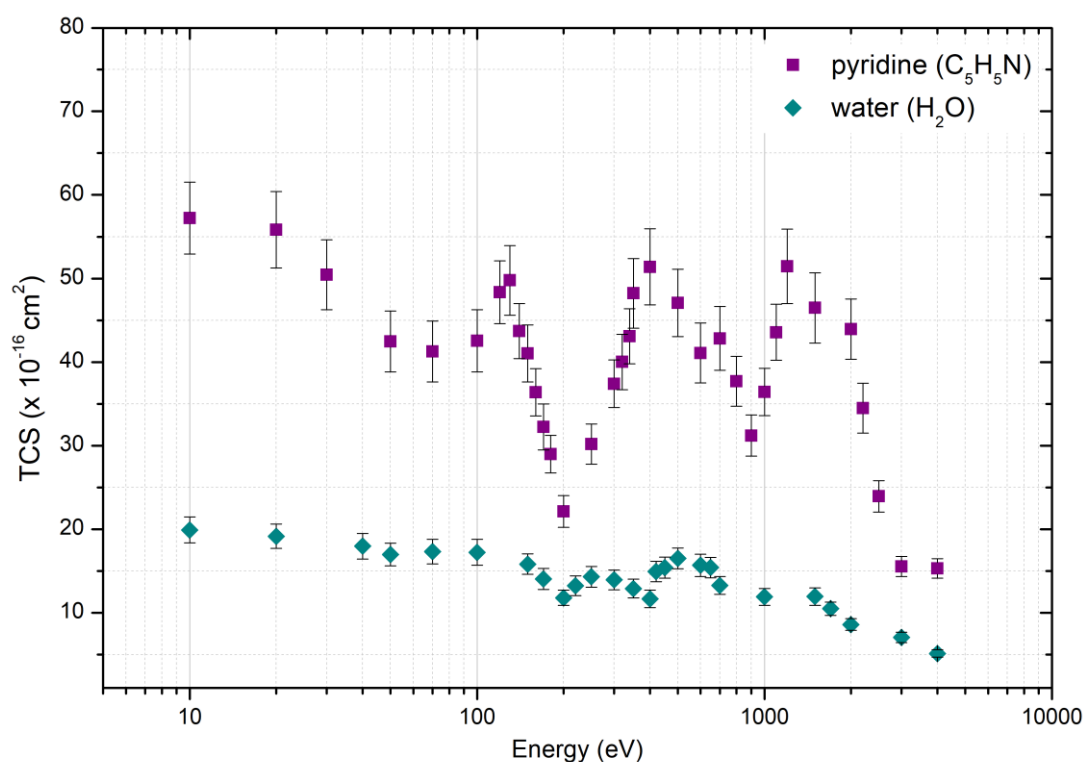


Figure 5.4. Electron detachment cross-sections in the 10–4000 eV energy range for  $O_2^-$  collisions with water (cyan diamonds) and pyridine (purple squares).

The relative cross-section values for positive and negative ions formation were also experimentally obtained for both pyridine and water. These results can also give some hints about the structures that appear in the electron detachment cross-section showed in figure 5.4. A close observation of figure 5.5, shows that at 500 eV and 1500 eV an increase of the relative cross-section for the negative ions formation (yellow dash line), which may indicate a close relation between the high cross-section values in total electron detachment cross-section at that energies. Therefore, such peaks can be due to charge transfer processes. However, the peak at 250 eV cannot be explained as based on this assumption, as well as the strong enhancement in the relative cross-section for both positive and negative ions at 3000 and 4000 eV (lab frame), respectively. Further experiments are needed to clarify this behaviour.



The same procedure was implemented for the pyridine molecule, and it seems that the positive ions formation through ionization processes may play an important role in the preminent peaks observed in the electron detachment cross-sections. Additionally, the feature at 1200 eV may be related to negative ion formation through charge transfer reactions since a significant enhancement is observed in the relative negative ions cross-section (yellow dash line in figure 5.6).

Table 5.2. Experimental electron detachment cross-sections for O<sub>2</sub><sup>-</sup> collisions with water and pyridine.

Water			Pyridine		
Energy (eV)	$\sigma_{\text{exp}}$ ( $\times 10^{-16}$ cm <sup>2</sup> )	Statistical uncertainty (%)	Energy (eV)	$\sigma_{\text{exp}}$ ( $\times 10^{-16}$ cm <sup>2</sup> )	Statistical uncertainty (%)
10	19.9	7.80	10	57.2	7.52
20	19.2	7.54	20	55.8	8.18
40	18.0	8.55	30	50.5	8.32
50	17.0	7.91	50	42.5	8.56
70	17.3	8.52	70	41.3	8.80
100	17.2	8.98	100	42.6	8.74
150	15.8	7.66	120	48.3	7.79
170	14.0	8.95	130	49.8	8.37
200	11.8	7.83	140	43.7	7.53
220	13.2	8.92	150	41.0	8.33
250	14.3	8.73	160	36.4	7.73
300	13.9	8.48	170	32.2	8.55
350	12.9	8.67	200	29.0	7.73
400	11.7	8.93	250	22.1	8.53
420	14.9	8.19	300	30.2	7.99
450	15.4	8.13	320	37.4	7.62
500	16.5	7.57	340	40.0	8.27
600	15.7	8.50	350	43.1	7.63
650	15.4	7.93	400	48.2	8.63
700	13.3	8.04	500	51.4	8.84
1000	11.9	8.44	600	47.1	8.55
1500	12.0	8.75	700	41.1	8.76
1700	10.5	7.55	800	42.8	8.91
2000	8.6	7.99	900	37.7	7.91
3000	7.0	8.76	1000	31.2	7.88
4000	5.1	8.70	1100	36.4	7.74
			1200	51.5	8.67
			1500	46.5	9.03
			2000	43.9	8.24
			2200	34.5	8.61
			2500	23.9	7.88
			3000	15.5	7.64

The time-of-flight mass spectra for water and pyridine are shown in figures 5.7 and 5.8 and the assignment are presented in tables 5.3 and 5.4 for negative and positive ionic formation in good agreement with the data of Cacace *et al.* [230]. Figure 5.7 depicts two typical TOF mass spectra for water at 500 eV lab frame, for both positive and negative ions formation, while figure 5.8 is for pyridine at 1000 eV lab frame. In the case of water molecule the most intense ionic fragments correspond to those at 16, 17 and 18 m/z, which were assigned to O<sup>-</sup>/O<sup>+</sup>, OH<sup>-</sup>/OH<sup>+</sup> and H<sub>2</sub>O<sup>+</sup>. The TOF mass spectra resolution is relatively poor and, therefore it is not possible to distinguish properly consecutive peaks with mass difference of 1 m/z.

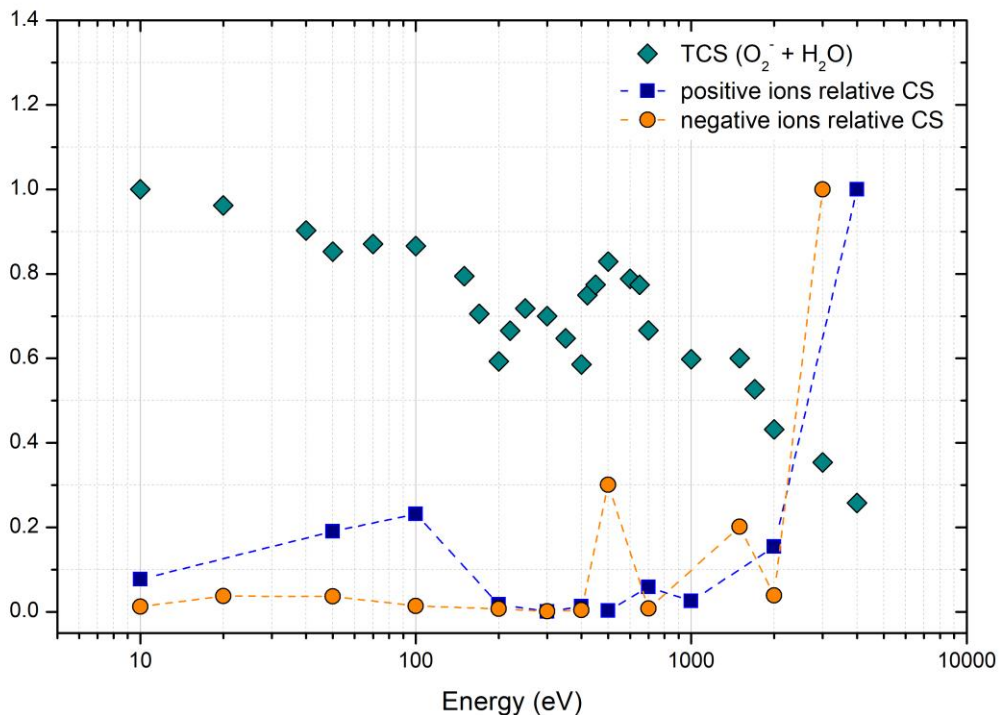


Figure 5.5. Comparison between electron detachment cross-section values and the relative cross-section for positive and negative ions formation in  $O_2^- + H_2O$  collisions. The values are normalized to the maximum value.

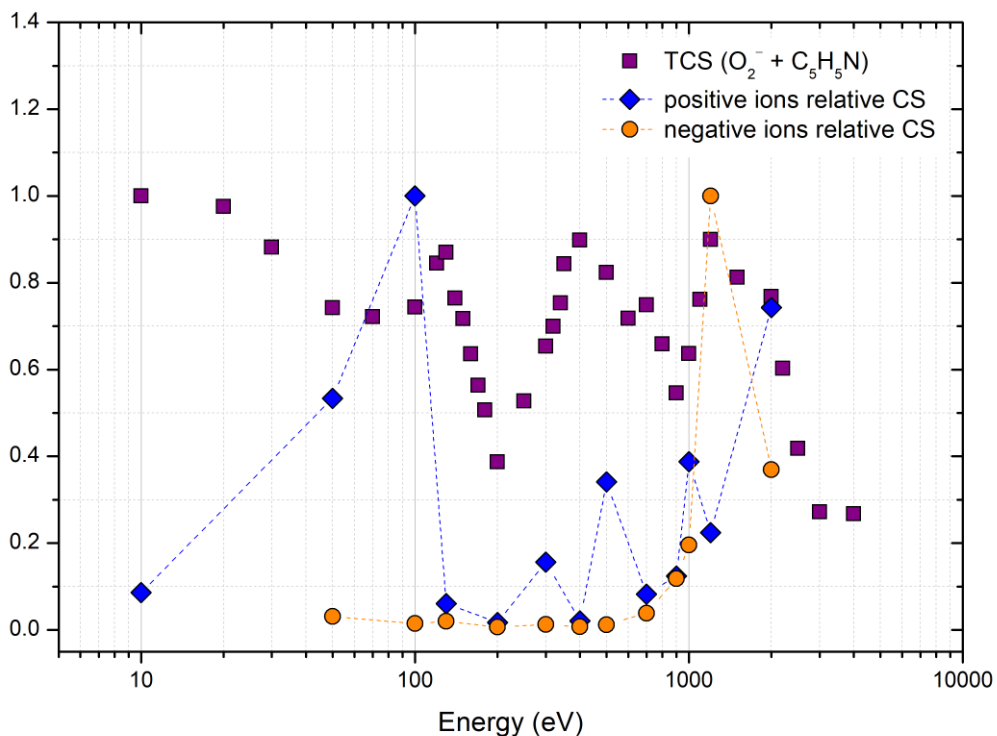


Figure 5.6. Comparison between electron detachment cross-section values and the relative cross-section for positive and negative ions formation in  $O_2^- + C_5H_5N$  collisions. The values are normalized to the maximum value.

Table 5.3. Tentative assignment of negative and positive ions formed in  $O_2^-$  collisions with water ( $H_2O$ ).

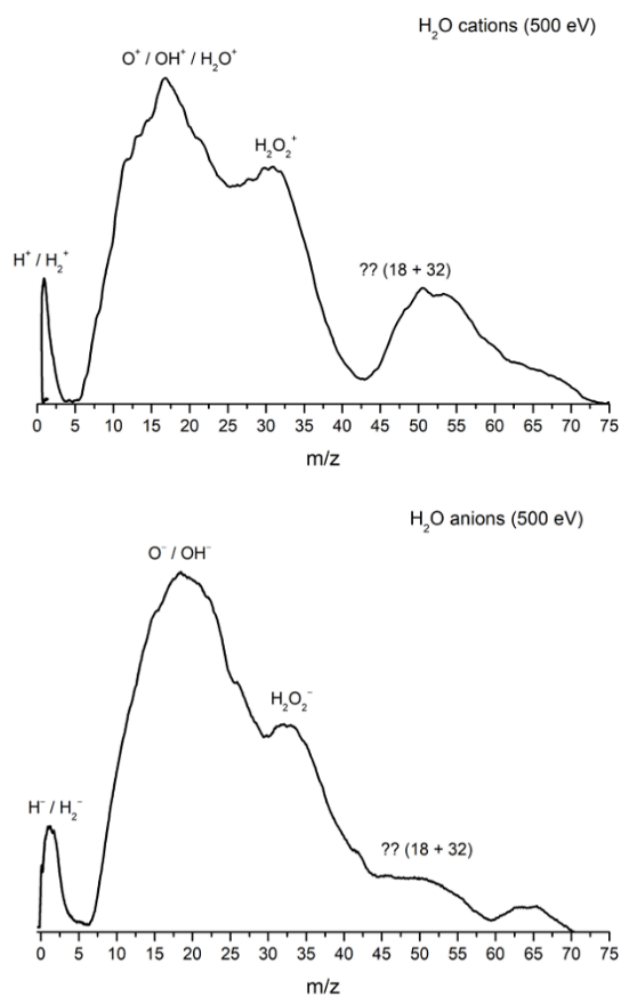
Mass (m/z)	Negative ions	Positive ions
1 / 2	$H^- / H_2^-$	$H^+ / H_2^+$
16 / 17	$O^- / OH^-$	$O^+ / OH^+$
18		$H_2O^+$
32	$O_2^-$	$O_2^+$
50	$(H_2O \cdot O_2)^-$	$(H_2O \cdot O_2)^+$

Regarding pyridine molecule, the main cationic fragments have been assigned to  $C_3H_3^+$  (39 m/z),  $C_3H_3N^+ / C_4H_4^+$  (53/54 m/z),  $C_5HN^+$  (75 m/z) and  $C_5H_4N^+/C_5H_5N^+$  (78/79 m/z). Regarding the fragmentation, we find some similarities with studies on electron impact ionization of pyridine [246] where the parent ion (79 m/z) and fragment ion  $C_4H_4^+$  (52 m/z) are the most abundant throughout the energy range probed, i.e. 10–200 eV. Some of the neutral products from dissociative ionization are due to the loss of H atoms and HCN molecules. These authors have also investigated charge transfer and proton transfer mechanisms of four important ions  $C_5H_5N^+$ ,  $C_4H_4^+$ ,  $C_4H_3^+$ , and  $C_4H_2^+$  in collisions with pyridine. Another interesting aspect of the TOF mass spectrum yielding positive ions is the presence of a feature at 111 m/z. Like in the case of water, here we tentatively assigned this anion to  $(C_5H_5N \cdot O_2)^+$ , although we could not find any related work in the literature to compare with. Moreover, it is remarkable that in the case of pyridine, such complex anion yield is the most intense of all anions assigned in the TOF mass spectrum which is in clear contrast with the case of water. This can be related to the dipole moment in water (1.85 Debye) and in pyridine (2.2 Debye), although the difference is not substantially high. We do not have any reasonable explanation for that at the moment and further studies are urgently needed to help clarifying such differences.

As far as negative ions formation is concerned, the most intense features in figure 5.8 are assigned to  $H^-$ ,  $C_3H_3N^-$  and the dehydrogenated parent anion and/or the parent ion. It is not possible to unambiguously distinguish between these two later ions given the limited mass resolution of the system. We note that DEA studies performed by Ryszka *et al.* [238] reported two main anions, 78 m/z (dehydrogenated parent anion) and 51 m/z ( $C_4H_3^-$  and  $C_3HN^-$ ), where formation of the dehydrogenated parent anion proceeds through resonances at 2.5, 5.3 and 9.0 eV, the later assigned to a core-excited shape resonance.

Table 5.4. Tentative assignment of negative and positive ions formed in  $O_2^-$  collisions with pyridine ( $C_5H_5N$ ).

Mass (m/z)	Negative ions	Positive ions
1 / 2	$H^- / H_2^-$	$H^+ / H_2^+$
12 / 13	$C^- / CH^-$	$C^+ / CH^+$
14 / 15	$N^- / CH_3^-$	
18		$H_4N^+$
26 / 27	$CN^-$	$CN^+ / CHN^+ / C_2H_3^+$
29	$CH_3N^-$	$CH_3N^+$
39		$C_3H_3^+$
40 / 41	$C_2H_2N^- / C_2H_3N^-$	
52 / 53	$C_3H_3N^-$	$C_4H_4^+ / C_3H_3N^+$
75	$C_5HN^-$	$C_5HN^+$
78 / 79	$C_5H_4N^- / C_5H_5N^-$	$C_5H_5N^+$
111		$(C_5H_5N \cdot O_2)^+$

Figure 5.7. Time-of-flight positive and negative ion mass spectra from  $O_2^-$ -pyridine collisions at 500 eV lab frame energy.

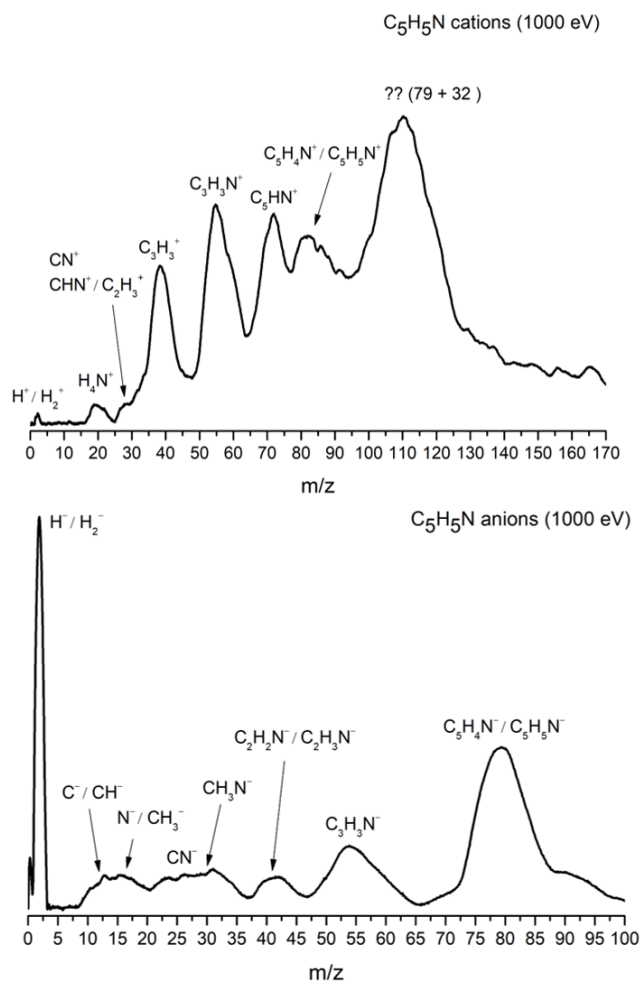


Figure 5.8. Time-of-flight positive and negative ion mass spectra from  $O_2^-$ -pyridine collisions at 1000 eV lab frame energy.

### 5.2.3 Conclusions

The present work provides the first investigation of the decomposition mechanisms of neutral water and pyridine in collisions with negative oxygen ions yielding different negative and positive ionic fragments, together with the first electron detachment cross-sections measurements. These results have been also performed for the first time in polyatomic molecules using a homemade crossed beam apparatus at Laboratorio de Interacciones Radiación-Materia, CSIC, Madrid. For both water and pyridine molecules, the electron detachment cross-section values show pronounced features which are suggested to be associated with the presence of excited states of the projectile and target species. Moreover, formation of negative and positive ions from water and pyridine after collisions with  $O_2^-$  were also investigated, and it seems that a correlation exists between the local maxima peaks observed in electron detachment cross-sections, and those due to ionization and/or to charge exchange interactions (negative ion formation). Notwithstanding, further comprehensive experimental studies are needed in order to clarify such dependency as well as state-of-the art calculations to further our knowledge on the underlying molecular mechanisms responsible for such findings



# CHAPTER 6

## CONCLUSIONS

### 6.1 Concluding Remarks

The main goals of this thesis were to investigate the mechanisms involved in electron transfer processes in atom/ion-molecule collisions. In order to achieve such attempt, this work was divided in two stages. The initial stage was developed using a crossed beam experiment where a neutral hyperthermal potassium beam crosses orthogonally with a gas-phase neutral molecular beam. This work was carried out by measuring the negative ion mass spectra that result from collisions of potassium atoms at different collision energies with a set of molecules, nitroimidazoles (4-nitroimidazole, 4NI and 2-nitroimidazole, 2NI) and methylated derivatives (1-methyl-4-nitroimidazole, Me4NI and 1-methyl-5-nitroimidazole, Me5NI). Imidazole and pyrimidine molecules were also investigated. The second stage comprised studies on collisions between oxygen negative ions ( $O_2^-$ ) and molecules of biological relevance, such as water and pyridine. The nitrogen molecule ( $N_2$ ) was also investigated in an initial phase of the experiments. These measurements were performed on a novel suitable cross molecular beam experimental setup, developed and optimised during the course of this thesis.

Next, we will present the main conclusions about the results obtained in these two different experimental systems, and finally, we will discuss some suggestions for future investigations as complement of the present work.

#### 6.1.1 Electron Transfer in K – Molecule Collisions

This section comprises two different research studies: (1) experimental studies with imidazole and nitroimidazole molecules, and (2) experimental studies with the pyrimidine molecule.

One of those studies involved measurements of site specific methylated derivatives of nitroimidazoles, in an attempt to understand the underlying molecular mechanisms during and after the collision. It was shown that in collision induced electron transfer to nitroimidazole molecules, bond breaking selectivity is achieved upon methylation on the N<sub>1</sub> site. Such methylation is not only responsible for blocking at low-collision energies the N<sub>1</sub>-CH<sub>3</sub> bond breaking channel but suppresses an essential decomposition channel yielding the neutral radical OH<sup>•</sup>. The modest yield of radical NO<sup>•</sup> is only operative at higher collision energies but limited to 4(5)NI and 2NI. These findings present a novel experimental evidence of selective chemical bond breaking by just tuning the proper collision energy in atom-molecule collision experiments.

A comprehensive investigation of the decomposition mechanisms of nitroimidazoles and imidazole in electron transfer collisions with neutral potassium atoms was also carried out. The major fragment anion channels have been investigated as a function of the available energy in the centre-of-mass frame. In the case of nitroimidazoles (4NI, 2NI and methylated molecules) the parent anion was identified as the most intense fragment over the entire energy range (10 – 1000 eV lab frame) which is only observed in DEA studies for resonances close to 0 eV. Such difference may be explained considering the high dipole moment of these molecules and their electron affinity. The presence of a third body (K<sup>+</sup>) in the collisional complex system (K<sup>+</sup>M<sup>-</sup>) can also contribute to the observation of different reaction channels, which can be explained based on the non-adiabatic description of the collision process. Other important anionic species were assigned as part of the fragmentation pattern of nitroimidazoles, such as NO<sub>2</sub><sup>-</sup>, the loss of OH and NO. Additionally, the studies with imidazole showed that the presence of a NO<sub>2</sub> group in the imidazole ring brings considerable modifications in the fragmentation pattern, as compared to the nitroimidazoles. In the imidazole molecule, the TOF mass spectra are dominated by the dehydrogenated parent anion, CN<sup>-</sup> and C<sub>2</sub>H<sub>2</sub>N<sup>-</sup>. We have also observed that the dehydrogenated parent anion seems to be a precursor in the formation of other fragment anions. Therefore, the present work opens up an opportunity to contribute to the current need of many more charge transfer collisions that can initiate selective reactivity of the kind demonstrated here. Moreover, such studies can support investigation for new chemical compounds for different applications such as in tumour radiation therapy through nitroimidazole based radiosensitisation.

The decomposition mechanisms of neutral Pyr in collisions with neutral potassium atoms yielding ion-pair formation were also explored in this thesis, supported by theoretical calculations. These studies revealed that the major negative ions produced during the electron transfer were assigned to the cyanide anion, the de-hydrogenated parent anion, and fragment anions related to the pyrimidine ring opening due to abstraction of HCN units from (Pyr-H)<sup>-</sup>. We have also shown that ion-pair formation in collisions of potassium atoms with pyrimidine molecules, yields two different electronic states of the metastable parent anion. These states have vertical electron affinities of (-5.69±0.20)



and  $(-7.57 \pm 0.20)$  eV, assigned to  $\pi_3^*(b_1)$  and a  $\pi_{CH}^*$  states, the latter accessible through a core-excited resonance.

### 6.1.2 Electron Transfer in $O_2^-$ – Molecule Collisions

Comprehensive studies on the interaction of nitrogen, water and pyridine with an oxygen anionic beam were performed in a wide range of collision energies. In such studies, positive and negative ions formation was detected by TOF mass spectrometry. The absolute electron detachment cross-sections were also experimentally obtained in a wide energy range for the molecules listed.

Regarding  $N_2$  measurements, the total electron detachment cross-section values present a remarkable dependence on the incident energy, peaking at 200 eV (lab frame). Since no measurements of this kind covering the entire energy range were reported previously, some tentative assignments have been put forward through comparisons with other related studies. The structure at 200 eV was interpreted on the light of different processes either through the decay of a temporary negative ion of  $N_2^- \ ^2\Pi_g$  shape resonance formed by charge exchange or reactions involving excited states of  $O_2^-$ .

The results on water and pyridine represent the first studies in polyatomic molecules for collisions with anionic projectiles. For both water and pyridine molecules, the electron detachment cross-section values show pronounced features which are suggested to be associated with the presence of excited states of the projectile and target species. Moreover, formation of negative and positive ions from water and pyridine in collisions with  $O_2^-$  were also investigated, and a correlation between the local maxima peaks observed in the electron detachment cross-sections, and those due to ionisation and/or to charge exchange interactions (negative ion formation) with energy has been suggested.

## 6.2 Future Work

The work performed throughout this thesis can be complemented with further specific studies to clarify unexplained observations. Several suggestions for future investigations suggesting improvements to the current experimental system can greatly increase the value of the obtained data, as well as studies with other molecular targets can greatly increase the scientific contribution.

Regarding the  $K^-$ -molecule collisions experiments, it will be interesting to probe new molecular targets in the follow-up of the present results, such as nimorazole, misonidazole, etanidazole and EF5, which belong to the family of nitroimidazoles and are under investigation as possible radiosensitizer agents. In order to fully understand the influence of the nitro group in molecules of biological relevance, it will be also pertinent to study nitrobenzene molecule in atom-molecule collisions. Theoretical calculations involving the presence of  $K^+$  in the vicinity of the molecular target in the case of nitroimidazole studies should also be implemented to help uncovering particular underlying molecular mechanisms about the parent anion formation in particular at high-collision

energies. It will be also important to perform kinetic energy loss of the potassium cationic beam after electron transfer for collisions with nitroimidazoles, similarly to the case of pyrimidine. Unfortunately, the energy loss analyser implemented in the setup does not respond properly to working temperatures above room temperature, since most of the nitroimidazoles molecules need to be heated inside the collision chamber in order to be brought into the gas-phase with a reasonable density for these experiments.

In the case of ion-molecule experiments, future improvements and comprehensive work exploring the mechanism in anion-molecule collisions, especially through energy loss experiments are mandatory to help interpreting the interaction processes involved in these type of collisions as well as relevant theoretical contribution to further our knowledge about these processes. Additionally, the novel experimental relative cross-section values for the production of positive and negative ions presented in this study will require further measurements in order to cover a broader impact energy range and improve the statistical uncertainty

# REFERENCES

- [1] L.A. Torre, F. Bray, R. Siegel, J. Ferlay, J. Lortet-Tieulent, A. Jemal, Global Cancer Statistics, 2012, *CA Cancer J Clin.* 65 (2015) 87–108. doi:10.3322/caac.21262.
- [2] F. Bray, J. Ferlay, I. Soerjomataram, R.L. Siegel, L.A. Torre, A. Jemal, Global Cancer Statistics 2018: GLOBOCAN Estimates of Incidence and Mortality Worldwide for 36 Cancers in 185 Countries, *CA Cancer J Clin.* 68 (2018) 394–424. doi:10.3322/caac.21492.
- [3] World Health Organization (WHO), Cancer, (2018). <https://www.who.int/en/news-room/fact-sheets/detail/cancer>.
- [4] Direção-Geral de Saúde, A Saúde dos Portugueses 2016, *A Saúde Dos Port.* 2016. (2017) 177. doi:ISSN: 2183-5888.
- [5] Direção-Geral de Saúde, Doenças Oncológicas em Números 2015 - Programa Nacional para as Doenças Oncológicas, Dgs. (2016) 5–65. doi:ISSN: 2183-0746.
- [6] P. Irigaray, J.A. Newby, R. Clapp, L. Hardell, V. Howard, L. Montagnier, S. Epstein, D. Belpomme, Lifestyle-related factors and environmental agents causing cancer: An overview, *Biomed. Pharmacother.* 61 (2007) 640–658. doi:10.1016/j.biopha.2007.10.006.
- [7] P. Anand, A.B. Kunnumakara, C. Sundaram, K.B. Harikumar, S.T. Tharakan, O.S. Lai, B. Sung, B.B. Aggarwal, Cancer is a preventable disease that requires major lifestyle changes, *Pharm. Res.* 25 (2008) 2097–2116. doi:10.1007/s11095-008-9661-9.
- [8] L.N. Kolonel, D. Altshuler, B.E. Henderson, The multiethnic cohort study: Exploring genes, lifestyle and cancer risk, *Nat. Rev. Cancer.* 4 (2004) 519–527. doi:10.1038/nrc1389.
- [9] M. Charles, UNSCEAR Report 2000: Sources and Effects of Ionizing Radiation, *J. Radiol. Prot.* 21 (2001) 83–85. doi:10.1088/0952-4746/21/1/609.
- [10] B. Nilsson, A. Brahme, *Interaction of Ionizing Radiation with Matter*, Elsevier B.V., 2014. doi:10.1016/B978-0-444-53632-7.00920-5.
- [11] E.B. Podgorsak, *Biological and Medical Physics, Biomedical Engineering*, 2nd ed., Springer-Verlag Berlin Heidelberg, 2010. doi:10.1007/978-3-642-00875-7.
- [12] H. Nikjoo, S. Uehara, D. Emfietzoglou, *Interaction of Radiation with Matter*, Taylor & Francis, 2012.
- [13] H. Matsumoto, M. Tomita, K. Otsuka, M. Hatashita, A New Paradigm in Radioadaptive Response Developing from Microbeam Research, *J. Radiat. Res.* 50 (2009) A67–A79. doi:10.1269/jrr.09003S.
- [14] O. Desouky, N. Ding, G. Zhou, Targeted and non-targeted effects of ionizing radiation, *J. Radiat. Res. Appl. Sci.* 8 (2015) 247–254. doi:10.1016/j.jrras.2015.03.003.
- [15] NRC, *Health Risks from Exposure to Low Levels of Ionizing Radiation - BEIR VII Phase 2*, 2006. doi:10.17226/11340.

- [16] C.J. Martin, D.G. Sutton, C.M. West, E.G. Wright, The radiobiology/radiation protection interface in healthcare, *J. Radiol. Prot.* 29 (2009). doi:10.1088/0952-4746/29/2A/S01.
- [17] R.E. Shore, H.L. Beck, J.D. Boice, E.A. Caffrey, S. Davis, H.A. Grogan, F.A. Mettler, R.J. Preston, J.E. Till, R. Wakeford, L. Walsh, L.T. Dauer, Implications of Recent Epidemiologic Studies for the Linear Nonthreshold Model and Radiation Protection, *J Radiol Prot.* 38 (2018) 1217–1233. doi:10.1088/1361-6498/aad348.
- [18] E. Cardis, M. Vrijheid, M. Blettner, E. Gilbert, M. Hakama, C. Hill, G. Howe, J. Kaldor, C.R. Muirhead, M. Schubauer-Berigan, T. Yoshimura, F. Bermann, G. Cowper, J. Fix, C. Hacker, B. Heinmiller, M. Marshall, I. Thierry-Chef, D. Utterback, Y.O. Ahn, E. Amoros, P. Ashmore, A. Auvinen, J.M. Bae, J. Bernar Solano, A. Biau, E. Combalot, P. Deboodt, A. Diez Sacristan, M. Eklof, H. Engels, G. Engholm, G. Gulis, R. Habib, K. Holan, H. Hyvonen, A. Kerekes, J. Kurtinaitis, H. Malke, M. Martuzzi, A. Mastauskas, A. Monnet, M. Moser, M.S. Pearce, D.B. Richardson, F. Rodriguez-Artalejo, A. Rogel, H. Tardy, M. Telle-Lamberton, I. Turai, M. Usel, K. Veress, Risk of cancer after low doses of ionising radiation - Retrospective cohort study in 15 countries, *Br. Med. J.* 331 (2005) 77–80. doi:10.1136/bmj.38499.599861.E0.
- [19] K. Kamiya, K. Ozasa, S. Akiba, O. Niwa, K. Kodama, N. Takamura, E.K. Zaharieva, Y. Kimura, R. Wakeford, Long-term effects of radiation exposure on health, *Lancet.* 386 (2015) 469–478. doi:10.1016/S0140-6736(15)61167-9.
- [20] N. Journy, I. Mansouri, R.S. Allodji, C. Demoor-Goldschmidt, D. Ghazi, N. Haddy, C. Rubino, C. Veres, W.S. Zrafi, S. Rivera, I. Diallo, F. De Vathaire, Volume effects of radiotherapy on the risk of second primary cancers: A systematic review of clinical and epidemiological studies, *Radiother. Oncol.* (2018). doi:10.1016/j.radonc.2018.09.017.
- [21] D.J. Brenner, R. Doll, D.T. Goodhead, E.J. Hall, C.E. Land, J.B. Little, J.H. Lubin, D.L. Preston, R.J. Preston, J.S. Puskin, E. Ron, R.K. Sachs, J.M. Samet, R.B. Setlow, M. Zaider, Cancer risks attributable to low doses of ionizing radiation: Assessing what we really know, *PNAS.* 100 (2003) 13761–13766. doi:10.1073/pnas.2235592100.
- [22] D.J. Shah, R.K. Sachs, D.J. Wilson, Radiation-induced cancer: A modern view, *Br. J. Radiol.* 85 (2012) 1166–1173. doi:10.1259/bjr/25026140.
- [23] H. Nikjoo, P. O'Neill, D.T. Goodhead, M. Terrissol, Computational modelling of low-energy electron-induced DNA damage by early physical and chemical events, *Int. J. Radiat. Biol.* 71 (1997) 467–483.
- [24] D.T. Goodhead, Initial Events in the Cellular Effects of Ionizing Radiations: Clustered Damage in DNA, *Int. J. Radiat. Biol.* 65 (1994).
- [25] D.T. Goodhead, J. Thacker, R. Cox, Effects of radiations of different qualities on cells: Molecular mechanisms of damage and repair, *Int. J. Radiat. Biol.* 63 (1993) 543–556. doi:10.1080/09553009314450721.
- [26] J.B. Little, Ionizing Radiation, in: *Holl. Frei Cancer Med.*, 15th ed., Hamilton (ON): B. C. Decker Inc.,

- 2000: p. 207.
- [27] P. Swiderek, Fundamental Processes in Radiation Damage of DNA, *Angew. Chem. Int. Ed.* 45 (2006) 4056–4059. doi:10.1002/anie.200600614.
- [28] S. Uehara, H. Nikjoo, D. Goodhead, Comparison and Assessment of Electron Cross-sections for Monte Carlo Track Structure Codes, *Radiat. Res.* 152 (1999) 202–213. doi:10.2307/3580095.
- [29] V. Cobut, Y. Frongillo, J.P. Patau, T. Goulet, M.J. Fraser, J.P. Jay-Gerin, Monte Carlo simulation of fast electron and proton tracks in liquid water - I. Physical and physicochemical aspects, *Radiat. Phys. Chem.* 51 (1998) 229–243. doi:10.1016/S0969-806X(97)00096-0.
- [30] E. Alizadeh, L. Sanche, Precursors of solvated electrons in radiobiological physics and chemistry, *Chem. Rev.* 112 (2012) 5578–5602. doi:10.1021/cr300063r.
- [31] M. Neustetter, J. Aysina, F.F. Da Silva, S. Denifl, The Effect of Solvation on Electron Attachment to Pure and Hydrated Pyrimidine Clusters, *Angew. Chemie - Int. Ed.* 54 (2015) 9124–9126. doi:10.1002/anie.201503733.
- [32] F. Blanco, A. Muñoz, D. Almeida, F.F. Da Silva, P. Limão-Vieira, M.C. Fuss, A.G. Sanz, G. García, Modelling low energy electron and positron tracks in biologically relevant media, *Eur. Phys. J. D.* 67 (2013) 1–18. doi:10.1140/epjd/e2013-40276-1.
- [33] S. Denifl, T.D. Mark, P. Scheier, The Role of Secondary Electrons in Radiation Damage, in: G. García Gómez-Tejedor, M.C. Fuss (Eds.), *Radiat. Damage Biomol. Syst.*, 1st ed., Springer Netherlands, 2012: pp. 45–58. doi:10.1007/978-94-007-2564-5.
- [34] E. Illenberger, J. Mominy, *Gaseous Molecular Ions*, 1st ed., Steinkopff-Verlag Heidelberg, 1992. doi:10.1007/978-3-662-07383-4.
- [35] S. Denifl, P. Sulzer, D. Huber, F. Zappa, M. Probst, T.D. Märk, P. Scheier, N. Injan, J. Limtrakul, R. Abouaf, H. Dunet, Influence of functional groups on the site-selective dissociation of adenine upon low-energy electron attachment, *Angew. Chemie - Int. Ed.* 46 (2007) 5238–5241. doi:10.1002/anie.200700032.
- [36] B.D. Michael, P.O. Neill, A Sting in the Tail of Electron Tracks, *Science.* 287 (2000) 1603–1604. doi:10.1126/science.287.5458.1603.
- [37] B. Boudaïffa, P. Cloutier, D. Hunting, M.A. Huels, L. Sanche, Resonant formation of DNA strand breaks by low-energy (3 to 20 eV) electrons., *Science.* 287 (2000) 1658–60. doi:10.1126/science.287.5458.1658.
- [38] M.A. Huels, B. Boudaïffa, P. Cloutier, D. Hunting, L. Sanche, Single, double, and multiple double strand breaks induced in DNA by 3-100 eV electrons, *J. Am. Chem. Soc.* 125 (2003) 4467–4477. doi:10.1021/ja029527x.
- [39] I. Bald, J. Kopyra, E. Illenberger, Selective excision of C5 from D-ribose in the gas phase by low-energy electrons (0-1 eV): implications for the mechanism of DNA damage, *Angew. Chem., Int. Ed. Engl.* 45 (2006) 4851–5. doi:10.1002/anie.200600303.

- [40] S. Ptasińska, S. Denifl, P. Scheier, T.D. Märk, Inelastic electron interaction (attachment/ionization) with deoxyribose, *J. Chem. Phys.* 120 (2004) 8505–8511. doi:10.1063/1.1690231.
- [41] H. Abdoul-Carime, S. Gohlke, E. Illenberger, Site-specific dissociation of DNA bases by slow electrons at early stages of irradiation, *Phys. Rev. Lett.* 92 (2004) 1–4. doi:10.1103/PhysRevLett.92.168103.
- [42] S. Ptasińska, S. Denifl, B. Mróz, M. Probst, V. Grill, E. Illenberger, P. Scheier, T.D. Märk, Bond selective dissociative electron attachment to thymine, *J. Chem. Phys.* 123 (2005). doi:10.1063/1.2035592.
- [43] K. Tanzer, L. Feketeová, B. Puschnigg, P. Scheier, E. Illenberger, S. Denifl, Reactions in Nitroimidazole Triggered by Low-Energy (0-2 eV) Electrons: Methylation at N1-H Completely Blocks Reactivity., *Angew. Chem. Int. Ed. Engl.* 53 (2014) 12240–3. doi:10.1002/anie.201407452.
- [44] R. Balog, E. Illenberger, Complete chemical transformation of a molecular film by subexcitation electrons (<3 eV), *Phys. Rev. Lett.* 91 (2003) 2–5. doi:10.1103/PhysRevLett.91.213201.
- [45] P.-C. Dugal, H. Abdoul-Carime, L. Sanche, Mechanisms for Low-Energy (0.5-30 eV) Electron-Induced Pyrimidine Ring Fragmentation within Thymine- and Halogen-Substituted Single Strands of DNA, *J. Phys. Chem. B.* 104 (2000) 5610–5617. doi:10.1021/jp9938112.
- [46] L. Ellis-Gibbings, A.D. Bass, P. Cloutier, G. García, L. Sanche, Electron stimulated desorption from condensed pyrimidine and pyridazine, *Phys. Chem. Chem. Phys.* 19 (2017) 13038–13048. doi:10.1039/c7cp00715a.
- [47] E. Alizadeh, A.G. Sanz, G. García, L. Sanche, Radiation Damage to DNA: The Indirect Effect of Low Energy Electrons., *J. Phys. Chem. Lett.* 4 (2013) 820–825. doi:10.1021/jz4000998.
- [48] S. Ptasińska, L. Sanche, Dissociative electron attachment to hydrated single DNA strands, *Phys. Rev. E.* 75 (2007) 031915. doi:10.1103/PhysRevE.75.031915.
- [49] M. Smyth, J. Kohanoff, Excess Electron Localization in Solvated DNA Bases, *Phys Rev Lett.* 106 (2011) 238108. doi:10.1103/PhysRevLett.106.238108.
- [50] L. Turi, P.J. Rossky, Theoretical studies of spectroscopy and dynamics of hydrated electrons, *Chem. Rev.* 112 (2012) 5641–5674. doi:10.1021/cr300144z.
- [51] C. Wang, J. Nguyen, Q. Lu, Bond Breaks of Nucleotides by Dissociative Electron Transfer of Nonequilibrium Prehydrated Electrons: A New Molecular Mechanism for Reductive DNA Damage, *J. Am. Chem. Soc.* 131 (2009) 11320–11322. doi:10.1021/ja902675g.
- [52] I. Baccarelli, I. Bald, F.A. Gianturco, E. Illenberger, J. Kopyra, Electron-induced damage of DNA and its components: Experiments and theoretical models, *Phys. Rep.* 508 (2011) 1–44. doi:10.1016/j.physrep.2011.06.004.
- [53] R.A. Crowell, D.M. Bartels, Multiphoton Ionization of Liquid Water with 3.0 - 5.0 eV Photons, *J Phys Chem.* 100 (1996) 17940–17949. doi:10.1021/jp9610978.
- [54] C. von Sonntag, Formation of Reactive Free Radicals in an Aqueous Environment, in: *Free. DNA*

- Damage Its Repair, Springer, Berlin, Heidelberg, 2006: pp. 7–46. doi:10.1007/3-540-30592-0.
- [55] J.T. Hancock, R. Desikan, S.J. Neill, Role of reactive oxygen species in cell signalling pathways, *Biochem. Soc. Trans.* 29 (2001) 345–349. doi:10.1042/bst0290345.
- [56] E.I. Azzam, J.P. Jay-Gerin, D. Pain, Ionizing radiation-induced metabolic oxidative stress and prolonged cell injury, *Cancer Lett.* 327 (2012) 48–60. doi:10.1016/j.canlet.2011.12.012.
- [57] G. Waris, H. Ahsan, Reactive oxygen species: role in the development of cancer and various chronic conditions, *J. Carcinog.* 5 (2006) 1–8. doi:10.1186/1477-3163-5-14.
- [58] A.T. Dharmaraja, Role of Reactive Oxygen Species (ROS) in Therapeutics and Drug Resistance in Cancer and Bacteria, *J Med Chem.* 60 (2017) 3221–3240. doi:10.1021/acs.jmedchem.6b01243.
- [59] J.N. Moloney, T.G. Cotter, ROS signalling in the biology of cancer, *Semin. Cell Dev. Biol.* 80 (2017) 1–15. doi:10.1016/j.semcdb.2017.05.023.
- [60] L. Sanche, Beyond radical thinking, *Nature.* 461 (2009) 358–359. doi:10.1038/ng.447.
- [61] D.A.F. de Almeida, The role of electron transfer in DNA building blocks : evaluation of strand breaks and their implications, Universidade Nova de Lisboa, 2013.
- [62] R. Antunes, The Role of Halouracils in Radiotherapy Studied by Electron Transfer in Atom-Molecule Collisions Experiments, Universidade Nova de Lisboa, 2011.
- [63] A.W. Kleyn, A.M.C. Moutinho, Negative ion formation in alkali-atom – molecule collisions, *J Phys B At. Mol. Opt. Phys.* 34 (2001) R1–R44. doi:10.1088/0953-4075/34/14/201.
- [64] P. Limão-Vieira, F. Ferreira da Silva, G. Gómez-Tejedor, Electron Transfer-Induced Fragmentation in (Bio)Molecules by Atom-Molecule Collisions, in: G. García Gómez-Tejedor, M.C. Fuss (Eds.), *Radiat. Damage Biomol. Syst.*, Springer, 2012: pp. 59–70.
- [65] M.M. Hubers, A.W. Kleyn, J. Los, Ion Pair Formation in Alkali-Halogen Collisions at High Velocities, *Chem. Phys.* 17 (1976) 303–325. doi:10.1016/S0301-0104(76)80034-1.
- [66] R. Antunes, D. Almeida, G. Martins, N.J. Mason, G. García, M.J.P. Maneira, Y. Nunes, P. Limão-Vieira, Negative ion formation in potassium-nitromethane collisions, *Phys. Chem. Chem. Phys.* 12 (2010) 12513–9. doi:10.1039/c004467a.
- [67] F.F. Da Silva, J. Rafael, T. Cunha, D. Almeida, P. Limão-vieira, Electron transfer to aliphatic amino acids in neutral potassium collisions, *Int. J. Mass Spectrom.* 365–366 (2014) 238–242. doi:10.1016/j.ijms.2014.01.003.
- [68] F.F. Da Silva, M. Lança, D. Almeida, G. García, P. Limão-Vieira, Anionic fragmentation of glycine upon potassium-molecule collisions, *Eur. Phys. J. D.* 66 (2012). doi:10.1140/epjd/e2012-20751-y.
- [69] P. Limão-Vieira, A.M.C. Moutinho, J. Los, Dissociative ion-pair formation in collisions of fast potassium atoms with benzene and fluorobenzene., *J. Chem. Phys.* 124 (2006) 054306. doi:10.1063/1.2161217.
- [70] D. Almeida, F. Ferreira Da Silva, G. García, P. Limão-Vieira, Selective bond cleavage in potassium

- collisions with pyrimidine bases of DNA, *Phys. Rev. Lett.* 110 (2013) 1–5. doi:10.1103/PhysRevLett.110.023201.
- [71] D. Almeida, D. Kinzel, F. Ferreira da Silva, B. Puschnigg, D. Gschliesser, P. Scheier, S. Denifl, G. García, L. González, P. Limão-Vieira, N-site de-methylation in pyrimidine bases as studied by low energy electrons and ab initio calculations., *Phys. Chem. Chem. Phys.* 15 (2013) 11431–40. doi:10.1039/c3cp50548k.
- [72] D. Almeida, F.F. da Silva, G. García, P. Limão-Vieira, Dynamic of negative ions in potassium-D-ribose collisions, *J. Chem. Phys.* 139 (2014) 114304. doi:10.1063/1.4820949.
- [73] D. Almeida, F. Ferreira Da Silva, S. Eden, G. García, P. Limão-Vieira, New fragmentation pathways in K-THF collisions as studied by electron-transfer experiments: Negative ion formation, *J. Phys. Chem. A.* 118 (2014) 690–696. doi:10.1021/jp407997w.
- [74] D. Almeida, F. Ferreira da Silva, J. Kopyra, G. García, P. Limão-vieira, Anion formation in gas-phase potassium–uridine collisions, *Int. J. Mass Spectrom.* 365–366 (2014) 243–247. doi:10.1016/j.ijms.2014.01.023.
- [75] D. Almeida, R. Antunes, G. Martins, S. Eden, F. Ferreira da Silva, Y. Nunes, G. Garcia, P. Limão-Vieira, Electron transfer-induced fragmentation of thymine and uracil in atom-molecule collisions, *Phys. Chem. Chem. Phys.* 13 (2011) 15657–15665. doi:10.1039/c1cp21340g.
- [76] S. Ramachandran, J. Ient, E.-L. Göttgens, A. Krieg, E. Hammond, Epigenetic Therapy for Solid Tumors: Highlighting the Impact of Tumor Hypoxia, *Genes (Basel)*. 6 (2015) 935–956. doi:10.3390/genes6040935.
- [77] J. Overgaard, Hypoxic Radiosensitization: Adored and Ignored, *J. Clin. Oncol.* 25 (2007) 4066–4074. doi:10.1200/JCO.2007.12.7878.
- [78] P. Wardman, Chemical Radiosensitizers for Use in Radiotherapy, *Clin. Oncol.* 19 (2007) 397–417. doi:10.1016/j.clon.2007.03.010.
- [79] J. Overgaard, H.S. Hansen, M. Overgaard, L. Bastholt, A. Berthelsen, L. Specht, B. Lindeløv, K. Jørgensen, A randomized double-blind phase III study of nimorazole as a hypoxic radiosensitizer of primary radiotherapy in supraglottic larynx and pharynx carcinoma. Results of the Danish Head and Neck Cancer Study (DAHANCA) Protocol 5-85, *Radiother. Oncol.* 46 (1998) 135–146. doi:10.1016/S0167-8140(97)00220-X.
- [80] J. Overgaard, Hypoxic modification of radiotherapy in squamous cell carcinoma of the head and neck - A systematic review and meta-analysis, *Radiother. Oncol.* 100 (2011) 22–32. doi:10.1016/j.radonc.2011.03.004.
- [81] L. Feketeová, A.L. Albright, B.S. Sørensen, M.R. Horsman, J. White, R.A.J. O’Hair, N. Bassler, Formation of radical anions of radiosensitizers and related model compounds via electrospray ionization, *Int. J. Mass Spectrom.* 365–366 (2014) 56–63. doi:10.1016/j.ijms.2013.12.014.
- [82] L. Feketeová, O. Plekan, M. Goonewardane, M. Ahmed, A.L. Albright, J. White, R.A.J. O’Hair, M.R.



- Horsman, F. Wang, K.C. Prince, Photoelectron Spectra and Electronic Structures of the Radiosensitizer Nimorazole and Related Compounds, *J. Phys. Chem. A.* 119 (2015) 9986–9995. doi:10.1021/acs.jpca.5b05950.
- [83] L. Feketeová, J. Postler, A. Zavras, P. Scheier, S. Denifl, R.A.J. O’Hair, Decomposition of nitroimidazole ions: experiment and theory., *Phys. Chem. Chem. Phys.* 17 (2015) 12598–607. doi:10.1039/c5cp01014d.
- [84] K. Tanzer, L. Feketeová, B. Puschnigg, P. Scheier, E. Illenberger, S. Denifl, Reactions in Nitroimidazole and Methylnitroimidazole Triggered by Low-Energy (0-8 eV) Electrons, *J. Phys. Chem. A.* 119 (2015) 6668–6675. doi:10.1021/acs.jpca.5b02721.
- [85] Z. Yu, E.R. Bernstein, Experimental and theoretical studies of the decomposition of new imidazole based energetic materials: Model systems, *J. Chem. Phys.* 137 (2012) 114303. doi:10.1063/1.4752654.
- [86] H. Abdoul-Carime, P. Limão-Vieira, S. Gohlke, I. Petrushko, N.J. Mason, E. Illenberger, Sensitization of 5-bromouridine by slow electrons, *Chem. Phys. Lett.* 393 (2004) 442–447. doi:10.1016/j.cplett.2004.06.081.
- [87] F. Ferreira da Silva, D. Almeida, R. Antunes, G. Martins, Y. Nunes, S. Eden, G. Garcia, P. Limão-Vieira, Electron transfer processes in potassium collisions with 5-fluorouracil and 5-chlorouracil, *Phys. Chem. Chem. Phys.* 13 (2011) 21621–21629. doi:10.1039/c1cp22644d.
- [88] T. Sommerfeld, Electron-induced Chemistry of 5-Chlorouracil, *ChemPhysChem.* 2 (2001) 677–679. doi:10.1002/1439-7641(20011119)2:11<677::AID-CPHC677>3.0.CO;2-C.
- [89] E. Alizadeh, S. Ptasińska, L. Sanche, Transient Anions in Radiobiology and Radiotherapy : From Gaseous Biomolecules to Condensed Organic and Biomolecular Solids, in: W.A. Monteiro (Ed.), *Radiat. Eff. Mater.*, INTECH, 2016. doi:10.5772/63293.
- [90] A.W. Kleyn, *Vibronic Excitation in Atom Molecule Collisions*, University of Amsterdam, 1980.
- [91] A.W. Kleyn, J. Los, E.A. Gislason, Vibronic Coupling At Intersections of Covalent and Ionic States, *Phys. Reports (Review Sect. Phys. Lett.* 90 (1982) 1–71. doi:10.1016/0370-1573(82)90092-8.
- [92] A.P.M. Baede, Charge transfer between neutrals at hyperthermal energies, *Adv. Chem. Phys.* 30 (1975) 463–535.
- [93] T.D. Mark, Ionization of Molecules by Electron Impact, in: L.G. Christophorou (Ed.), *Electron - Mol. Their Appl.* Vol. 1, ACADEMIC PRESS, INC., 1984: pp. 251–334.
- [94] J.A. Aten, J. Los, Space charge related energy deficit in beams from charge exchange sources, *J. Phys. E.* 8 (1975) 408–410. doi:10.1088/0022-3735/8/5/022.
- [95] E. Alizadeh, F. Ferreira da Silva, F. Zappa, A. Mauracher, M. Probst, S. Denifl, A. Bacher, T.D. Märk, P. Limão-Vieira, P. Scheier, Dissociative electron attachment to nitromethane, *Int. J. Mass Spectrom.* 271 (2008) 15–21. doi:10.1016/j.ijms.2007.11.004.
- [96] R.L. Champion, *Collisional Detachment of Negative Ions*, 1982. doi:10.1016/S0065-2539(08)61023-9.

- [97] V.N. Tuan, V.A. Esaulov, Electron detachment via direct coupling and charge exchange to shape resonances in negative-ion-molecule collisions, *J. Phys. B At. Mol. Phys.* 15 (1982). doi:10.1088/0022-3700/15/3/009.
- [98] D. Almeida, R. Antunes, G. Martins, G. Garcia, R.W. McCullough, S. Eden, P. Limão-Vieira, Mass spectrometry of anions and cations produced in 1-4 keV H-, O-, and OH- collisions with nitromethane, water, ethanol, and methanol, *Int. J. Mass Spectrom.* 311 (2012) 7–16. doi:10.1016/j.ijms.2011.11.009.
- [99] F. Rahman, B. Hird, Electron detachment atomic cross-sections from negative ions, *At. Data Nucl. Data Tables.* 35 (1986) 123–183. doi:10.1016/0092-640X(86)90029-X.
- [100] V.N. Tuan, V. Esaulov, J.P. Gauyacq, Charge exchange to a shape resonance in H–CO<sub>2</sub> collisions: Evidence of a non-Franck-Condon behaviour, *J. Phys. B At. Mol. Phys.* 17 (1984). doi:10.1088/0022-3700/17/5/005.
- [101] V. Ngoc Tuan, J.P. Gauyacq, V.A. Esaulov, On the impact parameter dependence of detached electron energy spectra in H–He collisions, *J. Phys. B At. Mol. Phys.* 16 (1983). doi:10.1088/0022-3700/16/4/002.
- [102] V.N. Tuan, V.A. Esaulov, J.P. Grouard, R.I. Hall, J.L. Montmagnon, Electron detachment and charge exchange to shape resonances in F- - molecule collisions, *J. Phys. B At. Mol. Opt. Phys.* 17 (1984) 2897–2912. doi:10.1088/0022-3700/17/14/018.
- [103] Vu Ngoc Tuan, V. Esaulov, J.P. Gauyacq, A. Herzenberg, Electron detachment in H--molecule collisions, *J. Phys. B At. Mol. Phys.* 18 (1985) 721–735. doi:10.1088/0022-3700/18/4/017.
- [104] T. Okamoto, Y. Sato, H. Inouye, Electron Detachment via Charge Transfer to Shape Resonances in H- - O<sub>2</sub> and H- - NO Collisions, *Phys Rev Lett.* 52 (1984) 184–187.
- [105] J.S. Risley, Excitation and decay of vibrational autodetaching states of N<sub>2</sub>- produced in collisions of H- and N<sub>2</sub>, *Phys. Rev. A.* 16 (1977) 2346. doi:10.1103/PhysRevA.16.2346.
- [106] B.K. Annis, S. Datz, R.L. Champion, L.D. Doverspike, Role of negative-molecular-ion resonances in collisional detachment: Cl+N<sub>2</sub>, *Phys. Rev. Lett.* 45 (1980) 1554–1557. doi:10.1103/PhysRevLett.45.1554.
- [107] R.L. Champion, L.D. Doverspike, Collisional detachment in collisions of Cl- with the rare gases, *Phys. Rev. A.* 13 (1976) 609–616. doi:10.1103/PhysRevA.13.609.
- [108] J.B. Hasted, Inelastic Collisions between Ions and Atoms, *Proc. R. Soc. A Math. Phys. Eng. Sci.* 212 (1952) 235–248. doi:10.1098/rspa.1952.0078.
- [109] J.B. Hasted, R.A. Smith, The Detachment of Electrons from Negative Ions, *Proc. R. Soc. A Math. Phys. Eng. Sci.* 235 (1956) 349–353. doi:10.1098/rspa.1956.0087.
- [110] R.A. Bennett, Electron loss cross-sections for O-, O-<sub>2</sub>, NO-<sub>2</sub>, and NO-<sub>3</sub> in several gases, *J. Chem. Phys.* 62 (1975) 2223. doi:10.1063/1.430744.
- [111] R.N. Compton, T.L. Bailey, Electron Detachment in Collisions of Low-Energy O- Ions with N<sub>2</sub>, *J. Chem. Phys.* 53 (1970) 454–456. doi:10.1063/1.1673808.

- [112] J.P. Doering, 1- to 10-keV Collisional Detachment Cross-sections for  $O^-$  and  $O_2^-$  on Argon and Nitrogen, *J. Chem. Phys.* 41 (1964) 1164–1165. doi:10.1063/1.1726030.
- [113] M. Matic, B. Cobic, Electron loss by C- and O- ions in gaseous targets, *J. Phys. B At. Mol. Phys.* 4 (1971) 111–115. doi:10.1088/0022-3700/4/1/015.
- [114] R. Ranjan, C.C. Goodyear, Collisional detachment from atmospheric negative ions, *J. Phys. B At. Mol. Phys.* 6 (1973) 1070–1078. doi:10.1088/0022-3700/6/6/021.
- [115] G. Jalbert, R.F. Nascimento, C.R. De Carvalho, C.R. Carvalho, B.F. Magnani, A.C.F. Santos, A.B. Rocha, M.M.S. Anna, N.V.D.C. Faria, Electron-detachment cross-section for  $CN^-$  and  $O_2^-$  incident on  $N_2$  at intermediate velocities, *Phys. Rev. A.* 89 (2014) 1–5. doi:10.1103/PhysRevA.89.012712.
- [116] G. Jalbert, W. Wolff, S.D. Magalhães, N. V. De Castro Faria, Electron detachment of negative ions: The influence of the outermost electron and its neutral core atom in collision with He, Ne, and Ar, *Phys. Rev. A - At. Mol. Opt. Phys.* 77 (2008) 1–8. doi:10.1103/PhysRevA.77.012722.
- [117] N. V. de Castro Faria, M.M. Sant’Anna, C. Carvalho, G. Jalbert, L.F.S. Coelho, B.F. Magnani, F. Zappa, Negative Ions and Their Behavior in Collisions, *Int. J. Quantum Chem.* 111 (2011) 1836–1842. doi:10.1002/qua.22843.
- [118] A.L.F. de Barros, S. Martínez, F. Zappa, S. Suárez, G. Bernardi, G. Jalbert, L.F.S. Coelho, N. V. de Castro Faria,  $H_2$  and  $N_2$  ionization and dissociative ionization by  $C^-$  and  $O^-$  ions at intermediate velocities: Direct and electron loss channels, *Phys. Rev. A.* 72 (2005) 032708. doi:10.1103/PhysRevA.72.032708.
- [119] F. Zappa, A.L.F. De Barros, L.F.S. Coelho, G. Jalbert, S.D. Magalhães, N. V. De Castro Faria, Ionization of helium by impact of negative B, O, and F ions, *Phys. Rev. A - At. Mol. Opt. Phys.* 70 (2004) 1–4. doi:10.1103/PhysRevA.70.034701.
- [120] T.M. da F. Cunha, Negative Ion Formation in Potassium-Purine Molecules collisions, Universidade Nova de Lisboa, 2018.
- [121] W.C. Wiley, I.H. McLaren, Time-of-flight mass spectrometer with improved resolution, *Rev. Sci. Instrum.* 26 (1955) 1150–1157. doi:10.1063/1.1715212.
- [122] G.J.M. Hagelaar, D.B. Mihailova, J. Van Dijk, Analytical model of a longitudinal hollow cathode discharge, *J. Phys. D. Appl. Phys.* 43 (2010). doi:10.1088/0022-3727/43/46/465204.
- [123] R.R. Arslanbekov, A.A. Kudryavtsev, R.C. Tobin, On the hollow-cathode effect: Conventional and modified geometry, *Plasma Sources Sci. Technol.* 7 (1998) 310–322. doi:10.1088/0963-0252/7/3/009.
- [124] S. Hashiguchi, M. Hasikuni, Theory of the hollow cathode glow discharge, *Jpn. J. Appl. Phys.* 26 (1987) 271–280. doi:10.1143/JJAP.26.271.
- [125] H. Amemiya, K. Ogawa, Characteristics of a hollow-cathode discharge containing negative ions, *J. Phys. D. Appl. Phys.* 30 (1997) 879–888. doi:10.1088/0022-3727/30/5/021.
- [126] J.C. Oller, L. Ellis-Gibbins, F.F. da Silva, P. Limão-Vieira, G. García, Novel experimental setup for time-of-flight mass spectrometry ion detection in collisions of anionic species with neutral gas-phase

- molecular targets, EPJ Tech. Instrum. 2 (2015) 13. doi:10.1140/epjti/s40485-015-0023-9.
- [127] J. Overgaard, Hypoxic modification of radiotherapy in squamous cell carcinoma of the head and neck - A systematic review and meta-analysis, *Radiother. Oncol.* 100 (2011) 22–32. doi:10.1016/j.radonc.2011.03.004.
- [128] Z. Zha, L. Zhu, Y. Liu, F. Du, H. Gan, J. Qiao, H.F. Kung, Synthesis and evaluation of two novel 2-nitroimidazole derivatives as potential PET radioligands for tumor imaging, *Nucl. Med. Biol.* 38 (2011) 501–508. doi:10.1016/j.nucmedbio.2010.11.001.
- [129] D.I. Edwards, Reduction of nitroimidazoles in vitro and DNA damage, *Biochem. Pharmacol.* 35 (1986) 53–58. doi:10.1016/0006-2952(86)90554-X.
- [130] B. Boudaïffa, P. Cloutier, D. Hunting, M.A. Huels, L. Sanche, Resonant formation of DNA strand breaks by low-energy (3 to 20 eV) electrons, *Science* (80-. ). 287 (n.d.) 1658–60. doi:10.1126/science.287.5458.1658.
- [131] D. Almeida, M.-C. Bacchus-Montabonel, F. Ferreira da Silva, G. Garcia, P. Limão-Vieira, Potassium-Uracil/Thymine Ring Cleavage Enhancement As Studied in Electron Transfer Experiments and Theoretical Calculations, *J. Phys. Chem. A.* 118 (2014) 6547–6552. doi:10.1021/jp503164a.
- [132] T. Cunha, M. Mendes, F. Ferreira Da Silva, S. Eden, G. García, P. Limão-Vieira, Communication: Site-selective bond excision of adenine upon electron transfer, *J. Chem. Phys.* 148 (2018) 021101. doi:10.1063/1.5018401.
- [133] P. Bolognesi, A.R. Casavola, A. Cartoni, R. Richter, P. Markus, S. Borocci, J. Chiarinelli, S. Tošić, H. Sa'adeh, M. Masić, B.P. Marinković, K.C. Prince, L. Avaldi, Communication: “Position” does matter: The photofragmentation of the nitroimidazole isomers, *J. Chem. Phys.* 145 (2016). doi:10.1063/1.4967770.
- [134] C. Desfrancois, H. Abdoul-Carime, S. Carles, V. Périquet, J.P. Schermann, D.M.A. Smith, L. Adamowicz, Experimental and theoretical ab initio study of the influence of N-methylation on the dipole-bound electron affinities of thymine and uracil, *J. Chem. Phys.* 110 (1999) 11876–11883. doi:10.1063/1.479175.
- [135] D. Almeida, F. Ferreira da Silva, G. García, P. Limão-Vieira, Selective bond cleavage in potassium collisions with pyrimidine bases of DNA, *Phys. Rev. Lett.* 110 (2013) 023201. doi:10.1103/PhysRevLett.110.023201.
- [136] T. Cunha, M. Mendes, F. Ferreira Da Silva, S. Eden, G. García, M.C. Bacchus-Montabonel, P. Limão-Vieira, Electron transfer driven decomposition of adenine and selected analogs as probed by experimental and theoretical methods, *J. Chem. Phys.* 148 (2018) 134301. doi:10.1063/1.5021888.
- [137] K. Tanzer, L. Feketeová, B. Puschnigg, P. Scheier, E. Illenberger, S. Denifl, Reactions in Nitroimidazole and Methylnitroimidazole Triggered by Low-Energy (0-8 eV) Electrons, *J. Phys. Chem. A.* 119 (2015) 6668–6675. doi:10.1021/acs.jpca.5b02721.
- [138] A. Ribar, K. Fink, M. Probst, S.E. Huber, L. Feketeová, S. Denifl, Isomer Selectivity in Low-Energy

- Electron Attachment to Nitroimidazoles, *Chem. - A Eur. J.* 23 (2017) 12892–12899. doi:10.1002/chem.201702644.
- [139] P. Sonveaux, B.F. Jordan, B. Gallez, O. Feron, Nitric oxide delivery to cancer: Why and how?, *Eur. J. Cancer.* 45 (2009) 1352–1369. doi:10.1016/j.ejca.2008.12.018.
- [140] D.E. Woon, T.H. Dunning, Gaussian basis sets for use in correlated molecular calculations. IV. Calculation of static electrical response properties, *J. Chem. Phys.* 100 (1994) 2975–2988. doi:10.1063/1.466439.
- [141] T.H. Dunning, Gaussian basis sets for use in correlated molecular calculations. I. The atoms boron through neon and hydrogen, *J. Chem. Phys.* 90 (1989) 1007–1023. doi:10.1063/1.456153.
- [142] R.A. Kendall, T.H. Dunning, R.J. Harrison, Electron affinities of the first-row atoms revisited. Systematic basis sets and wave functions, *J. Chem. Phys.* 96 (1992) 6796–6806. doi:10.1063/1.462569.
- [143] M. Gutowski, P. Skurski, A.I. Boldyrev, J. Simons, K.D. Jordan, Contribution of electron correlation to the stability of dipole-bound anionic states, *Phys. Rev. A - At. Mol. Opt. Phys.* 54 (1996) 1906–1909. doi:10.1103/PhysRevA.54.1906.
- [144] M. Gutowski, K.D. Jordan, P. Skurski, Electronic structure of dipole-bound anions, *J. Phys. Chem. A.* 102 (1998) 2624–2633. doi:10.1021/jp980123u.
- [145] P. Skurski, M. Gutowski, J. Simons, How to choose a one-electron basis set to reliably describe a dipole-bound anion, *Int. J. Quantum Chem.* 80 (2000) 1024–1038. doi:10.1002/1097-461X(2000)80:4/5<1024::AID-QUA51>3.0.CO;2-P.
- [146] D. Svozil, T. Frigato, Z. Havlas, P. Jungwirth, Ab initio electronic structure of thymine anions, *Phys. Chem. Chem. Phys.* 7 (2005) 840–845. doi:10.1039/b415007d.
- [147] M. Gutowski, P. Skurski, K.D. Jordan, J. Simons, Energies of dipole-bound anionic states, *Int. J. Quantum Chem.* 64 (1997) 183–191. doi:10.1002/(SICI)1097-461X(1997)64:2<183::AID-QUA5>3.0.CO;2-S.
- [148] M.J. Frisch, G.W. Trucks, H.B. Schlegel, G.E. Scuseria, M.A. Robb, J.R. Cheeseman, G. Scalmani, V. Barone, B. Mennucci, G.A. Petersson, H. Nakatsuji, M. Caricato, X. Li, H.P. Hratchian, A.F. Izmaylov, J. Bloino, G. Zheng, J.L. Sonnenberg, M. Hada, M. Ehara, K. Toyota, R. Fukuda, J. Hasegawa, M. Ishida, T. Nakajima, Y. Honda, O. Kitao, H. Nakai, T. Vreven, J.A.J. Montgomery, J.E. Peralta, F. Ogliaro, M. Bearpark, J.J. Heyd, E. Brothers, K.N. Kudin, V.N. Staroverov, T. Keith, R. Kobayashi, J. Normand, K. Raghavachari, A. Rendell, J.C. Burant, S.S. Iyengar, J. Tomasi, M. Cossi, N. Rega, J.M. Millam, M. Klene, J.E. Knox, J.B. Cross, V. Bakken, C. Adamo, J. Jaramillo, R. Gomperts, R.E. Stratmann, O. Yazyev, A.J. Austin, R. Cammi, C. Pomelli, J.W. Ochterski, R.L. Martin, K. Morokuma, V.G. Zakrzewski, G.A. Voth, P. Salvador, J.J. Dannenberg, S. Dapprich, A.D. Daniels, O. Farkas, J.B. Foresman, J. V. Ortiz, J. Cioslowski, Gaussian 09, Revision D.01, (2013).
- [149] H. Wang, X. Mu, H. He, X.D. Zhang, Cancer Radiosensitizers, *Trends Pharmacol. Sci.* 39 (2018) 24–48. doi:10.1016/j.tips.2017.11.003.

- [150] J. Overgaard, Hypoxic modification of radiotherapy in squamous cell carcinoma of the head and neck - A systematic review and meta-analysis, *Radiother. Oncol.* 100 (2011) 22–32. doi:10.1016/j.radonc.2011.03.004.
- [151] S. Pandeti, L. Feketeová, T.J. Reddy, H. Abdoul-Carime, B. Farizon, M. Farizon, T.D. Märk, Binding preference of nitroimidazolic radiosensitizers to nucleobases and nucleosides probed by electrospray ionization mass spectrometry and density functional theory, *J. Chem. Phys.* 150 (2019) 014302. doi:10.1063/1.5062604.
- [152] A. Cartoni, A.R. Casavola, P. Bolognesi, M.C. Castrovilli, D. Catone, J. Chiarinelli, R. Richter, L. Avaldi, Insights into 2- and 4(5)-Nitroimidazole Decomposition into Relevant Ions and Molecules Induced by VUV Ionization, *J. Phys. Chem. A.* 122 (2018) 4031–4041. doi:10.1021/acs.jpca.8b01144.
- [153] F. Kossoski, M.T.D.N. Varella, How does methylation suppress the electron-induced decomposition of 1-methyl-nitroimidazoles?, *J. Chem. Phys.* 147 (2017). doi:10.1063/1.5005604.
- [154] E.G. Brown, Imidazoles and benzimidazoles., in: *Ring Nitrogen Key Biomol.*, Springer, Dordrecht, 1998: pp. 40–59. doi:10.1007/978-94-011-4906-8.
- [155] M. Kumar, D. Kumar, V. Raj, Studies on Imidazole and Its Derivatives with Particular Emphasis on Their Chemical/biological Applications as Bioactive Molecules/Intermediated to Bioactive Molecule, *Curr. Synth. Syst. Biol.* 05 (2017) 1–10. doi:10.4172/2332-0737.1000135.
- [156] A. Ribar, K. Fink, Z. Li, S. Ptasinska, I. Carmichael, L. Feketeova, S. Denifl, Stripping off Hydrogens in Imidazole Triggered by the Attachment of a Single Electron, *Phys. Chem. Chem. Phys.* (2017) 6406–6415. doi:10.1039/C6CP08773F.
- [157] A. Modelli, P.D. Burrow, Electron attachment to the aza-derivatives of furan, pyrrole, and thiophene, *J. Phys. Chem. A.* 108 (2004) 5721–5726. doi:10.1021/jp048759a.
- [158] S. Carles, F. Lecomte, J.P. Schermann, C. Desfrancois, Gas-phase experimental and theoretical studies of adenine, imidazole, pyrrole, and water non-covalent complexes, *J. Phys. Chem. A.* 104 (2000) 10662–10668. doi:10.1021/jp002157j.
- [159] A.J. Gianola, T. Ichino, R.L. Hoenigman, S. Kato, V.M. Bierbaum, W.C. Lineberger, Photoelectron spectra and ion chemistry of imidazolidine, *J. Phys. Chem. A.* 109 (2005) 11504–11514. doi:10.1021/jp053566o.
- [160] R. Antunes, D. Almeida, G. Martins, N.J. Mason, G. Garcia, M.J.P. Maneira, Y. Nunes, P. Limão-Vieira, Negative ion formation in potassium–nitromethane collisions, *Phys. Chem. Chem. Phys.* 12 (2010) 12513–12519. doi:10.1039/c004467a.
- [161] M. Mendes, B. Pamplona, S. Kumar, F. Ferreira da Silva, A. Aguilar, G. García, M.-C. Bacchus-Montabonel, P. Limão-Vieira, Ion-pair formation in neutral potassium-neutral pyrimidine collisions: electron transfer experiments (submitted for publication in *Frontiers in Chemistry*), (2019).
- [162] C. Desfrancois, Determination of electron binding energies of ground-state dipole-bound molecular anions, *Phys. Rev. A.* 51 (1995) 3667. doi:10.1103/PhysRevA.51.3667.

- [163] R.N. Compton, H.S. Carman, C. Desfrancois, H. Abdoul-Carmine, J.P. Schermann, J.H. Hendricks, S.A. Lyapustina, K.H. Bowen, On the binding of electrons to nitromethane: Dipole and valence bound anions, *J. Chem. Phys.* 105 (1996) 3472–3478. doi:10.1063/1.472993.
- [164] A.W. Kleyn, A.M.C. Moutinho, Negative ion formation in alkali-atom-molecule collisions, *J Phys B.* 34 (2001).
- [165] NIST Chemistry WebBook, (2018). <http://webbook.nist.gov/chemistry/> for NIST Chemistry WebBook.
- [166] C.-R. Wang, J. Nguyen, Q.-B. Lu, Bond Breaks of Nucleotides by Dissociative Electron Transfer of Nonequilibrium Prehydrated Electrons: A New Molecular Mechanism for Reductive DNA Damage, *J. Am. Chem. Soc.* 131 (2009) 11320–11322. doi:10.1021/ja902675g.
- [167] L. Sanche, Low energy electron-driven damage in biomolecules, *Eur. Phys. J. D.* 35 (2005) 367–390. doi:10.1140/epjd/e2005-00206-6.
- [168] Y. Zheng, L. Sanche, Effective and absolute cross-sections for low-energy (1-30 eV) electron interactions with condensed biomolecules, *Appl. Phys. Rev.* 5 (2018). doi:10.1063/1.5010916.
- [169] K. Aflatooni, G.A. Gallup, P.D. Burrow, Electron attachment energies of the DNA bases, *J. Phys. Chem. A.* 102 (1998) 6205–6207. doi:10.1021/jp980865n.
- [170] F.F. Da Silva, C. Matias, D. Almeida, G. García, O. Ingólfsson, H.D. Flosadóttir, B. Ómarsson, S. Ptasinska, B. Puschnigg, P. Scheier, P. Limão-Vieira, S. Denifl, NCO-, a key fragment upon dissociative electron attachment and electron transfer to pyrimidine bases: Site selectivity for a slow decay process, *J. Am. Soc. Mass Spectrom.* 24 (2013) 1787–1797. doi:10.1007/s13361-013-0715-9.
- [171] M.A. Huels, I. Hahndorf, E. Illenberger, L. Sanche, Resonant dissociation of DNA bases by subionization electrons, *J. Chem. Phys.* 108 (1998) 1309–1312. doi:10.1063/1.475503.
- [172] I. Linert, M. Dampc, B. Mielewska, M. Zubek, Cross-sections for ionization and ionic fragmentation of pyrimidine molecules by electron collisions, *Eur. Phys. J. D.* 66 (2012). doi:10.1140/epjd/e2011-20648-3.
- [173] D. Almeida, F. Ferreira Da Silva, G. García, P. Limão-Vieira, Selective bond cleavage in potassium collisions with pyrimidine bases of DNA, *Phys. Rev. Lett.* 110 (2013) 1–5. doi:10.1103/PhysRevLett.110.023201.
- [174] S. Ptasinska, S. Denifl, V. Grill, T.D. Märk, E. Illenberger, P. Scheier, Bond- and site-selective loss of H- from pyrimidine bases, *Phys. Rev. Lett.* 95 (2005) 1–4. doi:10.1103/PhysRevLett.95.093201.
- [175] R. Pandey, M. Ryszka, T. da Fonseca Cunha, M. Lalande, M. Dampc, P. Limão-Vieira, N.J. Mason, J.C. Poully, S. Eden, Threshold behavior in metastable dissociation of multi-photon ionized thymine and uracil, *Chem. Phys. Lett.* 684 (2017) 233–238. doi:10.1016/j.cplett.2017.06.051.
- [176] I. Nenner, G.J. Schulz, Temporary negative ions and electron affinities of benzene and N-heterocyclic molecules: Pyridine, pyridazine, pyrimidine, pyrazine, and s-triazine, *J. Chem. Phys.* 62 (1975) 1747–1758. doi:10.1063/1.430700.

- [177] A. Modelli, P.D. Burrow, Electron-transmission study of the temporary anion states of substituted pyridines, *J. Electron Spectros. Relat. Phenomena.* 32 (1983) 263–276. doi:10.1016/0368-2048(83)85007-5.
- [178] A. Modelli, P. Bolognesi, L. Avaldi, Temporary anion states of pyrimidine and halopyrimidines, *J. Phys. Chem. A.* 115 (2011) 10775–10782. doi:10.1021/jp206559d.
- [179] Z. Mašín, J.D. Gorfinkiel, Effect of the third  $\pi^*$  resonance on the angular distributions for electron-pyrimidine scattering, *Eur. Phys. J. D.* 70 (2016) 151. doi:10.1140/epjd/e2016-70165-x.
- [180] M.D. Sevilla, B. Besler, A.O. Colson, Ab initio molecular orbital calculations of DNA radical ions. 5. Scaling of calculated electron affinities and ionization potentials to experimental values, *J. Phys. Chem.* 99 (1995) 1060–1063. doi:10.1021/j100003a032.
- [181] M.C. Fuss, A.G. Sanz, F. Blanco, J.C. Oiler, P. Limão-Vieira, M.J. Brunger, G. García, Total electron scattering cross-sections for pyrimidine and pyrazine as measured using a magnetically confined experimental system, *Phys. Rev. A.* 88 (2013) 042702. doi:10.1088/1742-6596/488/1/012048.
- [182] W.Y. Baek, A. Arndt, M.U. Bug, H. Rabus, M. Wang, Total electron-scattering cross-sections of pyrimidine, *Phys. Rev. A - At. Mol. Opt. Phys.* 88 (2013) 1–8. doi:10.1103/PhysRevA.88.032702.
- [183] D.B. Jones, S.M. Bellm, F. Blanco, M. Fuss, G. García, P. Limão-Vieira, M.J. Brunger, Differential cross-sections for the electron impact excitation of pyrimidine, *J. Chem. Phys.* 137 (2012). doi:10.1063/1.4743961.
- [184] D.B. Jones, S.M. Bellm, P. Limão-Vieira, M.J. Brunger, Low-energy electron scattering from pyrimidine: Similarities and differences with benzene, *Chem. Phys. Lett.* 535 (2012) 30–34. doi:10.1016/j.cplett.2012.03.044.
- [185] J.B. Maljković, A.R. Milosavljević, F. Blanco, D. Šević, G. García, B.P. Marinković, Absolute differential cross-sections for elastic scattering of electrons from pyrimidine, *Phys. Rev. A - At. Mol. Opt. Phys.* 79 (2009) 1–7. doi:10.1103/PhysRevA.79.052706.
- [186] Z. Mašín, J.D. Gorfinkiel, D.B. Jones, S.M. Bellm, M.J. Brunger, Elastic and inelastic cross-sections for low-energy electron collisions with pyrimidine, *J. Chem. Phys.* 136 (2012). doi:10.1063/1.3702629.
- [187] E. Itälä, S. Granroth, D.T. Ha, K. Kooser, H. Levola, E. Rachlew, K. Tanzer, E. Kukk, Fragmentation of imidazole, pyrimidine and purine induced by core ionization: Significance of small-scale chemical environment, *J. Photochem. Photobiol. A Chem.* 356 (2018) 283–289. doi:10.1016/j.jphotochem.2018.01.003.
- [188] W. Wolff, H. Luna, L. Sigaud, A.C. Tavares, E.C. Montenegro, Absolute total and partial dissociative cross-sections of pyrimidine at electron and proton intermediate impact velocities, *J. Chem. Phys.* 140 (2014). doi:10.1063/1.4864322.
- [189] M.N. Pisanias, L.G. Christophorou, J.G. Carter, D.L. McCorkle, Compound-negative-ion resonance states and threshold-electron excitation spectra of N-heterocyclic molecules: Pyridine, pyridazine, pyrimidine, pyrazine, and sym-triazine, *J. Chem. Phys.* 58 (1973) 2110–2124. doi:10.1063/1.1679477.



- [190] K. Regeta, M. Allan, Z. Mašin, J.D. Gorfinkiel, Absolute cross-sections for electronic excitation of pyrimidine by electron impact, *J. Chem. Phys.* 144 (2016). doi:10.1063/1.4939077.
- [191] F.F. da Silva, D. Almeida, G. Martins, a R. Milosavljević, B.P. Marinković, S. V Hoffmann, N.J. Mason, Y. Nunes, G. Garcia, P. Limão-Vieira, The electronic states of pyrimidine studied by VUV photoabsorption and electron energy-loss spectroscopy., *Phys. Chem. Chem. Phys.* 12 (2010) 6717–6731. doi:10.1039/b927412j.
- [192] P.L. Levesque, M. Michaud, L. Sanche, Absolute vibrational and electronic cross-sections for low-energy electron (2–12 eV) scattering from condensed pyrimidine, *J. Chem. Phys.* 122 (2005). doi:10.1063/1.1854121.
- [193] M.C. Fuss, L. Ellis-Gibbins, D.B. Jones, M.J. Brunger, F. Blanco, A. Muñoz, P. Limão-Vieira, G. García, The role of pyrimidine and water as underlying molecular constituents for describing radiation damage in living tissue: A comparative study, *J. Appl. Phys.* 117 (2015). doi:10.1063/1.4921810.
- [194] F.F. da Silva, G. Meneses, O. Ingólfsson, P. Limão-Vieira, Side chain effects in reactions of the potassium-tyrosine charge transfer complex, *Chem. Phys. Lett.* 662 (2016) 19–24. doi:10.1016/j.cplett.2016.08.004.
- [195] M.C. Bacchus-Montabonel, Y.S. Tergiman, Radiation damage on biomolecular systems: Dynamics of ion induced collision processes, *Comput. Theor. Chem.* 990 (2012) 177–184. doi:10.1016/j.comptc.2011.11.004.
- [196] E. Bene, Á. Vibók, G.J. Halász, M.C. Bacchus-Montabonel, Ab initio molecular treatment of charge transfer processes induced by collision of C<sub>2</sub><sup>+</sup> ions with the OH radical: A linear approach, *Chem. Phys. Lett.* 455 (2008) 159–163. doi:10.1016/j.cplett.2008.02.094.
- [197] M.C. Bacchus-Montabonel, Y.S. Tergiman, Charge transfer dynamics of carbon ions with uracil and halouracil targets at low collision energies, *Chem. Phys. Lett.* 503 (2011) 45–48. doi:10.1016/j.cplett.2011.01.013.
- [198] L. Salem, *Electrons in Chemical Reactions: First Principles*, Wiley Interscience: New York, 1982.
- [199] M.C. Bacchus-Montabonel, F. Calvo, Nanohydration of uracil: Emergence of three-dimensional structures and proton-induced charge transfer, *Phys. Chem. Chem. Phys.* 17 (2015) 9629–9633. doi:10.1039/c5cp00611b.
- [200] M.C. Bacchus-Montabonel, Y.S. Tergiman, An ab initio study of ion induced charge transfer dynamics in collision of carbon ions with thymine, *Phys. Chem. Chem. Phys.* 13 (2011) 9761–9767. doi:10.1039/c1cp20503j.
- [201] M.C. Bacchus-Montabonel, Y.S. Tergiman, Anisotropic effect in the charge transfer of C<sub>q</sub><sup>+</sup> ions with uracil, *Phys. Rev. A - At. Mol. Opt. Phys.* 74 (2006) 8–11. doi:10.1103/PhysRevA.74.054702.
- [202] H.-J. Werner, P.J. Knowles, G. Knizia, F.R. Manby, M. Schutz, P. Celani, et al, MOLPRO, version 2015.1, (2015). www.molpro.net.
- [203] A. Nicklass, M. Dolg, H. Stoll, H. Preuss, Ab initio energy-adjusted pseudopotentials for the noble

- gases Ne through Xe: Calculation of atomic dipole and quadrupole polarizabilities, *J. Chem. Phys.* 102 (1995) 8942–8952. doi:10.1063/1.468948.
- [204] J.C. Rienstra-Kiracofe, G.S. Tschumper, H.F. Schaefer, Atomic and Molecular Electron Affinities: Photoelectron Experiments and Theoretical Computations, *Chem.* 102 (2002) 231–282. doi:10.1021/cr990044u.
- [205] D.J. Lavorato, T.K. Dargel, W. Koch, G.A. McGibbon, H. Schwarz, J.K. Terlouw, Pyrimidine-ylidenes produced using neutralization-reionization mass spectrometry and probed by density functional methods, *Int. J. Mass Spectrom.* 210/211 (2001) 43–57. doi:10.1016/S1387-3806(01)00410-9.
- [206] L.C.L. Huang, O. Asvany, A.H.H. Chang, N. Balucani, S.H. Lin, Y.T. Lee, R.I. Kaiser, Crossed beam reaction of cyano radicals with hydrocarbon molecules. III. Chemical dynamics of vinyl cyanide ( $C_2H_3CN; X\ 1A'$ ) formation from reaction of  $CN(X\ 2\Sigma^+)$  with ethylene,  $C_2H_4(X\ 1Ag)$ , *J. Chem. Phys.* 113 (2000) 8656–8666. doi:10.1063/1.1289530.
- [207] B. Van Zyl, T.M. Stephen, Dissociative ionization of  $H_2$ ,  $N_2$ , and  $O_2$  by electron impact, *Phys. Rev. A.* 50 (1994) 3164–3173. doi:10.1103/PhysRevA.50.3164.
- [208] V.S. Prabhudesai, A.H. Kelkar, D. Nandi, E. Krishnakumar, Functional group dependent site specific fragmentation of molecules by low energy electrons, *Phys. Rev. Lett.* 95 (2005) 1–4. doi:10.1103/PhysRevLett.95.143202.
- [209] T. Tabata, T. Shirai, M. Sataka, H. Kubo, Analytic cross-sections for electron impact collisions with nitrogen molecules, *At. Data Nucl. Data Tables.* 92 (2006) 375–406. doi:10.1016/j.adt.2006.02.002.
- [210] F. Ferreira da Silva, D. Almeida, R. Antunes, G. Martins, Y. Nunes, S. Eden, G. Garcia, P. Limão-Vieira, Electron transfer processes in potassium collisions with 5-fluorouracil and 5-chlorouracil, *Phys. Chem. Chem. Phys.* 13 (2011) 21621–9. doi:10.1039/c1cp22644d.
- [211] C. von Sonntag, The superoxide Radical, in: D.S. Schreck (Ed.), *Free. DNA Damage Its Repair*, Springer, Berlin Heidelberg, 2006: pp. 178–194. doi:10.1007/3-540-30592-0.
- [212] J. López-Patiño, B.E. Fuentes, F.B. Yousif, H. Martínez, Low energy ionization and fragmentation cross-sections for  $H^+$  impact on  $N_2$  and  $O_2$ , *Int. J. Mass Spectrom.* 405 (2016) 59–63. doi:10.1016/j.ijms.2016.05.014.
- [213] D.T. Hall, D.F. Strobel, P.D. Feldman, M. a McGrath, H. a Weaver, Detection of an oxygen atmosphere on Jupiter's moon Europa., *Nature.* 373 (1995) 677–681. doi:10.1038/373677a0.
- [214] A.S. Yen, S.S. Kim, M.H. Hecht, M.S. Frant, B. Murray, Evidence That the Reactivity of the Martian Soil Is Due to Superoxide Ions, *Science* (80-. ). 289 (2000) 1909–1912. doi:10.1126/science.289.5486.1909.
- [215] S.L. Lin, J.N. Bardsley, D.L. Albritton, Cross-section for the reaction  $O^+ + O_2 \rightarrow O_2^+ + O$  at relative kinetic energies from threshold to 3 eV, *Int. J. Mass Spectrom. Ion Phys.* 34 (1980) 113–124.
- [216] H. Kheyrandish, D.G. Armour, E.J. Jones, The measurement of charge transfer cross-sections for a variety of ions on air and argon, *Vacuum.* 34 (1984) 269–273.

- [217] J.J. Leventhal, L. Friedman, Diatomic-Ion—Molecule Reactions:  $N_2^+-N_2$ ,  $CO^+-CO$ , and  $O_2^+-O_2$ , *J. Chem. Phys.* 46 (1967) 997–1005. doi:10.1063/1.1840838.
- [218] F.B. Alarcón, B.E. Fuentes, H. Martínez, F.B. Yousif, Single electron capture measurements in collisions of  $K^+$  on  $N_2$ , *Nucl. Instruments Methods Phys. Res. Sect. B Beam Interact. with Mater. Atoms.* 332 (2014) 317–320. doi:10.1016/j.nimb.2014.02.086.
- [219] W.J. Lichtenberg, K. Bethge, H. Schmidt-Böcking, Electron-loss cross-sections for negative ions at high energies, *J. Phys. B Atom. Molec. Phys.* 13 (1980) 343–357.
- [220] J.S. Risley, R. Geballe, Absolute  $H^-$  detachment cross-sections, *Phys. Rev. A.* 9 (1974) 2485. doi:10.1103/PhysRevA.9.2485.
- [221] J.B. Hasted, D. Phil, The Detachment of Electrons from Negative Ions, *Proc. R. Soc. A Math. Phys. Eng. Sci.* 222 (1954) 74–83. doi:10.1098/rspa.1954.0053.
- [222] J.B.H. Stedeford, J.B. Hasted, Further Investigations of Charge Exchange and Electron Detachment. I. Ion Energies 3 to 40 keV. II. Ion Energies 100 to 4000 eV, *Proc. R. Soc. A Math. Phys. Eng. Sci.* 227 (1955) 466–486. doi:10.1098/rspa.1955.0024.
- [223] A.E. Roche, C.C. Goodyear, Electron detachment from negative oxygen ions at beam energies in the range 3 to 100 eV, *J. Phys. B At. Mol. Phys.* 2 (1969) 191–200. doi:10.1088/0022-3700/2/2/307.
- [224] H.S.W. Massey, Negative ions, in: David R. Bates, B. Bederson (Eds.), *Adv. At. Mol. Phys.*, ACADEMIC PRESS, INC., 1979: pp. 1–36.
- [225] H.S.W. Massey, Collisions between atoms and molecules at ordinary temperatures, *Reports Prog. Phys.* 12 (1949) 248–269. doi:10.1088/0034-4885/12/1/311.
- [226] K. Takahashi, T. Hasegawa, Y. Sakai, Doubly excited states of molecular nitrogen by scattered electron-ion coincidence measurements, *Eur. Phys. J. D.* 71 (2017) 1–5. doi:10.1140/epjd/e2017-70465-7.
- [227] P. Erman, A. Karawajczyk, U. Köble, E. Rachlew, K.Y. Franzén, L. Veseth, Ultrashort-lived non-rydberg doubly excited resonances observed in molecular photoionization, *Phys. Rev. Lett.* 76 (1996) 4136–4139. doi:10.1103/PhysRevLett.76.4136.
- [228] K. Codling, Structure in the Photo-Ionization Continuum of  $N_2$  near 500 Å, *Astrophys. J.* 143 (1966) 552. doi:10.1086/148533.
- [229] M. Ukai, K. Kameta, N. Kouchi, Y. Hatano, K. Tanaka, Neutral decay of double-holed doubly excited resonances of  $N_2$ , *Phys. Rev. A.* 46 (1992) 7019–7022. doi:10.1103/PhysRevA.46.7019.
- [230] F. Cacace, G. de Petris, F. Pepi, A. Troiani, Direct Experimental Evidence for the  $H_2O+O_2^-$  Charge Transfer Complex: Crucial Support to Atmospheric Photonucleation Theory, *Angew. Chem. Int. Ed.* 39 (2000) 367–369. doi:10.1021/jp0006330.
- [231] N.B. Ram, V.S. Prabhudesai, E. Krishnakumar, Resonances in dissociative electron attachment to water, *J. Phys. B At. Mol. Opt. Phys.* 42 (2009). doi:10.1088/0953-4075/42/22/225203.

- [232] M.C. Fuss, L. Ellis-Gibbins, D.B. Jones, M.J. Brunger, F. Blanco, a. Muñoz, P. Limão-Vieira, G. García, The role of pyrimidine and water as underlying molecular constituents for describing radiation damage in living tissue: A comparative study, *J. Appl. Phys.* 117 (2015) 214701. doi:10.1063/1.4921810.
- [233] Y. Itikawa, N. Mason, Cross-sections for electron collisions with water molecules, *J. Phys. Chem. Ref. Data.* 34 (2005) 1–22. doi:10.1063/1.1799251.
- [234] W. Tattersall, L. Chiari, J.R. Machacek, E. Anderson, R.D. White, M.J. Brunger, S.J. Buckman, G. García, F. Blanco, J.P. Sullivan, Positron interactions with water-total elastic, total inelastic, and elastic differential cross-section measurements, *J. Chem. Phys.* 140 (2015). doi:10.1063/1.4862685.
- [235] F. Gobet, S. Eden, B. Coupier, J. Tabet, B. Farizon, M. Farizon, M.J. Gaillard, S. Ouaskit, M. Carré, T.D. Märk, Electron-loss and target ionization cross-sections for water vapor by 20-150 keV neutral atomic hydrogen impact, *Chem. Phys. Lett.* 421 (2006) 68–71. doi:10.1016/j.cplett.2006.01.016.
- [236] C. Szmytkowski, S. Stefanowska, N. Tańska, B. Żywicka, E. Ptasińska-Denga, P. Możejko, Cross-sections for electron collision with pyridine [C<sub>5</sub>H<sub>5</sub>N] molecule, *Mol. Phys.* 8976 (2018) 1–9. doi:10.1080/00268976.2018.1517908.
- [237] D.W. Hopper, K.M.K. Kutterer, A.L. Crombie, J.J. Clemens, Six-membered ring systems: pyridine and benzo derivatives, Elsevier Ltd, 2009. doi:10.1016/S0959-6380(09)70016-9.
- [238] M. Ryszka, E. Alizadeh, Z. Li, S. Ptasińska, Low-energy electron-induced dissociation in gas-phase nicotine, pyridine, and methyl-pyrrolidine, *J. Chem. Phys.* 147 (2017). doi:10.1063/1.4994679.
- [239] J. Wan, M. Hada, M. Ehara, H. Nakatsuji, Electronic excitation and ionization spectra of azabenzene: Pyridine revisited by the symmetry-adapted cluster configuration interaction method, *J. Chem. Phys.* 114 (2001) 5117. doi:10.1063/1.1351880.
- [240] U.S. Department of Commerce Washington DC, NIST Standard Reference Database No. 101, edited by R. D. Johnson III, 2018. (n.d.). <http://cccbdb.nist.gov/>.
- [241] D. Mathur, J.B. Hasted, Temporary negative-ion states in pyridine and diazine molecules, *Chem. Phys.* 16 (1976) 347–352. doi:10.1016/0301-0104(76)87030-9.
- [242] A.I. Lozano, J. Jiménez, F. Blanco, G. García, Total electron scattering cross-section from pyridine molecules in the energy range 1–200 eV, *Phys. Rev. A.* 98 (2018) 012709. doi:10.1103/PhysRevA.98.012709.
- [243] A. Traoré Dubuis, F. Costa, F.F. da Silva, P. Limão-Vieira, J.C. Oller, F. Blanco, G. García, Total electron scattering cross-section from pyridine molecules in the energy range 10–1000 eV, *Chem. Phys. Lett.* 699 (2018) 182–187. doi:10.1016/j.cplett.2018.03.065.
- [244] A. Sieradzka, F. Blanco, M.C. Fuss, Z. Maśń, J.D. Gorfinkiel, G. García, Electron scattering from pyridine, *J. Phys. Chem. A.* 118 (2014) 6657–6663. doi:10.1021/jp503665a.
- [245] A.S. Barbosa, D.F. Pastega, M.H.F. Bettega, Shape resonances in the elastic scattering of slow electrons by pyridine, *Phys. Rev. A - At. Mol. Opt. Phys.* 88 (2013) 1–6.

- doi:10.1103/PhysRevA.88.022705.
- [246] C.Q. Jiao, C.A. DeJoseph, R. Lee, A. Garscadden, Kinetics of electron impact ionization and ion-molecule reactions of pyridine, *Int. J. Mass Spectrom.* 257 (2006) 34–40. doi:10.1016/j.ijms.2006.06.007.
- [247] J.N. Bull, J.W.L. Lee, C. Vallance, Absolute electron total ionization cross-sections: Molecular analogues of DNA and RNA nucleobase and sugar constituents, *Phys. Chem. Chem. Phys.* 16 (2014) 10743–10752. doi:10.1039/c4cp00490f.
- [248] M.A. Śmiałek, M.A. MacDonald, S. Ptasńska, L. Zuin, N.J. Mason, Photoelectron and threshold photoelectron valence spectra of pyridine, *Eur. Phys. J. D.* 70 (2016). doi:10.1140/epjd/e2016-60673-0.
- [249] G. Vall-Ilosera, M. Coreno, P. Erman, M.A. Huels, K. Jakubowska, A. Kivimäki, E. Rachlew, M. Stankiewicz, VUV photoionisation of free azabenzene: Pyridine, pyrazine, pyrimidine, pyridazine and s-triazine, *Int. J. Mass Spectrom.* 275 (2008) 55–63. doi:10.1016/j.ijms.2008.05.019.
- [250] R. Cabrera-Trujillo, E. Deumens, Y. Öhrn, O. Quinet, J.R. Sabin, N. Stolterfoht, Water-molecule fragmentation induced by charge exchange in slow collisions with He<sup>+</sup> and He<sup>2+</sup> ions in the keV-energy region, *Phys. Rev. A - At. Mol. Opt. Phys.* 75 (2007) 1–13. doi:10.1103/PhysRevA.75.052702.
- [251] F. Alvarado, R. Hoekstra, T. Schlathölder, Dissociation of water molecules upon keV H<sup>+</sup> and He<sup>q+</sup>-induced ionization, *J. Phys. B At. Mol. Opt. Phys.* 38 (2005) 4085–4094. doi:10.1088/0953-4075/38/22/012.
- [252] D. Oubaziz, R. Boulifa, Z. Aitelhadjali, C. Champion, Double ionization of water molecules by proton impact: the role of the direct ionization mechanism, *Eur. Phys. J. D.* 72 (2018). doi:10.1140/epjd/e2018-80307-9.
- [253] C. Illescas, L.F. Errea, L. Méndez, B. Pons, I. Rabadán, A. Riera, Classical treatment of ion-H<sub>2</sub>O collisions with a three-center model potential, *Phys. Rev. A - At. Mol. Opt. Phys.* 83 (2011) 1–12. doi:10.1103/PhysRevA.83.052704.
- [254] R.W. Fessenden, P. Neta, ESR Spectra of radicals produced by reduction of pyridine and pyrazine, *Chem. Phys. Lett.* 18 (1973) 14–17. doi:10.1016/0009-2614(73)80327-6.
- [255] J.P. Doering, J.H. Moore, Observation of a singlet-triplet transition in gas phase pyridine by ion and electron impact, *J. Chem. Phys.* 56 (1972) 2176–2178. doi:10.1063/1.1677515.

